Université de Toulouse

THESE

En vue de l'obtention du

DOCTORAT DE L'UNIVERSITÉ DE TOULOUSE

Délivré par :
Institut National Polytechnique de Toulouse (INP Toulouse)

Discipline ou spécialité :
Dynamique des fluides

Présentée et soutenue par :
Ignacio DURAN GARCIA-RAMA
Le 25/11/2013

Titre :
Prediction of combustion noise in modern aero engines combining large eddy simulations and analytical methods.

Ecole doctorale :
Mécanique, Energétique, Génie civil et Procédés (MEGeP)

Unité de recherche :
CERFACS

Directeur(s) de Thèse :
Thierry POINSOT (Directeur de Recherche à l'IMF de Toulouse, France)
Co-directeur : Stéphane MOREAU (Professeur à l'Université de Sherbrooke, Canada)

Rapporteurs :
Christopher TAM (Professor, Florida State University, USA)
Christophe BAILLY (Professor, Ecole Centrale de Lyon, France)

Autre(s) membre(s) du jury :
Friedrich BAKE (DLR, Berlin, Germany)
Alexis GIAUQUE (Ecole Centrale de Lyon, France)
Claude SENSIAU (SNECMA, France)

Prediction of combustion noise in modern aero-engines combining Large Eddy Simulations and analytical methods

A dissertation submitted in partial fulfillment of the requirements for the degree

Doctor of Philosophy

by

Ignacio Durán García-Rama

Institut National Polytechnique
Toulouse

Advisor :	Thierry Poinsot	-	CNRS / IMFT
Co-advisor :	Stéphane Moreau	-	Université de Sherbrooke
Reviewers :	Christopher Tam	-	Florida State University
	Christophe Bailly	-	Ecole Centrale de Lyon
Examiners :	Friedrich Bake	-	DLR
	Alexis Giauque	-	Ecole Centrale de Lyon
Guest :	Claude Sensiau	-	Snecma

November 2013

Abstract

Combustion noise is increasing its relative contribution to aircraft noise, while other sources are being reduced and new low-NOx emission combustion chambers being built. Two mechanisms are responsible for this noise source: direct noise in which acoustic waves are generated by the flame and propagate to the outlet of the aero-engine, and indirect noise, where entropy waves generate noise as they are accelerated and decelerated in the turbine stages. In this work the analytical models used for the propagation of waves through non-homogeneous flows, including the generation of indirect noise, are revised and extended. In the first part, the quasi-1D case is studied, extending the analytical method to non-zero frequencies and validating the results with numerical methods and experimental data. In the second part, the 2D method for the case of compact turbine blades is studied and validated using numerical simulations of a rotating blade and of a complete turbine stage. Finally, in the third part of this thesis, these models are combined with reactive and compressible Large Eddy Simulations (LES) of combustion chambers to build a hybrid approach, named CHORUS, able to predict combustion noise.

Keywords: Combustion noise, indirect noise, aeroacoustics, analytical methods.

Résumé

La contribution relative du bruit de combustion au bruit global des moteurs aéronautiques augmente progressivement dû d'un coté à la réduction des autres sources et d'un autre à l'implémentation des nouvelles technologies de chambre de combustion pour la réduction des émissions de NOx. Deux mécanismes sont responsables de cette source de bruit : d'abord le bruit direct, dû aux ondes acoustiques générées par la flamme qui se propagent à la sortie du moteur d'avion, et ensuite le bruit indirect, généré par les ondes d'entropie quand elles sont accélérées et ralenties dans les étages de turbine. Dans ce travail, les modèles analytiques utilisés pour la propagation des ondes à travers les flux non-homogènes, y compris la génération de bruit indirect, sont révisés et étendus. Tout d'abord, le cas quasi-1D est étudié: la méthode analytique est étendue pour les fréquences non nulles et validée avec des méthodes numériques et des données expérimentales. Dans la seconde partie, la méthode analytique 2D dans le cas d'aubes de turbines compactes est étudiée et validée à l'aide de simulations numériques d'un rotor et d'un étage de turbine complète. Enfin, ces modèles sont combinés avec des simulations aux grandes échelles réactives et compressibles de chambres de combustion pour construire une approche hybride appelée CHORUS capable de prédire le bruit de combustion.

Mots clés: Bruit de combustion, bruit indirect, aéroacoustique, méthodes analytiques.

Contents

List of figures iv

Acknowledgements xiii

1 General introduction 1

1.1 International regulations 2

1.2 Noise sources in modern aero-engines 4

1.3 Combustion noise 5

1.3.1 Indirect combustion noise 5

1.3.2 Direct combustion noise 7

1.4 Propagation of waves 8

1.5 Objectives and organisation of this thesis 11

I Propagation of waves through non-uniform quasi-1D flows 13

Introduction 17

2 State of the art 21

2.1 The flow through a quasi-1D nozzle 21

2.1.1 Steady flow 23

2.1.2 Linearised Euler equations 25

2.2 The compact nozzle method 27

2.3 Linear mean velocity profile nozzle method 30

2.4 Asymptotic expansion of the linearised Euler equations 34

3 The invariant method 37

3.1 The invariant equation 38

3.2 The Magnus expansion 40

3.2.1 Solution for larger frequencies 43

3.3 Boundary conditions 44

3.3.1 Subsonic flow 45

3.3.2 Choked flow 47

3.3.3 Supersonic flow with a shock wave 49

4 Nozzle transfer functions at non-compact frequencies 55

4.1 Comparison with a linear steady velocity choked nozzle 56

4.2 Comparison with the 'equivalent nozzle length' method for choked nozzles 63

4.3 Comparison with experimental measurements 69

4.4 Study of subsonic nozzles 71

4.5 Parametric study on direct and indirect combustion noise . . 76

Conclusions 81

II Propagation of waves through turbine stages 85

Introduction 89

5 Two-dimensional analytical method 93

5.1 Introduction and assumptions 93

5.2 Wave decomposition 95

5.2.1 Entropy wave 96

5.2.2 Vorticity wave 97

5.2.3 Acoustic waves 98

5.3 Jump conditions through the blade row 100

5.3.1 Stator vane 101

5.3.2 Rotor blade . . . 103
5.4 Solution of the equations and boundary conditions . . . 105

6 Numerical simulations 109
6.1 Numerical methods . . . 110
6.1.1 Numerical methods for rotation . . . 111
Method A: ALE method . . . 111
Method B: MISCOG method . . . 113
Method C: No-deformation method . . . 113
6.1.2 Boundary conditions and forcing term . . . 114
6.1.3 Post-processing of the waves . . . 118
6.2 Rotor case study . . . 120
Acoustic wave . . . 122
Entropy wave . . . 123
6.3 Stator-Rotor case study . . . 128
Acoustic wave . . . 128
Entropy wave . . . 130

Conclusions 139

III Predicting combustion noise combining LES and analytical tools for the propagation of waves 141

Introduction 145

7 Description of the methodology 147
7.1 Compressible reactive LES of the combustion chamber . . . 147
7.2 The CHORUS post-processing . . . 150
7.2.1 Primitive variables . . . 151
7.2.2 Waves at the outlet of the combustion chamber . . . 153
7.2.3 Transmission through the turbine stages . . . 155
7.2.4 Acoustic power computation . . . 157

8 Application to an aero-engine **159**

8.1 LES of the combustion chamber 159

8.1.1 Flow description 162

8.2 Waves in the combustion chamber 164

8.3 Direct and indirect combustion noise 165

Conclusions **171**

General conclusions and perspectives **173**

Bibliography **186**

Articles **187**

List of Figures

1.1 Primary energy use in the US (2011). Source: EIA (2013). . . 2

1.2 Global CO_2 emissions by sector. 3

1.3 Historical data obtained from ICAO (2013) website. 3

1.4 The two mechanisms of combustion noise. 6

1.5 Methodology to predict combustion noise combining Large Eddy Simulations (LES) and analytical methods. 10

1.6 Developments made in this PhD. 10

2.1 A quasi-1D nozzle. 23

2.2 Mach number as a function of the cross-section ratio. 25

2.3 Sketch of the acoustic and entropy waves in a subsonic converging-diverging nozzle. 28

2.4 Sketch of a linear mean velocity profile nozzle. 31

3.1 Sketch of the acoustic and entropy waves in a converging-diverging choked nozzle. 48

3.2 Sketch of a shock wave in a diverging section. u'_s is the movement of the shock wave due to the incoming perturbations. . 50

4.1 Section and Mach number of two linear steady velocity profile nozzles with inlet Mach number of $M_0 = 0.29$ and two different outlet Mach numbers. 56

4.2 Amplitude and phase of the downstream-facing acoustic wave at the outlet, w_1^+, generated by an incoming entropy wave, $w_0^s = 1$, with $M_0 = 0.29$. ant method (——); hypergeometric equation (•) and compact solution (– · – · –). 57

4.3 Amplitude and phase of the upstream-facing acoustic wave at the outlet, w_1^-, generated by an incoming entropy wave, w_0^s = 1, with M_0 = 0.29. Invariant method (——); hypergeometric equation (•) and compact solution (– · – · –). 58

4.4 Amplitude and phase of the reflection coefficient (w_0^- due to w_0^+) for a linear steady velocity choked nozzle with M_0 = 0.29 and M_1 = 1.5. Invariant method (——); hypergeometric equation (•) and compact solution (– · – · –). 58

4.5 Amplitude and phase of the acoustic wave, w_0^-, generated by an incoming entropy wave, w_0^s = 1, with M_0 = 0.29 and M_1 = 1.5. Invariant method (——); hypergeometric equation (•). 59

4.6 Section and Mach number of a converging-diverging nozzle. Geometry obtained with (4.2) (——) and with the linear steady velocity profile (– – –), with inlet and outlet Mach numbers M_0 = 0.29 and M_1 = 1.5 for both nozzles. (•) represents the nozzle subdivisions for the invariant method for calculation up to Ω = 5. 60

4.7 Amplitude and phase of the acoustic wave at the outlet, w_1^+, generated by an incoming acoustic wave at the inlet, w_0^+. Geometry obtained with (4.2) and solved using the invariant method (——) and numerically (∘); linear steady velocity profile (– – –). 61

4.8 Amplitude and phase of the reflected acoustic wave at the inlet, w_0^-, generated by an incoming acoustic wave at the inlet, w_0^+. Geometry obtained with (4.2) and solved using the invariant method (——) and numerically (∘); linear steady velocity profile (– – –). 61

4.9 Amplitude and phase of the acoustic wave at the outlet, w_1^+, generated by an incoming entropy wave at the inlet, w_0^s. Geometry obtained with (4.2) and solved using the invariant method (——) and numerically (∘); linear steady velocity profile (– – –). 62

4.10 Plot of $A(\xi)$ of the nozzle of Stow et al. (2002). 63

4.11 Amplitude and phase of the reflected acoustic wave at the inlet of the nozzle (w_0^- due to w_0^+). Stow's equivalent length method, (+), Stow's numerical results (∘), and invariant method (——). 64

4.12 Plot of $M(\xi)$ for the nozzle used in Goh and Morgans (2011a) for three flow configurations: choked isentropic (thick line), choked with a shock wave at the nozzle outlet (thin line) and choked with a shock wave in the divergent (dashed line). . . . 65

4.13 Amplitude and phase of the transmitted acoustic wave generated by an acoustic perturbation at the inlet for a choked nozzle. Equivalent nozzle length method (∘), Marble and Candel method (×) and invariant method (——). 65

4.14 Amplitude and phase of the transmitted acoustic wave generated by an entropy perturbation at the inlet for a choked nozzle. Equivalent nozzle length method (∘), Marble and Candel method (×) and invariant method (——). 66

4.15 Amplitude and phase of the transmitted acoustic wave generated by an acoustic perturbation at the inlet for the choked case with a shock wave at the end of the nozzle. Equivalent nozzle length method (∘), Marble and Candel method (×) and invariant method (——). 66

4.16 Amplitude and phase of the transmitted acoustic wave generated by an entropy perturbation at the inlet for the choked case with a shock wave at the end of the nozzle. Equivalent nozzle length method (∘), Marble and Candel method (×) and invariant method (——). 67

4.17 Amplitude and phase of the transmitted acoustic wave generated by an acoustic perturbation at the inlet for the choked case with a shock wave. Equivalent nozzle length method (∘), Marble and Candel method (×) and invariant method (——). 68

4.18 Amplitude and phase of the transmitted acoustic wave generated by an entropy perturbation at the inlet for the choked case with a shock wave. Equivalent nozzle length method (∘), Marble and Candel method (×) and invariant method (——). 68

4.19 Axisymmetric nozzle geometry of Bell et al. (1973). 70

4.20 Real and imaginary parts of the acoustic admittance Y of three different choked nozzles; $M_0 = 0.08$, $r_{cc}/r_c = 0.44$. For $\theta_1 = 15$: analytical (——), experiments (∘). For $\theta_1 = 30$: analytical (– – –), experiments (△). For $\theta_1 = 45$: analytical ($\cdots$), experiments (▪). 71

4.21 Section of the EWG nozzle, and three Mach number profiles, corresponding to three different throat Mach numbers. 73

4.22 Amplitude of the transmitted and reflected acoustic waves generated by an entropy wave in the EWG nozzle, for different throat Mach numbers calculated using the invariant method. 73

4.23 Amplitude of the transmitted and reflected acoustic waves generated by an entropy wave in the EWG nozzle, for M_T = 0.7 calculated using the invariant method at different orders of the Magnus expansion. 74

4.24 Amplitude of the acoustic transmission and reflection coefficients of the EWG nozzle calculated using the invariant method. 75

4.25 Simplified model of a combustor used by Leyko et al. (2009). 75

4.26 Indirect to direct noise ratio, η, calculated using the invariant method as a function of the inlet and the outlet Mach numbers of the nozzle, M_0 and M_1, for different frequencies. 79

5.0 Acoustic response of a stator blade at the outlet (2) to a perturbation at the inlet (1) for different flow orientations θ (in degree). Computed using the 2D compact model of Cumpsty and Marble (——); 1D compact model Marble and Candel with Mach number based on the overall velocity magnitude ($- \cdot -$), or on the axial velocity component ($- - -$). Figure reproduced from Leyko (2010). 90

5.1 Sketch of the studied configuration. 94

5.2 Sketch of the jump conditions using the compact blade assumption. 101

5.3 Sketch of the flow through a rotor blade. Superscript $(\,)^r$ represents the variables in the rotor reference frame. 104

6.1 Sketch of the computational domain of the stator-rotor configuration. L_y = 50 mm, L_x^{in} = 150 mm and L_x^{out} = 450 mm. . . 111

6.2 Sketch of the stator-rotor showing the moving region and the deformed mesh for the ALE method. 112

6.3 Analysis of the mesh deformation for the ALE method. 112

6.4 Detail of the mesh deformation of figure 6.2 for the region between the stator and the rotor blades. Two vertical lines delimit the deformed region. 113

6.5 Sketch of the interface between the two simulations: CFD1 and CFD2 for the MISCOG method. 114

6.6 Reflection coefficient of the outlet boundary condition. 115

6.7 Function $f(t)$ used to pulse the boundary conditions plotted with $N = 50$. 116

6.8 Function $f_r(t)$ used to pulse the boundary conditions plotted with $N = 50$. 117

6.9 Vorticity field of the flow for the stator-rotor case. 119

6.10 Sketch of the computational domain of the rotor configuration. 120

6.11 Acoustic transfer functions. (——): Analytical theory; (x): No-deformation method; ($\bullet$): ALE method; ($+$): MISCOG method. 123

6.12 Entropy transfer functions. (——): Analytical theory; (x): No-deformation method; ($\bullet$): ALE method; ($+$): MISCOG method. 124

6.13 Entropy transmission through the rotor blade. (——): Analytical method; ($\bullet$): Numerical simulations at different x locations, increasing from the trailing edge to a one-chord distance downstream. 124

6.14 Instantaneous fields of the entropy wave propagating through the rotor blade, calculated using the MISCOG method. Note that the forcing function $f(t)$ from figure 6.7 is used here for a better visualisation of the flow. 125

6.15 Streamlines through the rotor blade in the rotating reference frame (a) and the time-delay function, $t_d(y)$, calculated using the mean flow the rotor. 126

6.16 Attenuation of the entropy wave due to the deformation of the plane mode by the mean flow through the rotor, $D_0(f)$, calculated using $t_d(y)$ of figure 6.15(b) (——), and obtained numerically at the outlet of the rotor blade ($\bullet$). 127

6.17 Entropy transfer functions for the rotor blade with the attenuation function model, $D_0(f)$. (——): Analytical method; (x): No-deformation method; ($\bullet$): ALE method; ($+$): MISCOG method. 128

6.18 Acoustic transfer functions. (——): Analytical method; ($\bullet$): ALE method; ($+$): MISCOG method. 130

6.19 Entropy transfer functions. (——): Analytical theory; ($\bullet$): ALE method; ($+$): MISCOG method. 131

6.20 Instantaneous fields of the entropy wave propagating through the stator-rotor configuration, calculated using the MISCOG method. Note that the forcing function $f(t)$ from figure 6.7 is used here for a better visualisation of the flow. 132

6.21 Entropy transmission throughout the stator-rotor. (——): Analytical model; (•): ALE method; (+): MISCOG method. 133

6.22 Streamlines through the turbine blades obtained using the mean flow of the MISCOG simulation. 133

6.23 Value of $t_d(y)$ obtained using the mean flow of the MISCOG simulation. 134

6.24 Attenuation of the entropy wave due to the mean flow, $D_0^s(f)$ and $D_0^r(f)$ calculated using $t_d(y)$ of figure 6.23. 134

6.25 Entropy transmission through the stator-rotor. (——): Model for the entropy attenuation; (•): ALE method; (+): MISCOG method. 135

6.26 Entropy transfer functions. (——): Analytical method with correction on the entropy wave; (•): ALE method; (+): MISCOG method. 136

6.27 Acoustic waves at the inlet (a) and at the outlet (b). (▲): Reference simulation with no forcing; (•): forcing the entropy wave at the inlet using $f(t)$ from figure 6.7; (+): forcing the entropy wave at the inlet using $f_r(t)$ from figure 6.8. 136

6.28 Entropy waves forced the inlet. (▲): Reference simulation with no forcing; (•): forcing the entropy wave at the inlet using $f(t)$ from figure 6.7; (+): forcing the entropy wave at the inlet using $f_r(t)$ from figure 6.8. 137

7.1 Sketck of CHORUS methodology for computing combustion noise. 150

7.2 Interpolation of LES results at several outlet planes of the engine. 151

7.3 CHORUS procedure for computing the waves at the outlet of the combustion chamber and the noise generated at the outlet of the aero-engine (adapted from Leyko 2010). 152

8.1 Combustion chamber studied. 160

8.2 Mesh used for the LES of the combustion chamber. 161

8.3 Mean velocity $[m/s]$ of a cross-section of the combustion chamber. 162

8.4 Temperature fields of a cross-section of the combustion chamber $[K]$. A solid black line on (a) shows the central recirculation zone. 163

8.5 Instantaneous field of heat release. 163

8.6 Instantaneous field of the temperature fluctuation $[K]$. 164

8.7 Spectra of the waves at the outlet of the combustion chamber for the plane mode (■) and for the first circumferential mode of the sector, $m = 18$ (▲). 166

8.8 Combustion noise at the outlet of the turbine stages. Indirect noise (▲), direct noise (■) and vorticity noise (●). No attenuation considered. 167

8.9 Transfer function of the complete turbine considered for the plane mode. 167

8.10 Combustion noise at the outlet of the turbine stages. Indirect noise (▲), direct noise (■) and vorticity noise (●) considering the attenuation functions for the entropy wave. 168

8.11 Noise integrated over all frequencies at each turbine stage. Indirect noise (▲), direct noise (■) and vorticity noise (●). . . 169

Acknowledgements

I would like to thank first the jury for reading my manuscript and for the interesting questions and discussion during my PhD defense.

Je voudrais remercier particulièrement mes encadrants, Thierry et Stéphane, qui ont su m'encadrer en me laissant libre au même temps pour pouvoir développer mes propres idées.

Merci à l'équipe Snecma qui m'a encadré. Un grand merci pour Alexandre Vuillemin, qui m'a encadré depuis Snecma pendant la première année. Je me souviens toujours le jour de l'entretien a Snecma, ou je n'arrivais pas a trouver un taxi et je t'avais appelé pour que tu viennes me chercher en voiture à la gare de Lieussaint! Merci aussi pour tes remarques toujours constructives sur le déroulement de ma these! Et pour les soirées post-conference à Portland! Merci a Claude, qui a pris la suite d'Alex. C'était un plaisir de travailler avec toi pendant ces semaines que j'ai passé à Snecma! J'ai bien aimé nos sorties au Phantom Canyon, devant l'hôtel à Colorado Springs, pour nous détendre après l'AIAA. Gracias también a Guillém, por todo el apoyo que me has dado desde Snecma. Merci aussi a Jacky, Guillaume, Jean-Michel, Cyprien, Rasika, Maxime, Norman, et tout le groupe d'acousticiens a Snecma! C'était un plaisir de travailler avec vous!

Merci aussi à tous les seniors du CERFACS: Laurent, Florent, Franck, Gab, Olivier, Eleonore (pour les bonjours du matin!), Benedicte... je vous ai tous embêté avec mes questions! Merci aussi aux gens d'aéro, que j'ai aussi embêté: Nico, Guillaume, Hugues, etc. Je voudrais remercier aussi tout l'équipe CSG. Fabrice, Gérard, Patrick et Isabelle, toujours très réactifs! Merci aussi à Marie, Nicole, Séverine et Lydia. Un merci spéciale à Chantal et Michèle, pour être toujours si souriantes!

Pendant ces trois années j'ai croisé pas mal des gens, au cerfacs et ailleurs. Merci d'abord aux thésards du cerfacs que j'ai rencontré: D'abord Matthieu Leyko, qui m'a appris tellement des choses pendant mon début! Merci aussi a Camilo, j'espère te croiser un jour dans une autre conference! Merci a Elsa, Jorge, Mario, Ignacio H., Ali, Thomas Pedot, Anthony Ruiz, Patricia, Victor! Tout l'équipe de foot! Et merci Guillaume, mon collègue d'aviron!

Merci a Corentin et Thomas, qui continuent a travailler sur le bruit de combustion, et a Cesar et Melissa, qui vont faire la suite! Merci a Dimitri pour tout l'aide sur l'utilisation de TurboAVBP (ou MISCOG... je sais plus!). Merci Geoffroy pour le panier de légumes... et pour tout en générale! C'est toi le prochain! Merci à Jean-Phi, Greg, Rémy, Raph, Dorian, Mika, Antony, Damien, Sandrine, Lucas, David, Pierre, Pablo, mon co-bureau Basti, Jérôme (cuando quieras nos vemos por Madrid y nos tomamos unas birras y unas tapas!), Abdulla (merci pour tous les discussions qu'on a eu!) et Luis le stagiaire en bruit de combustion! Aïssa, Franchine, Laura... Merci aussi à Daniel et les gens de l'IMFT! Merci à Laurent Selle, pour tes conseils et les discussions, scientifiques ou pas! Merci aux gens de l'équipe aéro, François, Adrien, Yannis, Sophie, Thomas Leonard, Seb, Flore... Et aussi a JC! J'ai bien aimé nos voyages en Italie, USA... on a bien profité de la thèse! Et on a fait pas mal de rencontres... un mot spéciale pour notre cher Chief Tsosie (plus connu comme Chief PD!). Souviens-toi de moi quand tu trouves un poste chez airbus JC!

Merci aux gens de l'EC2M que j'ai rencontré pas mal de fois: Sébastien Ducruix et Thierry Schuller, à ceux de l'ONERA, Alexis et Maxime, j'ai bien apprécié les discussions qu'on a eu! Merci aux gens d'airbus, Yann en particulier. J'ai passé des très bon moments avec vous!

Un merci especial al grupo de comida en español de MeteoFrance: Carole, Marie, Florent, Emilia, Julia y Laura. Y por supuesto Gus, que nos abandono para trabajar para la competencia (el ONERA) y ahora se arrepiente y quiere volver ;). Y sin olvidar a Xavi y a Silvia! Gracias por todos los consejos, todas las soirées, las catas de vinos variados (monolithiques, avec une arome a Printemps...) y por supuesto la paella! Que rica que estaba! Bueno, espero que vengáis a vernos a Londres muy a menudo! Thanks to the group of english-speaking people of MeteoFrance... most of you being those mentioned above for the 'spanish-speaking people', but also including Paul, Siliang and Dominique.

Gracias a Elena! He pasado un ultimo año difícil sin nuestras pausas café para desquitarnos! Gracias también a Ronan! Te veo pronto en la entrega de medallas Fields! A ver si venís a Londres a visitarnos! Merci aussi à Elodie et à Joris! Gracias a Roberto, por las charlas en castellano (para que no se me olvide!), y los consejos que me has dado este tiempo! Y gracias también a Javi, con quien recorrí el cañón del Paria y Hells Canyon, aun a riesgo de ser comidos por una serpiente o un oso (o los dos!). Un recuerdo especial a los ITP guys... espero veros pronto en alguna conferencia AIAA!

Merci à tous les amis que j'ai rencontré à Toulouse pendant ces années: Helen, Suse et Viktoria! Merci pour vos cours d'allemand! Merci a Matthias Pointner et François Deudon! Conrado, my trip-mate! I've visited half

of europe with you, and soon Australia! Et bien sur, Francesco Stella, Audrey, Francesco Fiore, Domenico, Pablo, Victor et Solène, Fran y Anabel, Severine, Raul, Tina, Nico et Agnese, Txemus, Laura y Nico, la super-coloc: Pancho, Camille y Anna! J'ai passé des années incroyables avec vous! Des voyages ensemble (Galicia!), des randos dans les Pyrénées, ou on nage dans dans des lacs et rivières presque congelés, des soirées tranquilles, pas tranquilles, des BBQ... tellement des choses qu'on a fait tous ensemble! Et sans oublier mes voisins: Julien et Muriel, qui font des aperos, fondues, tapas et tout ce qu'ils veulent! Y de nuevo a Xavi y Silvia, que repito, tenéis que venir a Londres!

Gracias a mis amigos de Madrid, Iris, Nuria, Carlos, Diego y Ana! Espero veros en Londres!

Gracias (de nuevo) a la super-coloc... los colocs originales (Pancho y yo), que fueron los primeros en aprender la danza de la coloc, a los que luego se sumaron Camille y Anna, que pronto aprendieron a bailar también! Y por supuesto, esta tesis esta dedicado al inventor del jamón, el invento mas importante del mundo! :)

Muchas gracias a mi hermanita Laura, que es la que mas veces ha venido a verme a Toulouse en estos años... hasta el punto de conocer a Nico y quedarse a vivir aquí! Gracias por ser siempre tan simpática y una hermana tan perfecta!

Y para terminar, gracias sobre todo a mis padres, que han hecho posible todo esto! Gracias por vuestro apoyo y paciencia! Porque habéis sabido ser los mejores padres que jamás podría haberme imaginado. Esta tesis no habría sido posible sin vosotros! Y por extensión a mi familia: tíos tías, abuela y primos por igual! Gracias a todos!

Gracias a Anna, que me ha apoyado tanto estos años. Gracias por estar a mi lado!

Thank you all!

Ignacio Durán García-Rama

Chapter 1

General introduction

Combustion of fossil fuels is nowadays the main mechanism for generating energy. In the US alone, combustion of coal, natural gas and petroleum represents about 80% of the total energy used (EIA, 2013), as shown in figure 1.1. This is even more significant for the transport sector where this ratio increases to 98%, and particularly for the aeronautical sector which is dominated by combustion-driven engines, and therefore powered mainly by burning petroleum products.

Combustion is an easy way of generating thermal energy, which can be easily and efficiently converted into mechanical and electrical energy. Fossil fuels have the advantage of having a large energy-release to mass ratio, which make them suitable for transport systems. Another advantage of combustion systems is its wide range of applications since burners can be either small for domestic applications or large for industrial power-plants. The major drawback of combustion, however, is the negative effects of pollutants generated by this activity on both health and environment. Alternatives to combustion systems, such as nuclear energy or renewables (solar, wind and hydroelectric power) find their application in large-scale electricity production, while for transport systems they are less suited due to the large weight of these systems. For this reason, it is expected that transport, and in particular aircraft, will still be powered by the combustion of fossil fuels (or alternatively biofuel or synthesised methane, obtained for example from renewable or nuclear energy using the Sabatier reaction). This is why the pollutants produced during combustion have to be reduced.

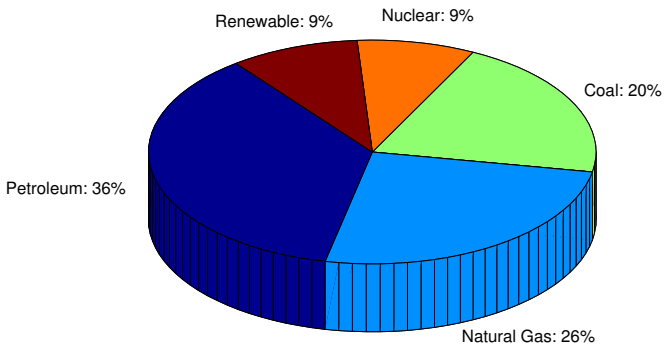

Figure 1.1 – *Primary energy use in the US (2011). Source: EIA (2013).*

There are three main pollutants generated by the aeronautical industry: CO_2, nitric oxides and noise emissions. The global aviation industry is responsible for 2% of all the human-induced CO_2 emissions, as seen in figure 1.2. It is also responsible for generating nitric oxides (NO_x), which strongly contribute to the degradation of air quality and produce acid rain, and noise emissions, which have an influence on health and quality of life in the vicinity of airports. All these pollutants must be reduced to meet the international regulations and restrictions on pollutant emissions.

1.1 International regulations

Since 1995 the world's air traffic has increased at an average annual growth rate of 5.0% (measured in RPK[1]), according to the International Civil Aviation Organisation (ICAO, 2013), as shown in figure 1.3. It is expected that this annual growth will continue at an average rate of around 4.5% in the next decades. This growth leads to a global increase of pollution and noise emissions generated by the aeronautical industry, which should be minimised.

With the objective of reducing all types of pollutant emissions, in 2001 the Advisory Council for Aeronautical Research in Europe (ACARE, 2013) established targets for new aircraft designs entering into service in 2020. These included a reduction of fuel consumption (and CO_2) emissions by

[1]RPK: Revenue Passenger-Kilometer is a measure of traffic calculated by multiplying the number of revenue-paying passengers by the distance travelled

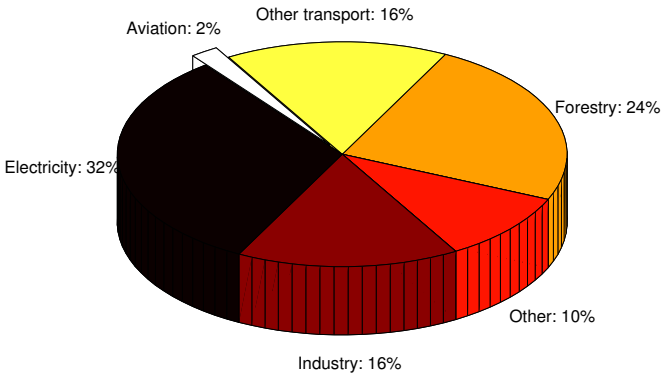

Figure 1.2 – *Global CO_2 emissions by sector.*

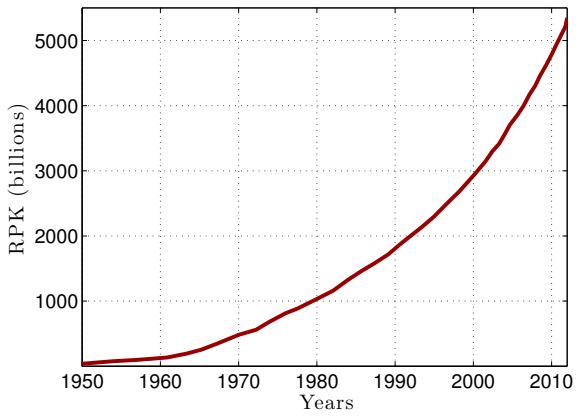

Figure 1.3 – *Historical data obtained from ICAO (2013) website.*

50%, the reduction of NO_x emissions by 80% and the reduction of perceived noise by 50% with respect to levels in 2001. Similarly, the ICAO (2013) defines maximum noise levels for certifying an aircraft, but some airports define even more restrictive levels due to the proximity of residential areas. Furthermore, aircraft operators are also concerned about passenger comfort and demand a quieter cabin. Noise emissions are therefore a major concern for both aircraft and engine manufacturers and must be viewed as another pollutant created by combustion.

For these reasons, the reduction of acoustic emissions has been a major field of research in both industry and research groups.

1.2 Noise sources in modern aero-engines

The first studies on the subject, carried out by Lighthill (1952), showed the great importance of jet noise on the overall noise emissions. This was done in the context of the recently adopted jet engine which was significantly louder than its helix-propelled predecessors. Lighthill showed that the jet-noise source scaled with the eighth power of the jet-exhaust speed, meaning that doubling the jet speed would lead to an increase of the acoustic intensity level by nearly 50dB. Jet speed reduction was at the time not only a noise concern but also a performance requirement as the propulsive efficiency increased significantly when the jet speed was reduced, increasing aircraft range and reducing costs. The turbofan engine used nowadays achieved these goals reducing jet speed and maintaining the total thrust by increasing the mass-flow using a secondary flow. The increase of the propulsive efficiency and the noise reduction were significant, but the increase of air traffic and the construction of airports near residential areas forced aircraft manufacturers to further decrease the global noise emissions. At the same time fuel costs and environmental concerns lead to further research on consumption reduction. The reduction of jet speed reached its maximum as a higher by-pass rate lead to heavier engines and therefore higher fuel consumption. Research on the reduction of jet noise continued in different directions, leading to solutions which were in many cases opposed to those reducing fuel consumption and where a compromise had to be found. Chevrons, for example, were adopted to enhance the jet mixing at the outlet of the nozzle to reduce jet noise, but this mechanism also had an impact on the propulsion, reducing the total thrust of the engine and therefore increasing fuel consumption.

Other noise sources started to increase their relative contribution as jet noise was significantly reduced. Firstly, the turbofan engine reduced jet noise but at the same time added a new and non-negligible contribution: fan noise. As jet noise was being reduced, research on fan and turbomachinery noise increased as there was still significant room for improvement. Airframe, landing gear, flap and slat noise were also considered. Combustion noise was initially addressed in the work of Strahle (1972), Chiu and Summerfield (1974), Hassan (1974), Marble and Candel (1977) and Cumpsty and Marble (1977), however, its relative contribution to global aircraft acoustic emissions was still low. It was not until the development of the new low NO_x-emission combustion chambers, such as lean premixed, rich-quench-lean or staged-

injection combustion chambers that noise emissions from the combustion chamber increased their relative contribution and started to be a major concern. These new combustion chamber concepts have been adopted to reduce NO_x emissions, but the design has two major issues. On the one hand, they can present combustion instabilities when the turbulent flame interacts with the acoustics of the chamber in a constructive way, increasing the acoustic energy which can lead to severe damage of the combustion system (Lieuwen and Yang, 2005; Poinsot and Veynante, 2011). On the other hand, and as the main subject of this thesis, the turbulent flame induces larger heat release fluctuations as the mixture is close to the lean extinction point. These heat release fluctuations generate two types of waves, acoustic and entropy, which are responsible for the two mechanisms of combustion noise generation as seen in the following sections.

1.3 Combustion noise

Combustion noise is generated inside the combustion chamber and has to propagate through turbine blades. The problem of the propagation of acoustic waves through accelerating flows was first studied by Tsien (1952) in a rocket engine combustion instability framework. It was Marble and Candel (1977), however, who first included the propagation of entropy waves through accelerating subsonic and supersonic nozzles, explaining in this way the two mechanisms of combustion noise generation: direct and indirect, as seen in figure 1.4. Direct noise is generated by the acoustic waves produced in the flame region, which travel downstream through the turbine stages to the outlet. Indirect combustion noise is generated by the entropy waves induced by the unsteady combustion process. These waves generate noise when propagating through non-homogeneous flows such as the turbine stages. The two mechanisms generate noise in the low frequency range.

1.3.1 Indirect combustion noise

Any heat release generates entropy through the equation,

$$\frac{\partial s}{\partial t} + \vec{u} \cdot \nabla s = \frac{\dot{Q}}{\rho T} \quad \text{with} \quad s = c_v \ln\left(\frac{p}{\rho^\gamma}\right) \tag{1.1}$$

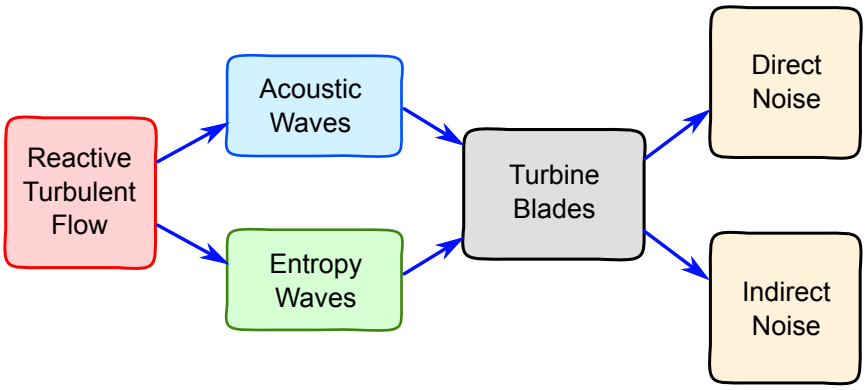

Figure 1.4 – *The two mechanisms of combustion noise.*

where the usual definition of entropy has been used. It is therefore straightforward to conclude (using a linearised form of equation (1.1)) that an unsteady heat release, q', of this heat source (due to turbulence for example) generates a fluctuating entropy term, s', given through

$$\frac{\partial s'}{\partial t} + \vec{u} \cdot \nabla s' = \frac{q'}{\rho T} - \left(\frac{p'}{p} \vec{u} + \vec{u}' \right) \nabla s \quad \text{with} \quad \frac{s'}{c_p} = \frac{p'}{\gamma p} - \frac{\rho'}{\rho}, \tag{1.2}$$

as shown by Dowling et al. (1988), where the mean steady quantities are represented by the non-primed variables for simplicity. This equation shows that entropy fluctuations are generated in two ways: on one hand by the flame's heat-release fluctuations (q') and on the other hand by acoustic fluctuations in regions with mean heat release (second term of the right-hand side). At the same time it shows that once generated, in the region outside of the flame where no mean or fluctuating heat release exists ($\nabla s = 0$ and $q' = 0$), the right-hand side of equation (1.2) is zero and the entropy wave is just convected with the mean flow velocity ($\vec{u}$) when neglecting any flow mixing or diffusion.

Marble and Candel (1977) showed that a one-way coupling between entropy and acoustics appeared when a flow gradient existed in a quasi-1D nozzle. Using the quasi-1D linearised Euler equations for the flow through

the nozzle (neglecting heat release and diffusion)[2],

$$\left[\frac{\partial}{\partial t}+u\frac{\partial}{\partial x}\right]\left(\frac{p'}{\gamma p}\right)+u\frac{\partial}{\partial x}\left(\frac{u'}{u}\right)=0, \tag{1.3a}$$

$$\left[\frac{\partial}{\partial t}+u\frac{\partial}{\partial x}\right]\left(\frac{u'}{u}\right)+\frac{c^2}{u}\frac{\partial}{\partial x}\left(\frac{p'}{\gamma p}\right)=\left[\frac{s'}{c_p}-2\frac{u'}{u}+(\gamma-1)\left(\frac{p'}{\gamma p}\right)\right]\frac{du}{dx}, \tag{1.3b}$$

$$\left[\frac{\partial}{\partial t}+u\frac{\partial}{\partial x}\right]\left(\frac{s'}{c_p}\right)=0, \tag{1.3c}$$

the coupling between entropy and acoustics can be seen on the right-hand side of equation (1.3b), where the entropy waves appears multiplied by the velocity gradient (du/dx). If the flow is homogeneous with no velocity gradient, the right-hand side of equation (1.3b) is zero and the well-known result for acoustic propagation in non-zero but constant Mach number flows is recovered from equations (1.3a) and (1.3b). However, when considering a mean flow gradient, the coupling between convective and acoustic waves appears: the entropy wave acts as a source term in the acoustic equation, generating entropy or indirect combustion noise. This mechanism has been extensively studied from an experimental (Bake et al., 2009), analytical (Williams and Howe, 1975; Howe, 1975; Sinai, 1980; Howe, 2010; Leyko et al., 2011) and numerical point of view (Kostka and Pitsch, 2010; Leyko et al., 2009, 2008; Tam et al., 2012, 2013).

1.3.2 Direct combustion noise

As seen in the second part of equation (1.2), an entropy wave (s') is associated to a density fluctuation (ρ'). In the near region of the flame this fluctuation of density is due to the unsteady heat release, and generates a velocity perturbation (acoustic wave) due to the mass conservation equation. This mechanism generates acoustic waves directly in the flame region as a monopole source (Kotake, 1975) which are propagated through the turbine stages, generating direct combustion noise. In free space, a method based on an acoustic analogy can be used to propagate this noise source. For example, when considering Phillips' analogy (Phillips, 1960), which was extended to reactive flows by Chiu and Summerfield (1974) and Kotake (1975), the wave equation reads,

$$\frac{D^2\pi}{Dt^2}-\frac{\partial}{\partial x_i}\left(c^2\frac{\partial\pi}{\partial x_i}\right)=\frac{D}{Dt}\left[\frac{(\gamma-1)}{\rho c^2}\dot{\omega}_T\right] \tag{1.4}$$

[2]This equation will be derived in Chapter 2 and is given here to illustrate the discussion.

where $\pi = (1/\gamma)\ln(p/p_\infty)$ and $\dot{\omega_T}$ is the heat release of the flame. Only this direct contribution has been retained for simplicity to illustrate the monopole nature of combustion noise at low Mach numbers. Direct combustion noise has been studied analytically (Strahle, 1971, 1972), combining numerical simulations and acoustic analogies (Ihme et al., 2005; Ihme and Pitsch, 2012; Swaminathan et al., 2011; Talei et al., 2011) and experimentally (Rajaram and Lieuwen, 2009).

Direct combustion noise is the major source term in lab-scale combustion chambers, where no acceleration of the entropy waves exist. The indirect mechanism, however, can be of great importance in modern aero-engines due to the large accelerations of the flow in the turbine blades, as seen by (Candel, 1972a; Muthukrishnan et al., 1978; Pickett, 1975). Leyko et al. (2008) showed that, for a 1D model combustor with a choked nozzle, indirect noise can be one order of magnitude larger than direct noise, depending on the mean Mach number in the combustion chamber.

Both mechanisms of combustion noise generation depend strongly on the propagation of waves through turbine stages. Direct noise is shielded by the presence of turbine blades and the successive accelerations and decelerations of the mean flow. On the other hand, entropy noise is generated by these accelerations and decelerations. For this reason, the prediction of combustion noise has focused both on the generation of waves by the flame and on the propagation of waves through these non-uniform flows and the generation of indirect noise.

1.4 Propagation of waves

Acoustic analogies such as Lighthill (1952)'s are widely used in the aeroacoustics community and easily applied with a low computational cost to propagate noise sources in homogeneous flows. The drawback, however, is that the mean flow is considered at rest in the propagation region and therefore indirect noise cannot be predicted using this method and has to be given in advance. Noise sources and noise propagation are considered to be separate and do not interact, which is clearly not the case in combustion

noise. When writing Lighthill's analogy in pressure terms, for example,

$$\begin{aligned}\frac{1}{c_\infty}\frac{\partial^2 p}{\partial t^2}-\frac{\partial^2 p}{\partial x_i^2} &= \frac{\partial^2}{\partial x_i \partial x_j}\left(\rho u_i u_j - \tau_{ij}\right)\\ &+ \frac{\partial}{\partial t}\left[\frac{\rho_\infty}{\rho}\frac{(\gamma-1)}{c^2}\left(\dot{\omega_T}+\sum_k h_k\frac{\partial J_k}{\partial x_k}-\frac{\partial q_i}{\partial x_i}+\tau_{ij}\frac{\partial u_i}{\partial x_j}+\dot{Q}\right)+\rho_\infty\frac{D}{Dt}\left(\ln r\right)\right]\\ &+ \frac{1}{c_\infty}\frac{\partial}{\partial t}\left[\left(1-\frac{\rho_\infty c_\infty^2}{\rho c^2}\right)\frac{Dp}{Dt}-\frac{p-p_\infty}{\rho}\frac{D\rho}{Dt}\right]\\ &+ \frac{\partial^2}{\partial x_j \partial t}\left(\rho_e u_j\right), \end{aligned} \tag{1.5}$$

the indirect combustion noise source (last line) appears on the right-hand side of the wave equation in terms of the excess density, $\rho_e = (\rho - \rho_\infty) - (p - p_\infty)/c_\infty$, introduced by Morfey (1973), as explained by Bailly et al. (2010). This means that the indirect noise mechanism is a source term and has to be given in advance to the wave equation as a known term so as to be propagated by the wave operator (left-hand side). The indirect term must therefore be computed in advance, using LES or other methods. Other acoustic analogies exist which consider the effects of mean flow, but indirect noise is still considered as a noise source and is not computed by the analogy and should be given as a known source term. Indirect noise is generated in the turbine stages and for this reason the turbine should be included in the source computation. However, including the turbine stages in a reactive LES numerical simulation of the combustion chamber is hardly feasible using state-of-the-art computational codes and resources due to the different time-scales involved. Other numerical methods exist, such as coupling the reactive LES codes (for the combustion chamber) with a URANS simulation of the turbine blades (Collado, 2012), used mainly for heat transfer problems.

An alternative method to compute combustion noise was proposed by Leyko (2010) and is continued in this thesis. The method shown in figure 1.5 computes only the combustion chamber using Large Eddy Simulations (LES). The waves are analysed and extracted at the outlet of the combustion chamber and the propagation of the acoustic and entropy waves through the turbine stages (and therefore the generation of direct and indirect noise) is performed using analytical methods based on 1D and 2D solutions of the Linearised Euler Equations. Once the direct and indirect noise terms are obtained at the outlet of the turbine stages, acoustic analogies can be easily used to propagate the noise to the far field.

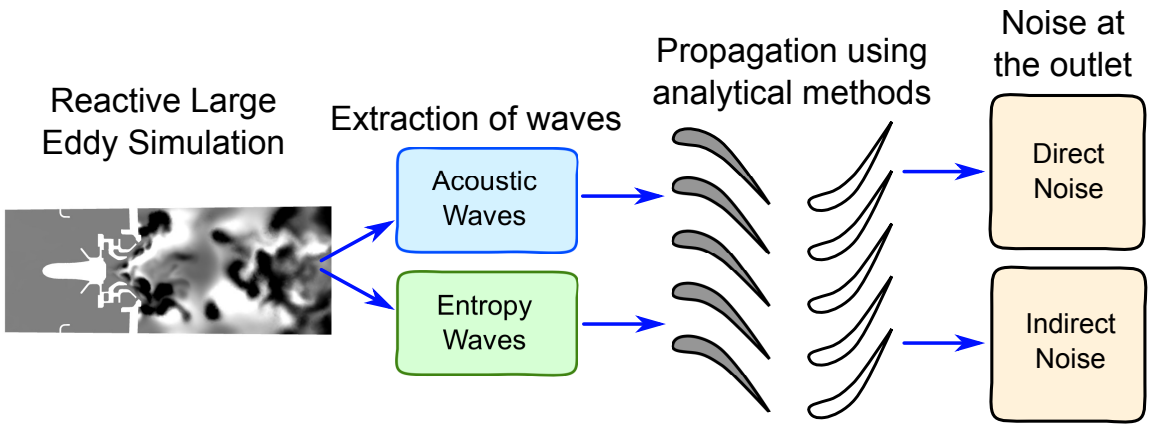

Figure 1.5 – *Methodology to predict combustion noise combining Large Eddy Simulations (LES) and analytical methods.*

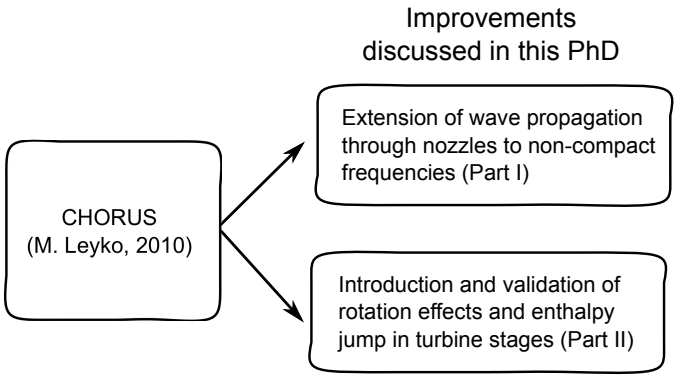

Figure 1.6 – *Developments made in this PhD.*

This hybrid approach combines high fidelity 3D LES for the chamber with analytical methods for the propagation of waves through the turbine. Multiple improvements were still under discussion when this PhD started and are addressed in this PhD (figure 1.6),

- The analytical approach of Marble and Candel (1977) was valid only in the limit of low frequency (compact nozzle), an assumption which was removed in the present work (Part I).

- The rotating blades as well as the enthalpy jump created by them were not considered in the analytical method. This was included in this PhD and is described and validated in Part II.

1.5 Objectives and organisation of this thesis

The present research work focuses on the generation and propagation of direct and indirect combustion noise. The analytical methods for the propagation of waves through non-uniform flows are first studied and validated using numerical simulations. The method is then used to compute the noise of an aero-engine. The rest of the thesis is divided into three different parts (table 1.1):

- **Part I**: Propagation of waves through non-uniform quasi-1D flows. This part presents a quasi-1D study of the propagation of waves through nozzles and the generation of indirect combustion noise from an analytical point of view. Previous analytical models and their assumptions are reviewed and a general analytical solution is proposed to obtain the transmission and reflection coefficients of acoustic and entropy waves propagating through subsonic and choked nozzles as a function of frequency. This includes the propagation of acoustic waves to generate direct noise, and the generation of indirect noise by the acceleration of entropy waves. This general solution is validated with other models, numerical simulations and with experimental data. Results show that the transfer functions of the nozzle have a strong dependency on both frequency and on the exact nozzle profile.

- **Part II**: Propagation of waves through turbine stages. The analytical two-dimensional model for the propagation of acoustic, entropy and vorticity waves through turbine blades of Cumpsty and Marble (1977) is compared with numerical simulations in order first to validate the analytical solution, and secondly to evaluate the range of validity of the solution. To begin with, the analytical method is explained in Chapter 5. The numerical simulations are then explained in chapter 6, first for the single rotating blade, then for the stator-rotor stage. Results are shown to agree with the analytical model at zero frequency. This compact solution is found to agree with the numerical simulations for the low frequency range, as expected from the assumptions made. The deformation of entropy waves is also studied as it is considered to affect the global indirect noise generation.

- **Part III**: Predicting combustion noise combining LES and analytical

Part I 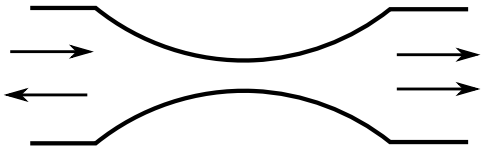	Extension of the Marble and Candel (1977) analytical method to non-zero frequencies (1D).
Part II 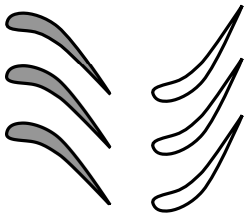	A 2D analytical low-order model for the propagation of waves through turbine blades, including stator and rotor, enthalpy jump and flow deviation effects. Validation of the model using numerical simulations.
Part III 	CHORUS methodology: Description of the hybrid method used to compute combustion noise combining LES and low-order analytical models for the propagation of waves through the turbine. Application to a real aero-engine.

Table 1.1 – *Organisation of this manuscript.*

tools for the propagation of waves. This part presents the numerical tool used to compute combustion noise and the propagation of waves through turbine stages, started during the PhD of Leyko (2010) and continued during this work. This tool is based on the combination of a compressible reactive LES simulation of a combustion chamber with analytical methods to propagate acoustic, entropy and vorticity waves through turbine stages. An industrial case is considered and analysed, computing the acoustic and entropy waves generated at the outlet of the combustion chamber and the propagation of this waves to generate direct and indirect noise at the outlet of the engine.

Part I

Propagation of waves through non-uniform quasi-1D flows

Table of Contents

Introduction **17**

2 State of the art **21**

2.1 The flow through a quasi-1D nozzle 21

2.1.1 Steady flow 23

2.1.2 Linearised Euler equations 25

2.2 The compact nozzle method 27

2.3 Linear mean velocity profile nozzle method 30

2.4 Asymptotic expansion of the linearised Euler equations 34

3 The invariant method **37**

3.1 The invariant equation 38

3.2 The Magnus expansion 40

3.2.1 Solution for larger frequencies 43

3.3 Boundary conditions 44

3.3.1 Subsonic flow 45

3.3.2 Choked flow 47

3.3.3 Supersonic flow with a shock wave 49

4 Nozzle transfer functions at non-compact frequencies **55**

4.1 Comparison with a linear steady velocity choked nozzle . . . 56

4.2 Comparison with the 'equivalent nozzle length' method for choked nozzles 63

4.3 Comparison with experimental measurements 69

4.4 Study of subsonic nozzles 71

4.5 Parametric study on direct and indirect combustion noise . . . 76

Conclusions **81**

Introduction

The study of the propagation of acoustic and entropy fluctuations through a one-dimensional nozzle is of great importance when dealing with both combustion noise and thermoacoustic instabilities. Marble and Candel (1977) showed that acoustic and entropy waves generated in the combustion chamber of aircraft or helicopter engines contributed significantly to the total engine noise. Two mechanisms control combustion noise generation, related to the propagation of these two waves to the outlet of the engine as explained in Section 1.3: direct noise, generated when acoustic waves pass through the turbine stages, and indirect noise, a mechanism in which entropy waves generate noise when accelerated with the mean flow. The latter source can contribute significantly to the total noise (Candel, 1972b; Pickett, 1975; Muthukrishnan et al., 1978). Recent studies (Bake et al., 2009; Howe, 2010; Leyko et al., 2009, 2008) have shown that the propagation of waves through non-uniform flows plays a major role on the generation and attenuation of combustion noise.

Similarly, when studying thermoacoustic instabilities in combustion chambers of gas turbines, the propagation of acoustic and entropy waves through the inlet and the outlet of the chamber has a significant effect because it controls impedances seen by the combustion chamber upstream and downstream (Poinsot and Veynante, 2011). Waves generated by the turbulent flame inside the combustion chamber are reflected at the compressor and turbine stages and interact with the flame. The flame reacts to the acoustic perturbation, generating a fluctuating heat release that will in turn produce more acoustic waves. If this fluctuating heat release and the acoustic waves are in phase, a positive feedback will occur as shown by Rayleigh (1878), Dowling (1997) and Dowling and Stow (2003). This may lead to thermoacoustic instabilities if the energy gain exceeds the losses through boundaries and other dissipation mechanisms (Gullaud

et al., 2009). The instability mechanism depends strongly on the boundary conditions of the combustion chamber: the phase of the reflection coefficient will influence the resonance frequency at which the instability occurs, and the modulus will control the rate at which the energy of the instability is lost through the boundaries, determining whether the mode is stable or unstable (Williams, 1985; Candel and Poinsot, 1988; Culick, 1988; Dowling, 1995).

The propagation of waves through nozzles was first studied by Tsien (1952), who analysed the propagation of acoustic waves through a quasi one-dimensional nozzle with a spatially linear velocity profile. Marble and Candel (1977) extended this result to consider entropy waves and obtained the wave-transfer functions of the nozzle using the compact assumption for both subsonic and choked nozzles, showing that entropy waves generated acoustic perturbations when accelerated through a nozzle. This compact hypothesis considers the axial length of the nozzle to be small compared to the wavelength of the perturbation, limiting the results to low frequencies. The frequency dependence of the transfer functions of the nozzle has been studied using mainly two approaches. The first approach was to consider a specific nozzle geometry. This was done by Marble and Candel (1977), following the work of Tsien (1952), in which the nozzle was supposed to have a linear velocity profile. For this very specific case, an analytical solution was obtained in the form of a hypergeometric differential equation. Moase et al. (2007) extended the non-compact analysis for a choked nozzle with a shock wave, where the steady velocity was approximated as piecewise linear and computed using the solution of Marble and Candel (1977). For each interval with a linear velocity profile, the hypergeometric equation was solved and coupled to the adjacent intervals to compute the complete solution of the nozzle. A different approach for studying the non-compact effect was proposed by Stow et al. (2002). They used an asymptotic analysis to calculate the first order correction to the low-frequency hypothesis in the case of a choked nozzle with no specific assumption on the nozzle geometry, and used this analysis to obtain an effective nozzle length that corrects the phase prediction of the reflection coefficient. Goh and Morgans (2011a) used this result to extend the effective nozzle length to compute the transmission coefficients of a choked flow. There are other methods used in the literature, such as Campos (1987) which is based on a low-Mach number assumption.

It has been shown (Duran et al., 2013c) that subsonic converging/diverging nozzles exhibit strong non-compact effects both in the

modulus and in the phase of the transfer functions. Work done by Marble and Candel (1977) and by Moase et al. (2007) showed that the modulus of the transfer functions of choked nozzles changes significantly with frequency. When considering gas turbines, the modulus of the reflection coefficient represents energy loss through the boundary conditions (for thermoacoustic instability applications), and the transmission coefficient represents the acoustic energy propagated downstream (in combustion noise applications). The objective of this section is to study the propagation of waves through non-uniform quasi-1D flows analytically, starting from the compact method of Marble and Candel (1977) and extending analytically this method to non-zero frequencies, removing the compact nozzle assumption to study the evolution of both modulus and phase of the transfer functions at non-zero frequencies for any geometry and any flow configuration using a new asymptotic expansion method.

Two major assumptions are made in this section: first the flow is considered quasi one-dimensional and only plane waves are considered through the nozzle, and secondly the Euler equations are used, neglecting viscous terms. The first hypothesis considers that the nozzle is long compared to its characteristic transversal length (for the flow to remain quasi-1D), and that the waves verify $\lambda > l_y$, where l_y is the characteristic length in the transverse direction and λ the wavelength of the perturbation ($\lambda = c/f$, with c the sound speed and f the frequency). This last condition limits the results to frequencies under the first cut-off frequency of the transverse modes of the nozzle. The second hypothesis assumes that viscous effects occur in a negligible zone of the flow, and has been frequently used in the literature (Marble and Candel, 1977; Stow et al., 2002; Moase et al., 2007). The effect of viscosity in the propagation of waves through quasi-one-dimensional flows is double: First the development of a steady boundary layer modifies the mean flow calculated using the Euler equations. This effect can be modelled by considering a displacement length of the boundary layer, which reduces the effective section of the nozzle and changes therefore the mean flow configuration through which waves propagate. This modifies the propagation of waves and therefore the transfer functions. This correction may, however, be very important in certain conditions, as the reduction of cross-sectional area through the displacement length of the boundary layer may lead to a choked flow instead of a subsonic one, for example. The propagation of entropy and acoustic waves through the viscous boundary layer is not modelled through the displacement length, but this can be neglected if the boundary layer is small compared to the characteristic section (no flow separation occurs in

the divergent region of the nozzle). The second effect of viscosity is the dissipation of acoustic and entropy waves, which occurs only at large frequencies and is neglected in most acoustic propagation models. In addition to these assumptions, the mean flow is supposed to be unaltered by the acoustic and entropy disturbances: the disturbances propagating through it do not lead to oscillations of the flow regime between subsonic and choked conditions and they induce no flow separation. The interaction of shock waves with the boundary layer and with turbulence, as studied by Ribner (1953, 1954, 1987), is also neglected in this quasi one-dimensional solution. Regardless of these simplifications, it is interesting to obtain an analytical solution of the quasi one-dimensional Euler equations using the asymptotic expansion in order to compute the transmission and reflection coefficient of waves through nozzles. This could be used later to provide more realistic boundary conditions for LES of actual complex full annular combustion chambers (Gicquel et al., 2012) and to predict both combustion instabilities (Motheau et al., 2012) and waves transmitted to the turbine stages.

The following chapters are organised as follows: Chapter 2 summarises the basic equations that will be used to solve the flow through a quasi-1D nozzle and gives some insight on previous methods used in the literature to calculate analytically the acoustic and entropy transfer functions. Chapter 3 provides a more general analytical solution of the linearised Euler equations given through the Magnus expansion in which no assumption is made on the geometry of the nozzle. Results and comparisons between methods and with experimental data are illustrated in Chapter 4 for different nozzle geometries and configurations and conclusions are finally drawn.

Chapter 2

State of the art

In this chapter, an overview of previous analytical methods for analytically calculating the propagation of waves through non-uniform quasi-1D flows will be given.

The steady flow through a high-Reynolds-number quasi-1D nozzle can be easily calculated applying the Euler equations. This is not the case, however, when analysing the unsteady flow, which is the case for the propagation of acoustic waves. However, since acoustic variables are generally small compared to the mean quantities, it is possible to linearise the Euler equations (LEE) about a steady mean flow and solve these equations instead. In this chapter, the basic equations of the quasi-1D nozzle will be presented in Section 2.1 in the case of both the steady flow and the LEE formulation. This will be followed by a summary of previous methods used in the literature to solve the LEE analytically to obtain the transfer functions of the nozzle: the compact method will be presented first (Section 2.2), where the frequency of the perturbations is considered small; two methods to deal with the non-compact case will then be presented in Sections 2.3 and 2.4.

2.1 The flow through a quasi-1D nozzle

In this section a short summary of the basic equations used in this chapter is provided. The reader is referred to more general fluid mechanics and

acoustics books for details on the derivations (Batchelor, 1988; Pierce, 1981; Howe, 1998).

The starting point for studying the flow through a nozzle is to write out the Navier-Stokes equations for an ideal compressible fluid, which describe its motion, namely

$$\frac{\partial \rho}{\partial t} + \nabla \cdot (\rho \mathbf{u}) = 0, \tag{2.1a}$$

$$\frac{\partial (\rho \mathbf{u})}{\partial t} + \nabla \cdot (\rho \mathbf{u}\mathbf{u}) = \nabla \cdot (-p\mathcal{I} + \tau), \tag{2.1b}$$

$$\rho T \left(\frac{\partial s}{\partial t} + \mathbf{u} \cdot \nabla s \right) = \nabla \cdot (k \nabla T) + \phi_v, \tag{2.1c}$$

where the primitive variables are the density, ρ; the pressure, p, and the velocity vector, $\mathbf{u}$. $\mathcal{I}$ is the identity matrix, τ the viscous stress tensor, k the thermal conductivity and ϕ_v the Rayleigh dissipation function (Liñán, 2005). The flow is considered adiabatic and therefore no heat addition or combustion is considered in these equations. The entropy, s, is related to the state variables through $Tds = c_v dT + pd(1/\rho)$ for a calorically perfect gas, with T the temperature and c_v the specific heat capacity at constant volume. After applying the usual ideal gas law, $p = \rho r T$ and with the relations $r = c_p - c_v$ and $\gamma = c_p/c_v$, the entropy is written as a function of the density and pressure, namely

$$s = c_v \ln \left(\frac{p}{\rho^\gamma} \right). \tag{2.2}$$

These equations have to be combined with the appropriate boundary conditions to be solved correctly. The set of equations can be further simplified under reasonable assumptions: for high Reynolds number flows the viscous terms are important in the boundary layer only, where the velocity gradients are strong due to the no-slip condition. This boundary layer is small compared to the nozzle characteristic length (typically its radius), and therefore neglected when no flow separation exists. Similarly, heat conduction is neglected and the flow is said to be reversible, which, when combined with the adiabatic condition, is said to be isentropic, giving the Euler equations,

$$\frac{\partial \rho}{\partial t} + \nabla \cdot (\rho \mathbf{u}) = 0, \tag{2.3a}$$

$$\frac{\partial (\rho \mathbf{u})}{\partial t} + \nabla \cdot (\rho \mathbf{u}\mathbf{u}) = \nabla \cdot (-p\mathcal{I}), \tag{2.3b}$$

$$\frac{\partial s}{\partial t} + \mathbf{u} \cdot \nabla s = 0, \tag{2.3c}$$

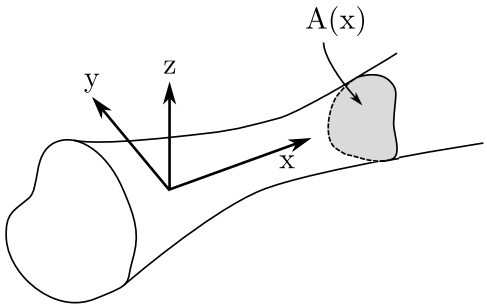

Figure 2.1 – *A quasi-1D nozzle.*

The quasi-one-dimensional assumption can be used to further simplify the 3D Euler equations. Under this assumption, the cross-section of the nozzle, $A(x)$ is supposed to vary slowly with the axial coordinate x as seen in figure 2.1. The flow velocity is considered to occur only in this direction, neglecting the transverse components, and to be constant in the cross-section, giving $\mathbf{u} = u(x)\mathbf{i}$ where $\mathbf{i}$ is the unitary vector in the axial direction. Considering this assumption, the Euler equations are integrated over the transverse section, giving

$$\frac{\partial(\rho A)}{\partial t} + \frac{\partial(u\rho A)}{\partial x} = 0 \tag{2.4a}$$

$$\left[\frac{\partial}{\partial t} + u\frac{\partial}{\partial x}\right](u) + \frac{1}{\rho}\frac{\partial p}{\partial x} = 0 \tag{2.4b}$$

$$\left[\frac{\partial}{\partial t} + u\frac{\partial}{\partial x}\right]s = 0. \tag{2.4c}$$

This set of equations will be the starting-point for the study the propagation of waves through quasi-1D nozzles. For this study, the steady flow through the nozzle will be first briefly described in Section 2.1.1, followed by the derivation of the linearised Euler equations from equation (2.4) in Section 2.1.2.

2.1.1 Steady flow

For the case of a steady flow, the quasi-1D Euler equations of (2.4) can be recast to give three magnitudes which are conserved through the nozzle: the mass, total enthalpy and entropy. For the mass and entropy, the result is

easily obtained from equations (2.4a) and (2.4c), giving

$$\dot{m} = \rho u A = \dot{m}_0, \tag{2.5}$$

$$s = s_0, \tag{2.6}$$

where the subscript $_0$ represents the inlet conditions. For the total enthalpy, its definition ($h_t = h + u^2/2$) is used, with the thermodynamic relation $dh = Tds + (1/\rho)dp$. Combining equations (2.4b) and (2.4c) a conservation equation for the total enthalpy is obtained,

$$\left[\frac{\partial}{\partial t} + u\frac{\partial}{\partial x}\right] h_t = \frac{1}{\rho}\frac{\partial p}{\partial t}, \tag{2.7}$$

from where it can be seen that the enthalpy is conserved through the nozzle when considering the steady flow. Using the total enthalpy definition and considering an ideal gas, it can be shown that $h_t = c_p T_t$ with T_t being the total temperature,

$$T_t = T + \frac{u^2}{2c_p} = T\left(1 + \frac{\gamma - 1}{2} M^2\right), \tag{2.8}$$

which is conserved through the nozzle. In equation (2.8) $M = u/c$ is the Mach number, and $c = \sqrt{\gamma r T}$ the sound speed. It should be noted that even if total temperature and entropy are two measures of energy, the first one is a linear combination of the internal energy with the momentum equation, containing in this way the kinetic energy and therefore resulting in an independent magnitude.

The conservation of entropy through the nozzle can be used to show that, in this isentropic flow, the magnitude given by $p/(\rho)^\gamma$ is also conserved. This leads to the definition of the total or stagnation variables, which are conserved through the nozzle,

$$\rho_t = \rho\left(1 + \frac{\gamma - 1}{2} M^2\right)^{\frac{1}{\gamma - 1}}, \tag{2.9a}$$

$$T_t = T\left(1 + \frac{\gamma - 1}{2} M^2\right), \tag{2.9b}$$

$$p_t = p\left(1 + \frac{\gamma - 1}{2} M^2\right)^{\frac{\gamma}{\gamma - 1}}. \tag{2.9c}$$

Using the mass flow conservation, a relation between the flow Mach number and the cross-section can be found up to a constant value, namely

$$\frac{A_*}{A} = M\left[\left(\frac{2}{\gamma + 1}\right)\left(1 + \frac{\gamma - 1}{2} M^2\right)\right]^{-\frac{\gamma + 1}{2(\gamma - 1)}}, \tag{2.10}$$

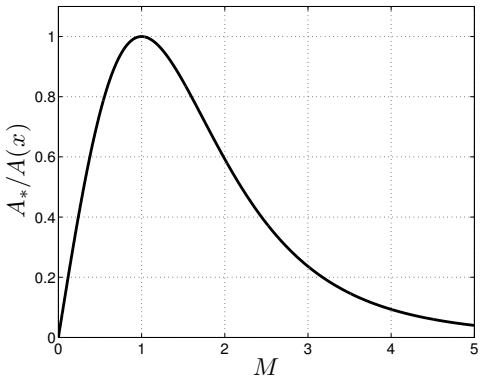

Figure 2.2 – *Mach number as a function of the cross-section ratio.*

where the value of the cross-section at the point where $M = 1$, A_*, is taken as reference (independently of whether such a point exists in the nozzle) and is found by imposing the boundary conditions. This implicit equation can be solved for each cross-section to obtain the local Mach number as a function of the axial coordinate. Once done, any other variable can be calculated through the relations given in equation (2.9).

Equation (2.10) is plotted in figure 2.2, showing that the minimum value of A is A_*, which means that if the flow reaches $M = 1$ this should occur in the nozzle throat. For any other value of the cross-section ratio, two possible values of the Mach number exist: a subsonic and a supersonic one. From figure 2.2 it can be seen that a subsonic flow is accelerated when the area decreases (convergent region) and decelerates when the area increases (divergent region), while when the flow is supersonic the opposite occurs.

2.1.2 Linearised Euler equations

The unsteady quasi-1D linearised Euler equations of (2.4) have to be solved numerically in the general case. However, when considering small fluctuations around the mean flow, the equations can be linearised to obtain a set of equations for the perturbations only. The flow variables are written in this way as the sum of a mean and a fluctuating part, $\phi = \bar{\phi} + \phi'$, where $\bar{(\ )}$ denotes the mean and $(\ )'$ the fluctuating part. The $\bar{(\ )}$ symbol will be however dropped for simplicity in notation hereafter. Doing so in the entropy definition, a relation between the entropy, pressure and density

fluctuations is obtained,

$$\frac{s'}{c_p} = \frac{\rho'}{\rho} - \frac{p'}{\gamma p}. \tag{2.11}$$

Using the unsteady Euler equations of (2.4) and neglecting high order terms of the fluctuations, the linearised Euler equations follow,

$$\left[\frac{\partial}{\partial t} + u\frac{\partial}{\partial x}\right]\left(\frac{p'}{\gamma p}\right) + u\frac{\partial}{\partial x}\left(\frac{u'}{u}\right) = 0, \tag{2.12a}$$

$$\left[\frac{\partial}{\partial t} + u\frac{\partial}{\partial x}\right]\left(\frac{u'}{u}\right) + \frac{c^2}{u}\frac{\partial}{\partial x}\left(\frac{p'}{\gamma p}\right) + \left[2\frac{u'}{u} - (\gamma - 1)\left(\frac{p'}{\gamma p}\right)\right]\frac{du}{dx} = \frac{s'}{c_p}\frac{du}{dx}, \tag{2.12b}$$

$$\left[\frac{\partial}{\partial t} + u\frac{\partial}{\partial x}\right]\left(\frac{s'}{c_p}\right) = 0. \tag{2.12c}$$

The entropy term on the right-hand side of equation (2.12b) is responsible for the generation of indirect or entropy noise, as explained in the introduction. This term is non-zero when a mean velocity gradient exists in the nozzle.

When the mean flow is homogeneous, $du/dx = 0$ and the equations can be combined to give three decoupled equations with three unknowns, known as the characteristic equations, as shown by Thompson (1987),

$$\left[\frac{\partial}{\partial t} + (u + c)\frac{\partial}{\partial x}\right](w^+) = 0, \tag{2.13a}$$

$$\left[\frac{\partial}{\partial t} + (u - c)\frac{\partial}{\partial x}\right](w^-) = 0, \tag{2.13b}$$

$$\left[\frac{\partial}{\partial t} + u\frac{\partial}{\partial x}\right](w^s) = 0, \tag{2.13c}$$

with

$$w^+ = \frac{p'}{\gamma p} + \frac{u'}{c}, \qquad w^- = \frac{p'}{\gamma p} - \frac{u'}{u} \qquad \text{and} \qquad w^s = \frac{s'}{c_p}, \tag{2.14}$$

which are the two acoustic and the entropy waves propagating through the nozzle with speeds $u + c$, $u - c$ and u, and therefore define which boundary conditions can be imposed at each boundary as seen in figure 2.3, depending on which waves are incoming and which are outgoing. When the mean flow is non-homogeneous the system of equations is not so simple and the acoustic

and entropy waves are coupled through the mean flow gradient[1],

$$\left[\frac{\partial}{\partial t}+(u+c)\frac{\partial}{\partial x}\right](w^+)=\left\{\left[\frac{\eta^-}{M}-\beta^+\right]w^+-\left[\frac{\eta^-}{M}+\beta^-\right]w^--\zeta w^s\right\}\frac{dM}{dx}, \tag{2.15a}$$

$$\left[\frac{\partial}{\partial t}+(u-c)\frac{\partial}{\partial x}\right](w^-)=\left\{\left[\beta^+-\frac{\eta^+}{M}\right]w^++\left[\frac{\eta^+}{M}+\beta^-\right]w^-+\zeta w^s\right\}\frac{dM}{dx}, \tag{2.15b}$$

$$\left[\frac{\partial}{\partial t}+u\frac{\partial}{\partial x}\right](w^s)=0. \tag{2.15c}$$

The rest of this chapter presents a review of previous methods for solving the set of equations given in (2.12), including the mean flow gradient, using different analytical approaches and assumptions.

2.2 The compact nozzle method

The transfer functions between the upstream and downstream waves of the nozzle were obtained by Marble and Candel (1977) using the compact nozzle assumption, which states that the wavelengths of the acoustic and entropy perturbations are large compared to the axial length of the nozzle. This assumption is therefore valid for low-frequency perturbations only. Using this assumption, acoustic and entropy waves propagate quasi-steadily through the nozzle, and matching conditions can be written between the region upstream of the nozzle (noted with the subscript $_0$ in figure 2.3) and the region downstream of the nozzle (noted as $_1$) for the conservative variables mass flow rate, total temperature and entropy. They read

$$\left(\frac{\dot{m}'}{\dot{m}}\right)_0=\left(\frac{\dot{m}'}{\dot{m}}\right)_1, \tag{2.16a}$$

$$\left(\frac{T_t'}{T_t}\right)_0=\left(\frac{T_t'}{T_t}\right)_1, \tag{2.16b}$$

$$\left(\frac{s'}{c_p}\right)_0=\left(\frac{s'}{c_p}\right)_1, \tag{2.16c}$$

where the unaccented variables represent the mean steady flow and primed variables, $(\cdot)'$, represent small perturbations. To obtain the wave transfer

[1] These equations are derived in Chapter 3, equation (3.29), and are given here to illustrate the discussion. $\eta^\pm$, $\beta^\pm$ and ζ are functions of the Mach number used to simplify the equations, given in (3.28).

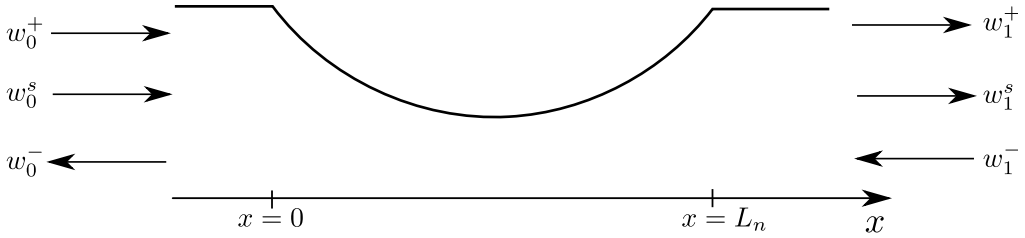

Figure 2.3 – *Sketch of the acoustic and entropy waves in a subsonic converging-diverging nozzle.*

functions the mass, total temperature and entropy perturbations are first written as functions of three primitive variables: the dimensionless pressure, velocity and entropy fluctuations,

$$\varphi = \frac{p'}{\gamma p}, \qquad \nu = \frac{u'}{u} \qquad \text{and} \qquad \sigma = \frac{s'}{c_p}. \tag{2.17}$$

It follows that

$$\left(\frac{\dot{m}'}{\dot{m}}\right) = \varphi + \nu - \sigma, \tag{2.18a}$$

$$\left(\frac{T_t'}{T_t}\right) = (\gamma - 1)\frac{M^2\nu + \varphi + \dfrac{\sigma}{\gamma - 1}}{1 + \dfrac{\gamma - 1}{2}M^2}, \tag{2.18b}$$

$$\left(\frac{s'}{c_p}\right) = \sigma. \tag{2.18c}$$

When considering a subsonic flow, three boundary conditions can be imposed, corresponding to the downstream-propagating acoustic wave at the inlet (w_0^+), the entropy wave at the inlet (w_0^s) and the upstream-propagating acoustic wave at the outlet (w_1^-), as seen in figure 2.3. These waves can be expressed as functions of the primitive variables in a nondimensional form as done by Leyko et al. (2009); Moase et al. (2007); Stow et al. (2002), and as shown in Section 2.1.2,

$$w^+ = \varphi + M\nu, \qquad w^- = \varphi - M\nu \qquad \text{and} \qquad w^s = \sigma. \tag{2.19}$$

Note that these definitions differ from those used by Marble and Candel (1977) by a factor 1/2 in the two acoustic waves, and therefore a factor 1/2 will appear in some terms of the final solution. Using (2.19) in (2.18) and combining them with the jump conditions in (2.16), Marble and Candel

	w_0^-	w_1^+
Response to $w_0^+ = 1$	$\frac{M_1 - M_0}{1 - M_0} \frac{1 + M_0}{M_0 + M_1} \frac{1 - \frac{1}{2}(\gamma - 1)M_0 M_1}{1 + \frac{1}{2}(\gamma - 1)M_0 M_1}$	$\frac{2M_1}{1 + M_1} \frac{1 + M_0}{M_0 + M_1} \frac{1 + \frac{1}{2}(\gamma - 1)M_1^2}{1 + \frac{1}{2}(\gamma - 1)M_0 M_1}$
Response to $w_0^s = 1$	$-\frac{M_1 - M_0}{1 - M_0} \frac{M_0}{1 + \frac{1}{2}(\gamma - 1)M_0 M_1}$	$\frac{M_1 - M_0}{1 + M_1} \frac{M_1}{1 + \frac{1}{2}(\gamma - 1)M_0 M_1}$
Response to $w_1^- = 1$	$\frac{2M_0}{1 - M_0} \frac{1 - M_1}{M_0 + M_1} \frac{1 + \frac{1}{2}(\gamma - 1)M_0^2}{1 + \frac{1}{2}(\gamma - 1)M_0 M_1}$	$-\frac{M_1 - M_0}{1 + M_1} \frac{1 - M_1}{M_0 + M_1} \frac{1 - \frac{1}{2}(\gamma - 1)M_0 M_1}{1 + \frac{1}{2}(\gamma - 1)M_0 M_1}$

Table 2.1 – *Compact acoustic and entropy transfer functions in a subsonic nozzle.*

(1977) obtained a set of three equations with three unknown outgoing waves and three imposed incoming waves. Considering a unitary incoming entropy wave and no acoustic waves, the entropy transfer functions are obtained and indicate how much acoustic energy is reflected and transmitted by the nozzle when it is hit by an entropy wave. Similarly, the acoustic transfer functions can be calculated by setting $w_0^s = w_1^- = 0$ and imposing a unitary downstream-propagating acoustic wave w_0^+. The transfer functions for the upstream-propagating acoustic wave at the outlet are obtained by imposing $w_0^s = w_0^+ = 0$. These results are summarised in Table 2.1.

For a flow choked at the throat, the acoustic wave w_1^- at the outlet cannot be imposed, as it propagates downstream. Marble and Candel (1977) imposed the choked flow condition by stating that the fluctuations of the reduced mass flow rate are zero at the inlet. This is equivalent to stating that the Mach number fluctuations are zero at the throat, and by using the compact equations (2.16) it is shown that this holds similarly at the nozzle inlet and outlet. The condition can be written as a function of the primitive variables as

$$\frac{M'}{M} = \nu - \frac{\gamma - 1}{2}\varphi - \frac{\sigma}{2} = 0. \tag{2.20}$$

It should be noted that this condition holds for any frequency at the nozzle throat only, as the Mach number should be 1 at this point and no fluctuations of the Mach number can be present. It is only in the compact case that the condition can be shown to hold at any point of the nozzle, which leads to stating that the reduced mass flow rate is choked. Using this extra condition

	w_0^-	w_1^+	w_1^-
Response to $w_0^+ = 1$	$\frac{1-\frac{1}{2}(\gamma-1)M_0}{1+\frac{1}{2}(\gamma-1)M_0}$	$\frac{1+\frac{1}{2}(\gamma-1)M_1}{1+\frac{1}{2}(\gamma-1)M_0}$	$\frac{1-\frac{1}{2}(\gamma-1)M_1}{1+\frac{1}{2}(\gamma-1)M_0}$
Response to $w_0^s = 1$	$\frac{-M_0}{1+\frac{1}{2}(\gamma-1)M_0}$	$\frac{M_1-M_0}{2\left(1+\frac{1}{2}(\gamma-1)M_0\right)}$	$\frac{-(M_1+M_0)}{2\left(1+\frac{1}{2}(\gamma-1)M_0\right)}$

Table 2.2 – *Compact acoustic and entropy transfer functions of a choked nozzle.*

and some algebra, the transfer functions can be calculated for the choked flow and are given in Table 2.2. It is interesting to note that, in the choked case, (2.16a), (2.16c) and (2.20) lead to the statement that φ, ν and σ are constant throughout the nozzle. Note also that the reflected wave w_0^- does not depend on the outlet Mach number when the flow is choked, as the information on the outlet Mach number cannot travel upstream from the nozzle throat.

The transfer function written hereafter as

$$\begin{bmatrix} \frac{w_0^-}{w_0^+} \end{bmatrix} \tag{2.21}$$

represents the upstream acoustic wave, w_0^-, generated at the inlet by a unitary downstream-propagating acoustic wave at the inlet, w_0^+, and is called the reflection coefficient of the nozzle. The downstream-propagating acoustic wave, w_1^+, generated by a unitary entropy wave, w_0^s, is simply known as the indirect noise (noise generated indirectly by entropy waves).

2.3 Linear mean velocity profile nozzle method

The compact assumption provides an easy analytical solution for the low-frequency case. To study the transfer functions at non-compact frequencies, Marble and Candel (1977) proposed an analytical method to solve the linearised Euler equations (2.12) in a nozzle with a linear steady velocity profile. Using the subscript $(\cdot)_*$ for quantities taken at the choked section, the dimensionless time and space coordinates can be defined as $\hat{\tau} = tc_*/x_*$ and

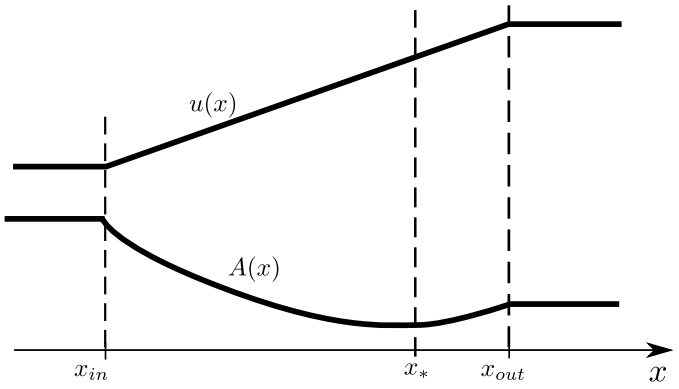

Figure 2.4 – *Sketch of a linear mean velocity profile nozzle.*

$\hat{\xi} = (x/x_*)^2 = (u/u_*)^2$ if $x = 0$ is taken where $u = 0$ (even if this point is extrapolated outside the computational domain)[2]. The Mach number of such a linear velocity profile nozzle can be calculated as a function of the space coordinate using the definition of $\hat{\xi}$,

$$\hat{\xi} = \left(\frac{x}{x_*}\right)^2 = \left(\frac{u}{u_*}\right)^2 = \left(\frac{\gamma+1}{2}\right)\frac{M^2}{1+\frac{\gamma-1}{2}M^2}, \tag{2.22}$$

and solving for the Mach number,

$$M = \sqrt{\left(\frac{2}{\gamma+1}\right)\frac{\hat{\xi}}{1-\left(\frac{\gamma-1}{\gamma+1}\right)\hat{\xi}}}. \tag{2.23}$$

Using equation (2.10) the dimensionless cross-section is obtained. Figure 2.4 shows a sketch of a linear mean velocity profile nozzle.

Marble and Candel (1977) used the dimensionless variables previously defined to transform (2.12) into

$$\left[\frac{\partial}{\partial\hat{\tau}} + 2\hat{\xi}\frac{\partial}{\partial\hat{\xi}}\right](\varphi) + 2\hat{\xi}\frac{\partial}{\partial\hat{\xi}}(\nu) = 0, \tag{2.24a}$$

$$\left[\frac{\partial}{\partial\hat{\tau}} + 2\hat{\xi}\frac{\partial}{\partial\hat{\xi}}\right](\nu) + \left[\frac{\gamma-1}{\hat{\xi}} - \gamma + 1\right]\hat{\xi}\frac{\partial}{\partial\hat{\xi}}(\varphi) + 2\nu - (\gamma-1)\varphi - \sigma = 0, \tag{2.24b}$$

$$\left[\frac{\partial}{\partial\hat{\tau}} + 2\hat{\xi}\frac{\partial}{\partial\hat{\xi}}\right](\sigma) = 0. \tag{2.24c}$$

[2]Note that the dimensionless quantities in this section, noted with ($\hat{}$), are reduced using the value of the primitive variables at the choked throat, as done by Marble and Candel (1977).

Assuming that the disturbances are harmonic, $\varphi = P(\hat{\xi})\exp(i\hat{\Omega}\hat{\tau})$, $\nu = U(\hat{\xi})\exp(i\hat{\Omega}\hat{\tau})$ and $\sigma = \sigma(\hat{\xi})\exp(i\hat{\Omega}\hat{\tau})$ are used, with $\hat{\Omega} = 2\pi f x_*/c_*$. The entropy equation (2.24c) is directly solved, giving

$$\sigma = \sigma_r \left(\frac{\hat{\xi}}{\hat{\xi}_r}\right)^{-i\hat{\Omega}/2}, \tag{2.25}$$

where ξ_r is the point where the reference value of the entropy wave is taken (the inlet). This result is combined with (2.24a) and (2.24b) to obtain an hypergeometric equation for P,

$$\hat{\xi}(1-\hat{\xi})\frac{d^2P}{d\hat{\xi}^2} - \left[2 + \frac{2i\hat{\Omega}}{\gamma+1}\right]\hat{\xi}\frac{dP}{d\hat{\xi}} - \frac{i\hat{\Omega}(2+i\hat{\Omega})}{2(\gamma+1)}P = -\sigma_r \frac{i\hat{\Omega}}{2(\gamma+1)}\left(\frac{\hat{\xi}}{\hat{\xi}_r}\right)^{-i\hat{\Omega}/2}, \tag{2.26}$$

where $U(\hat{\xi})$ has been eliminated. Once this equation is solved, $U(\hat{\xi})$ is given by

$$\left(2 + i\hat{\Omega}\right)U = -(\gamma+1)(1-\hat{\xi})\frac{dP}{d\hat{\xi}} + (\gamma - 1 + i\hat{\Omega})P + \sigma_r\left(\frac{\hat{\xi}}{\hat{\xi}_r}\right)^{-i\hat{\Omega}/2}. \tag{2.27}$$

The solution of (2.26) can be written as the sum of two homogeneous solutions and a particular solution,

$$P(\hat{\xi}) = \sigma_r P_p(\hat{\xi}) + a_0 P_{h1}(\hat{\xi}) + b_0 P_{h2}(\hat{\xi}), \tag{2.28}$$

where the solutions to the homogeneous equation (P_{h1} and P_{h2}) are calculated using the hypergeometric series around $(1-\hat{\xi})$ (Abramowitz and Stegun, 1964), as done by Moase et al. (2007),

$$P_{h1}(\hat{\xi}) = {}_2F_1(a, b; 1+a+b; (1-\hat{\xi})), \tag{2.29}$$

$$P_{h2}(\hat{\xi}) = (1-\hat{\xi})^{-a-b}\,{}_2F_1(-a, -b; 1-a-b; (1-\hat{\xi})). \tag{2.30}$$

The values of a and b are calculated through

$$a + b = 1 + \frac{2i\hat{\Omega}}{\gamma+1}, \quad \text{and} \quad ab = \frac{i\hat{\Omega}(2+i\hat{\Omega})}{2(\gamma+1)}, \tag{2.31}$$

and the hypergeometric functions ${}_2F_1$ are given by

$${}_2F_1(A, B; C; Z) = \sum_{n=0}^{\infty} \frac{A^{(n)}B^{(n)}}{C^{(n)}}\frac{Z^n}{n!}, \tag{2.32}$$

where $A^{(n)} = A(A+1)(A+2)...(A+n-1)$ is the rising factorial. The particular solution in series of $(1-\hat{\xi})$ was obtained by Moase et al. (2007). It reads

$$P_p(\hat{\xi}) = \frac{-i\Omega(\hat{\xi}_r)^{i\Omega/2}}{2(\gamma+1)}\sum_{n=0}^{\infty} c_n(1-\hat{\xi})^{n+1}, \tag{2.33}$$

where

$$c_0 = \frac{1}{1+a+b}. \tag{2.34}$$

$$c_n = \frac{c_{n-1}(n+a)(n+b)n! + (-1)^n(1-n-\frac{1}{2}\mathrm{i}\hat{\Omega})^{(n)}}{(n+1)(n+1+a+b)n!} \tag{2.35}$$

As shown by Moase et al. (2007), this solution converges for $0 < \hat{\xi} < 2$ because the series is performed around $(1-\hat{\xi})$, which gives a Mach number range from $M > 0$ to $M < \sqrt{4/(3-\gamma)}$[3]. For a subsonic flow, the boundary conditions are the downstream-propagating acoustic wave at the inlet, $w_f^+ = P(\hat{\xi}_{in}) + M_{in}U(\hat{\xi}_{in})$, and the upstream-propagating acoustic wave at the outlet, $w_f^- = P(\hat{\xi}_{out}) - M_{out}U(\hat{\xi}_{out})$. For choked nozzles, the second homogeneous solution behaves as $(1-\hat{\xi})^{-1-2\mathrm{i}\hat{\Omega}/(\gamma+1)}$ near $M = 1$. As P should be regular at this point, this solution should disappear if the throat is located inside the computational domain, giving $b_0 = 0$. The value of a_0 is obtained by imposing the downstream-propagating acoustic wave at the inlet. For subsonic flows, the boundary conditions should impose both the dowsntream-propagating acoustic wave at the inlet and the upstream-propagating acoustic wave at the outlet, which gives a set of two equations to obtain the two unknowns a_0 and b_0.

This method is, however, valid only for a particular nozzle geometry in which the mean velocity profile is linear. The method was extended first by Moase et al. (2007) and then by Giauque et al. (2012) to piecewise linear nozzles: the hypergeometric solution was used to compute the transfer functions of each linear segment of the nozzle, which where then combined to provide the complete transfer functions of the nozzle. Doing so, any nozzle geometry can be described with as many linear sections as necessary.

[3]Note that this limit is inherent of the present expansion of the solution around the pole $(1-\hat{\xi})$ used by Marble and Candel (1977). The series can also be expanded around other poles, $(\hat{\xi})$ or $(1/\hat{\xi})$, presenting different limits. The combination of the three expansions can provide the complete solution for any Mach number range.

2.4 Asymptotic expansion of the linearised Euler equations

The method described above, in Section 2.3, solves the propagation of waves for the case where the nozzle presents a linear mean velocity profile. When considering any other nozzle geometry, the compact solution gives the result for the limit of low frequencies. To improve the compact solution for larger frequencies, an asymptotic expansion of the linearised Euler equations (2.12) can be performed in terms of the dimensionless frequency $\Omega = fL_n/c_0$[4], where f is the frequency, L_n is the nozzle length and c_0 the inlet sound speed. To do so, the non-dimensional pressure fluctuation is written as $\varphi = \varphi^{(0)} + \Omega\varphi^{(1)}$, and similarly for the dimensionless velocity and entropy fluctuations. The zeroth-order term of the asymptotic expansion is, as expected, the compact solution, explained in Section 2.2. The first order correction of the equations is, however, a complicated system of equations as, in the general case, the zeroth-order solutions of pressure and velocity are a function of the x-coordinate, $\varphi^{(0)}(x)$ and $\nu^{(0)}(x)$. Stow et al. (2002) showed that, for the case of a choked nozzle, the zeroth-order solution of the dimensionless pressure and velocity are constant throughout the nozzle, as explained in Section 2.3. The asymptotic expansion can be performed analytically to correct the phase of the inlet reflection coefficient up to first-order in frequency,

$$\left[\frac{w_0^-}{w_0^+}\right] = \left[\frac{w_0^-}{w_0^+}\right]_{MC} \exp\left[-\mathrm{i}\left(k^+ + k^-\right)\bar{l}\Omega\right], \tag{2.36}$$

where the subscript $[\ ]_{MC}$ represents the transfer function obtained through the compact nozzle hypothesis (as seen in Table 2.2). For the reflection coefficient of a choked nozzle, it reads

$$\left[\frac{w_0^-}{w_0^+}\right]_{MC} = \frac{1 - \frac{1}{2}(\gamma-1)M_0}{1 + \frac{1}{2}(\gamma-1)M_0}. \tag{2.37}$$

In the above, $k^+ = 2\pi/(\bar{u}+\bar{c})$ and $k^- = 2\pi/(\bar{u}-\bar{c})$ (where $\bar{u}$ and $\bar{c}$ are reduced with the inlet speed c_0), and the dimensionless equivalent nozzle length, $\bar{l}$, is computed using the asymptotic expansion of the linearised Euler equations up to first order and considering a low Mach number at the inlet (for more

[4]The original article by Stow et al. (2002), where the method is first used, presents a different dimensionless frequency definition. Here the definition shown above will be used for coherence with the rest of the article.

details, see Stow et al. (2002)). It reads

$$\bar{l} = \frac{1}{L_n} \int_0^{x_*} \frac{u(0)}{u(x)} dx. \tag{2.38}$$

This correction is valid for choked nozzles and in the case of small inlet Mach numbers. As seen in (2.36), the correction affects the phase prediction only, leaving the modulus of the solution constant and equal to the compact prediction. It should be noted that the phase of the reflection coefficient is of great importance when solving combustion instability problems, as it controls the resonance frequency of the instability. However, variations of the modulus of the reflection coefficient cannot be neglected as they represent the energy lost through the boundaries.

The equivalent nozzle length method was extended by Goh and Morgans (2011a) to compute the phase of the transmission coefficients for the acoustic and the entropy waves. This method is based on the combination of several equivalent lengths through the convergent and the divergent sections to obtain the correct phase prediction of the transfer functions of the nozzle in a similar way as the reflection coefficient. In the case of choked nozzles with a shock wave, a dependency of the modulus of the transmission coefficient with frequency was also found (for more details, see Goh and Morgans (2011a)).

Chapter 3

The invariant method

As seen in Chapter 2, there are two possible ways to calculate the transmission and reflection coefficients of acoustic and entropy waves propagating through a nozzle: either a low-frequency assumption is made (Section 2.2), or an assumption is made on the nozzle geometry by assuming a linear mean velocity profile (Section 2.3). Leyko et al. (2009) and Duran et al. (2013c) showed that the transfer functions of a nozzle were strongly dependent on frequency. Bloy (1979) showed numerically that, while the compact solution depends only on the inlet and outlet Mach numbers, and not on the geometry of the nozzle, at non-compact frequencies the transfer functions depend strongly on its geometry. For this reason, it is interesting to obtain a general analytical solution in which the transfer functions can be calculated for any nozzle geometry.

In the present chapter, an analytical solution is derived for the linearised Euler equations of (2.12) for the general case. This is done first by performing a change of variable in the linearised Euler equations, writing them in terms of the dimensionless mass, total temperature and entropy fluctuations. These three variables are named invariants as they are constant throughout the nozzle for the zeroth-order solution (as seen in equation (2.16)). The resulting equation is the correction of the compact method for non-compact frequencies, and can be solved using the Magnus expansion (Blanes et al., 2009).

3.1 The invariant equation

To start, the linearised Euler equations of (2.12) are recast in a dimensionless form, using the dimensionless space and time variables, $\xi = x/L_n$ and $\tau = tf$, where L_n is the nozzle length and f is a characteristic frequency of the perturbation. The mean flow velocity is reduced using the sound speed at the inlet of the nozzle, c_0, giving the dimensionless form $\bar{u} = u/c_0$. The equations are rewritten using the reduced frequency (or Helmholtz number), $\Omega = fL_n/c_0$, which compares the nozzle length with a characteristic acoustic wavelength. In this form, the equations read

$$\left[\Omega\frac{\partial}{\partial\tau} + \bar{u}\frac{\partial}{\partial\xi}\right](\varphi) + \bar{u}\frac{\partial}{\partial\xi}(\nu) = 0, \tag{3.1a}$$

$$\left[\Omega\frac{\partial}{\partial\tau} + \bar{u}\frac{\partial}{\partial\xi}\right](\nu) + \frac{\bar{c}^2}{\bar{u}}\frac{\partial}{\partial\xi}(\varphi) + \Big(2\nu - (\gamma-1)\varphi - \sigma\Big)\frac{d\bar{u}}{d\xi} = 0, \tag{3.1b}$$

$$\left[\Omega\frac{\partial}{\partial\tau} + \bar{u}\frac{\partial}{\partial\xi}\right](\sigma) = 0. \tag{3.1c}$$

Equations (3.1) are first written as a function of the mass, total temperature and entropy fluctuations,

$$I_A \equiv \left(\frac{\dot{m}'}{\dot{m}}\right) = \varphi + \nu - \sigma, \tag{3.2a}$$

$$I_A \equiv \left(\frac{T_t'}{T_t}\right) = (\gamma-1)\frac{M^2\nu + \varphi + \dfrac{\sigma}{\gamma-1}}{1 + \dfrac{\gamma-1}{2}M^2}, \tag{3.2b}$$

$$I_A \equiv \left(\frac{s'}{c_p}\right) = \sigma. \tag{3.2c}$$

These are the flow invariants, which are constant throughout the nozzle when considering the compact assumption. To do so, the velocity gradient on the right hand side of (3.1b) is first written as a function of the Mach number gradient,

$$\frac{d\bar{u}}{d\xi} = \frac{d}{d\xi}\Big(M\bar{c}\Big) = M\frac{d\bar{c}}{d\xi} + \bar{c}\frac{dM}{d\xi} = \left(\frac{\bar{c}}{1 + \frac{\gamma-1}{2}M^2}\right)\frac{dM}{d\xi}. \tag{3.3}$$

This result is introduced in (3.1b) and then multiplied by M^2. Rearranging terms, it gives

$$\Omega M^2\frac{\partial}{\partial\tau}(\nu) + \bar{u}\frac{\partial}{\partial\xi}\left(M^2\nu + \varphi\right) - \bar{u}\left(\frac{(\gamma-1)M}{1 + \frac{\gamma-1}{2}M^2}\right)\Big(M^2\nu + \varphi + \frac{\sigma}{(\gamma-1)}\Big)\frac{dM}{d\xi} = 0. \tag{3.4}$$

Combining the spatial derivative terms and using (3.1c), the linearised Euler equations (3.1) can be recast as

$$\Omega\frac{\partial}{\partial\tau}(\varphi-\sigma)+\bar{u}\frac{\partial}{\partial\xi}(\varphi+\nu-\sigma)=0, \quad (3.5a)$$

$$\Omega\frac{\partial}{\partial\tau}\left(M^2\nu+\frac{\sigma}{(\gamma-1)}\right)+\bar{u}(1+\frac{\gamma-1}{2}M^2)\frac{\partial}{\partial\xi}\left(\frac{M^2\nu+\varphi+\frac{\sigma}{(\gamma-1)}}{1+\frac{\gamma-1}{2}M^2}\right)=0, \quad (3.5b)$$

$$\left[\Omega\frac{\partial}{\partial\tau}+\bar{u}\frac{\partial}{\partial\xi}\right](\sigma)=0, \quad (3.5c)$$

where no further assumption has been made. Using (3.2) within the limit of small frequencies ($\Omega\to 0$), the temporal derivatives can be dropped and the compact equations (2.16) are recovered.

To analyse the effects of non-zero frequencies, the equations are written as a function of the invariants I_A, I_B and I_C, introduced in (3.2). These flow invariants are constant through the nozzle at first order for any flow configuration. After some algebra, and writing the substantial derivative as $D/D\tau=\Omega\partial/\partial\tau+\bar{u}\partial/\partial\xi$, the equations read

$$\frac{D}{D\tau}(I_A)=\frac{\bar{u}}{(\gamma-1)M^2}\left[\frac{\partial}{\partial\xi}(I_C)-\left(1+\frac{\gamma-1}{2}M^2\right)\frac{\partial}{\partial\xi}(I_B)\right], \quad (3.6a)$$

$$\frac{D}{D\tau}(I_B)=-\frac{(\gamma-1)\bar{u}}{1+\frac{\gamma-1}{2}M^2}\left[\frac{\partial}{\partial\xi}(I_A)+\frac{\partial}{\partial\xi}(I_C)\right], \quad (3.6b)$$

$$\frac{D}{D\tau}(I_C)=0. \quad (3.6c)$$

If the invariants are assumed harmonic, a time Fourier transform (with the $e^{2\pi i\Omega\tau}$ convention) leads to

$$[\mathcal{E}(\xi)]\frac{d}{d\xi}[\mathbf{I}]=2\pi i\Omega\mathbf{I}, \quad (3.7)$$

where $\mathbf{I}$ is the vector of invariants, containing I_A, I_B and I_C, and $\mathcal{E}(\xi)$ is a non-constant 3×3 matrix,

$$\mathcal{E}(\xi)=-\bar{u}\begin{bmatrix}1 & \frac{1+\frac{\gamma-1}{2}M^2}{(\gamma-1)M^2} & -\frac{1}{(\gamma-1)M^2}\\ \frac{\gamma-1}{1+\frac{\gamma-1}{2}M^2} & 1 & \frac{\gamma-1}{1+\frac{\gamma-1}{2}M^2}\\ 0 & 0 & 1\end{bmatrix}, \quad (3.8)$$

where the Mach number, M, and the dimensionless speed, $\bar{u}$, are functions of the spatial coordinate, ξ. When the determinant of $\mathcal{E}$ is non-zero ($M \neq 1$), (3.7) can be inverted, leading to

$$\frac{d}{d\xi}[\mathbf{I}] = \mathcal{A}(\xi)\mathbf{I}. \tag{3.9}$$

Matrix $\mathcal{A}$ is a non-constant complex matrix of order $O(\Omega)$,

$$\mathcal{A}(\xi) = \frac{-2\pi i\Omega}{\bar{u}(M^2-1)} \begin{bmatrix} M^2 & -\dfrac{1+\frac{\gamma-1}{2}M^2}{\gamma-1} & \dfrac{\gamma}{\gamma-1} \\ \dfrac{-(\gamma-1)M^2}{1+\frac{\gamma-1}{2}M^2} & M^2 & -\dfrac{(\gamma-1)M^2+1}{1+\frac{\gamma-1}{2}M^2} \\ 0 & 0 & M^2-1 \end{bmatrix}, \tag{3.10}$$

which represents the correction to the compact assumption and where M and $\bar{u}$ are functions of ξ. For choked nozzles $M = 1$ at the throat, the determinant of $\mathcal{E}$ is zero and the matrix system cannot be inverted. This case will be treated separately in Section 3.3.2.

3.2 The Magnus expansion

Stow et al. (2002) and Goh and Morgans (2011a) performed an asymptotic expansion in terms of variables φ, ν and ρ'/ρ using the fact that the zero-order terms are constant through the nozzle for choked flows. Writing the equation for the first order correction in the choked case, they found a method to correct the phase of the reflection coefficient through an equivalent nozzle length. In our case, the asymptotic expansion can be performed in terms of the invariants (for which the zeroth-order term is constant throughout the nozzle for any flow configuration): equation (3.9) can be used to obtain an expression for the nth order term of the asymptotic expansion of $\mathbf{I}$. Considering $\mathbf{I}(\xi) = \mathbf{I}^{(0)} + \Omega\mathbf{I}^{(1)}(\xi) + \cdots + \Omega^n\mathbf{I}^{(n)}(\xi)$, the nth order equation reads

$$\frac{d}{d\xi}\left[\mathbf{I}^{(n)}\right] = \hat{\mathcal{A}}(\xi)\mathbf{I}^{(n-1)} \qquad \text{for} \qquad n > 0, \tag{3.11}$$

where $\hat{\mathcal{A}} = \mathcal{A}/\Omega$ is independent of Ω because $\mathcal{A}$ is a linear form of Ω, as seen in (3.10). This is a similar expression to the one obtained by Stow et al.

(2002), but written in terms of $\mathbf{I}$ instead of φ, ν and ρ'/ρ and generalised up to any order and for any flow configuration. As $\mathbf{I}^{(0)}$ is constant through the nozzle, the first term of the asymptotic expansion can be easily obtained through direct integration of $\hat{\mathcal{A}}(\xi)\mathbf{I}^{(0)}$, element by element. This extends the first order solution of Stow et al. (2002) for any flow condition. Yet, the complexity of this method increases for higher order terms as $\mathbf{I}^{(n)}$ is in general a function of ξ.

A simpler and more general method is proposed here to solve (3.9), based on the Magnus expansion (Magnus, 1954; Blanes et al., 2009). In this method, the solution of (3.9) is written as

$$\mathbf{I}(\xi) = [\mathcal{C}(\xi)]\,\mathbf{I}_0, \qquad \text{with} \qquad \mathcal{C}(\xi) = \exp\left(\mathcal{B}(\xi)\right), \tag{3.12}$$

where $\mathbf{I}_0$ is the value of the invariant vector at the inlet. The asymptotic expansion is performed in terms of $\mathcal{B}$ instead of expanding $\mathbf{I}$ directly. If matrix $\mathcal{A}(\xi)$ satisfied $\mathcal{A}(\xi_1)\mathcal{A}(\xi_2) - \mathcal{A}(\xi_2)\mathcal{A}(\xi_1) = 0$ for any ξ_1 and ξ_2 pair of values (this is the case, for example, if the Mach number is constant), then matrix $\mathcal{B}(\xi)$ could be calculated exactly by integrating $\mathcal{A}(\xi)$ term by term,

$$\mathcal{B}(\xi) = \int_0^\xi d\xi_1 \mathcal{A}(\xi_1). \tag{3.13}$$

In a more general case, matrix $\mathcal{B}(\xi)$ is obtained using the Magnus expansion,

$$\mathcal{B}(\xi) = \sum_{k=1}^{\infty} \mathcal{B}^{(k)}(\xi). \tag{3.14}$$

The first three terms are given by

$$\mathcal{B}^{(1)}(\xi) = \int_0^\xi d\xi_1 \mathcal{A}(\xi_1), \tag{3.15}$$

$$\mathcal{B}^{(2)}(\xi) = \frac{1}{2}\int_0^\xi d\xi_1 \int_0^{\xi_1} d\xi_2 [\mathcal{A}(\xi_1), \mathcal{A}(\xi_2)], \tag{3.16}$$

$$\mathcal{B}^{(3)}(\xi) = \frac{1}{6}\int_0^\xi d\xi_1 \int_0^{\xi_1} d\xi_2 \int_0^{\xi_2} d\xi_3 [\mathcal{A}(\xi_1), [\mathcal{A}(\xi_2), \mathcal{A}(\xi_3)]] + [\mathcal{A}(\xi_3), [\mathcal{A}(\xi_2), \mathcal{A}(\xi_1)]], \tag{3.17}$$

where $[\mathcal{A}_1, \mathcal{A}_2] = \mathcal{A}_1\mathcal{A}_2 - \mathcal{A}_2\mathcal{A}_1$ is the matrix commutator. The first term coincides exactly with the solution given in (3.13) for the case when

$[\mathcal{A}(\xi_1), \mathcal{A}(\xi_2)] = 0$, and the remaining terms are corrections of higher order. As $\mathcal{A}(\xi)$ is of order $O(\Omega)$, the Magnus expansion verifies that the kth term of the expansion is of order $O(\Omega^k)$. This does not mean that each kth term of the Magnus expansion will only contribute to the kth term of the asymptotic expansion in $\mathbf{I}$, since the exponential of matrix $\mathcal{B}$ should be performed as seen in (3.12).

The terms of the Magnus expansion can be calculated with a recursive procedure reducing computational costs. Defining the matrix $\mathcal{S}_n^{(k)}$ recursively,

$$\begin{cases} \mathcal{S}_n^{(j)} = \sum_{m=1}^{n-j} \left[\mathcal{B}^{(m)}, \mathcal{S}_{n-m}^{(j-1)}\right] & 2 \le j \le n-1 \\ \mathcal{S}_n^{(1)} = \left[\mathcal{B}^{(n-1)}, \mathcal{A}\right] \qquad \mathcal{S}_n^{(n-1)} = ad_{\mathcal{B}^{(1)}}^{(n-1)}(\mathcal{A}) \end{cases}, \tag{3.18}$$

where $ad_{\mathcal{B}}^{(k)}(\mathcal{A})$ is an iterated commutator given by

$$ad_{\mathcal{B}}^{(0)}(\mathcal{A}) = \mathcal{A} \qquad ad_{\mathcal{B}}^{(k+1)}(\mathcal{A}) = \left[\mathcal{B}, ad_{\mathcal{B}}^{(k)}(\mathcal{A})\right], \tag{3.19}$$

and $\mathcal{B}^{(k)}$ is finally obtained as

$$\begin{aligned} \mathcal{B}^{(1)}(\xi) &= \int_0^{\xi} d\xi_1 \mathcal{A}(\xi_1), \\ \mathcal{B}^{(n)}(\xi) &= \sum_{j=1}^{n-1} \frac{b_j}{j!} \int_0^{\xi} \mathcal{S}_n^{(j)}(\xi_1) d\xi_1 \end{aligned}, \tag{3.20}$$

where b_j are the Bernoulli numbers ($b_1 = \frac{-1}{2}$, $b_2 = \frac{1}{6}$, $b_3 = 0$, $b_4 = \frac{-1}{30}$, $b_5 = 0$ ...). The Magnus expansion has been widely used to solve linear systems of differential equations with varying coefficients such as (3.12), for example in Wilcox (1967), (Sakurai and Tuan, 1985) and Madhu and Kurur (2006).

To obtain the final solution, the value of $\mathcal{B}(\xi)$ has to be computed analytically (if possible) or numerically, and its exponential calculated to give $\mathcal{C}$. This can be done using different methods, as shown in Moler (2003). The method used hereafter performs a Taylor series of the exponential, namely,

$$\mathcal{C} = \exp(\mathcal{B}) = \mathcal{I} + (\mathcal{B}) + \frac{1}{2!}(\mathcal{B})^2 + \cdots + \frac{1}{n!}(\mathcal{B})^n. \tag{3.21}$$

Other methods can be used to calculate the matrix exponential with higher accuracy and reducing computational cost. The advantage of the Taylor series used here is that, if the Magnus expansion is truncated at the

kth order, the Taylor expansion can also be truncated at the same order (as higher order terms are meaningless), reducing the complexity of the solution. This method can be used to calculate $\mathcal{C}(\xi)$ in any section. In particular at the inlet $\mathcal{B}(0) = \mathcal{O}$, and therefore $\mathcal{C}(0) = \mathcal{I}$, the identity matrix.

As each term of the Magnus expansion $\mathcal{B}^{(k)}$ is of order $O(\Omega^k)$, it is possible to calculate a frequency-independent expression of the Magnus expansion using matrix $\hat{\mathcal{A}}$, where the term in Ω has been dropped. This expansion, denoted $\hat{\mathcal{B}}^{(k)}$, is used to obtain a general form with no frequency dependence. When solving for each frequency, the expansion of $\mathcal{B}$ can be calculated as $\mathcal{B} = \sum \Omega^k \hat{\mathcal{B}}^{(k)}$.

The series of (3.14) is an expansion of the solution for $\mathbf{I}(\xi)$ around $\xi = 0$. The series converges fast when the condition given by

$$\int_0^{\xi_F} ||\mathcal{A}(\xi)||_2 d\xi < \pi \tag{3.22}$$

is satisfied (see Blanes et al. (2009); Casas (2007); Moan and Niesen (2006) for more details), but may diverge for larger values of the integral. In the above, $||\cdot||_2$ is the 2-norm of the matrix, which for a square matrix is equal to the spectral norm (the largest singular value of the matrix), and can be calculated as

$$||\mathcal{A}||_2 = \sqrt{\lambda_{max}(\mathcal{A}^*\mathcal{A})}, \tag{3.23}$$

where $\mathcal{A}^*$ is the complex conjugate of $\mathcal{A}$ and $\lambda_{max}(\quad)$ is the largest eigenvalue of the matrix.

As boundary conditions should be imposed both at the inlet and at the outlet (see Section 3.3), the expansion should be valid until the outlet, $\xi_F = 1$. Integrating (3.22) gives a critical frequency value, Ω_{crit}, from which the method may diverge. Below this value, the series converges fast and a few terms are enough to compute an approximate solution.

3.2.1 Solution for larger frequencies

An analytical solution of the linearised Euler equations has been obtained for frequencies up to Ω_{crit}. This method can be extended to compute the solution up to any frequency as shown in Blanes et al. (2009). Given a certain Ω_{max} value, (3.22) gives the maximal value of $\xi = \xi_1$, for which the

solution given by (3.12) converges. In the general case, $\xi_1 < 1$. In that case, the remaining part of the the solution $\mathbf{I}(\xi)$ may be calculated by expanding it using the Magnus series around ξ_1, which, for the given value of Ω_{max}, converges until ξ_2. Proceeding with this method, each Magnus expansion of each nozzle division allows us to write

$$\mathbf{I}(\xi_n) = \exp\left(\mathcal{B}\left(\xi_n, \xi_{n-1}\right)\right)\mathbf{I}(\xi_{n-1}). \tag{3.24}$$

Combining the solutions from the inlet to the outlet,

$$\mathbf{I}(\xi_N) = \prod_{n=1}^{N} \exp\left(\mathcal{B}\left(\xi_n, \xi_{n-1}\right)\right)\mathbf{I}_0, \tag{3.25}$$

where $\mathcal{B}\left(\xi_n, \xi_{n-1}\right)$ is the Magnus expansion that relates $\mathbf{I}(\xi_n)$ with $\mathbf{I}(\xi_{n-1})$ through the matrix exponential and N is the number of divisions of the nozzle.

3.3 Boundary conditions

Once (3.9) is solved, the equations relating the acoustic and entropy perturbations at any point of the nozzle with the perturbations at the inlet are written as $\mathbf{I}(\xi) = \mathcal{C}(\xi)\mathbf{I}_0$. If the compact solution is considered, matrix $\mathcal{C}$ is obtained through (2.16) and is found to be the identity matrix. When considering the general solution in the non-zero-frequency case, $\mathcal{C}$ is frequency-dependent and is calculated using the procedure shown in Section 3.2. In both cases, the boundary conditions should provide three equations at the inlet or at the outlet to calculate $\mathbf{I}_0$. This should be done imposing only the incoming information. For this reason, vector $\mathbf{I}$ should be decomposed into propagating waves.

To do so, we place ourselves at a region where locally the section is considered constant, at the inlet or at the outlet. Vector $\mathbf{I}$ is written as $\mathbf{I} = \hat{\mathbf{I}}\exp(-\mathrm{i}\int_0^\xi \kappa(\varsigma)d\varsigma)$, with $\hat{\mathbf{I}}$ constant, and introduced in (3.9) to obtain an eigenvalue problem for κ. The solution of this problem leads to

$$\kappa^+ = \frac{2\pi\Omega}{\bar{u}+\bar{c}}, \qquad \kappa^- = \frac{2\pi\Omega}{\bar{u}-\bar{c}} \qquad \text{and} \qquad \kappa^s = \frac{2\pi\Omega}{\bar{u}}, \tag{3.26}$$

which are the wavenumbers of the downstream and upstream acoustic waves and of the entropy wave, propagating at dimensionless speeds $\bar{u}+\bar{c}$, $\bar{u}-\bar{c}$

and $\bar{u}$, respectively. The associated eigenvectors are obtained and written in a matrix form as

$$\hat{\mathbf{I}} = \mathcal{D}\mathbf{W} = \begin{bmatrix} \eta^+ & \eta^- & -1 \\ \beta^+ & \beta^- & \zeta \\ 0 & 0 & 1 \end{bmatrix} \begin{pmatrix} w^+ \\ w^- \\ w^s \end{pmatrix}, \tag{3.27}$$

where w^+, w^- and w^s are the acoustic and entropy waves as obtained in Section 2.1.2 , and

$$\eta^{\pm} = \frac{1}{2}\left(1 \pm \frac{1}{M}\right), \quad \beta^{\pm} = \frac{(\gamma-1)\zeta}{2}(1 \pm M) \quad \text{and} \quad \zeta = \left(1 + \frac{\gamma-1}{2}M^2\right)^{-1}, \tag{3.28}$$

are used for simplicity. Inverting the system (3.27) and rewriting $\hat{\mathbf{I}}$ using (3.2), the waves can be written as a function of the primitive variables to yield (2.19). Each one of the waves w^+, w^- and w^s corresponds to a wavenumber, respectively κ^+, κ^- and κ^s, and therefore to a propagating speed, respectively $\bar{u} + \bar{c}$, $\bar{u} - \bar{c}$ and $\bar{u}$. As only incoming waves can be imposed, a difference should be made between the subsonic and the choked flow.

Note that using matrix notation, it is straightforward to combine expressions (3.7) and (3.27) to obtain an expression of the LEE in terms of the acoustic and entropy waves,

$$\frac{\partial \mathbf{W}}{\partial t} + \mathcal{L}\mathbf{W} = \mathcal{D}^{-1}\mathcal{E}\frac{d\mathcal{D}}{d\xi}, \quad \text{with} \quad \mathcal{L} = \begin{bmatrix} \bar{u}+\bar{c} & 0 & 0 \\ 0 & \bar{u}-\bar{c} & 0 \\ 0 & 0 & \bar{u} \end{bmatrix}. \tag{3.29}$$

This formulation is not used here due to the complexity of the RHS term, but illustrates the coupling of acoustic and entropy waves when a mean flow gradient exists, as explained in Section 2.1.2. Equation (3.29) is equivalent to (2.15), but written in matrix form.

3.3.1 Subsonic flow

The propagation speeds of each wave define which ones can be imposed at the boundary condition. For a subsonic flow, the downstream-propagating

acoustic wave and the entropy wave are imposed at the inlet (noted with the subscript $_0$), while the upstream-propagating acoustic wave is imposed at the outlet (noted with $_1$), as seen in figure 2.3. This gives the three conditions that can be imposed to solve for $\mathbf{I}_0$. The incoming acoustic waves can be imposed by setting their values either directly, or indirectly through a reflection coefficient, relating it to the outgoing waves. For instance, the downstream-propagating acoustic wave at the inlet can be written as $w_0^+ = w_{0,f}^+ + R_0 w_0^-$, where $w_{0,f}^+$ is a known forcing term at the inlet and R_0 is the acoustic reflection coefficient at the inlet. For the upstream-propagating acoustic wave at the outlet, the expression reads $w_1^- = w_{1,f}^- + R_1 w_1^+ + R_s w_1^s$, where $w_{1,f}^-$ is a known forcing term at the outlet, R_1 is the acoustic reflection coefficient at the outlet and R_s is an extra term that accounts for the generation of upstream-propagating acoustic waves by the entropy waves, which will be used in Section 3.3.2. Similarly, the entropy wave can be written as $w_0^s = w_{0,f}^s + R_s' w_0^-$, where R_s' is the entropy wave generated by an upstream-propagating acoustic wave and will be used in Section 3.3.3. Equation (3.27) is applied at the inlet and at the outlet of the nozzle, where boundary conditions are imposed. Knowing that $\mathbf{I}_1 = \mathcal{C}_1 \mathbf{I}_0$ and using (3.27) for both the inlet and the outlet, the equations for the waves can be written as

$$\mathcal{D}_1 \begin{bmatrix} w^+ \\ w_f^- \\ w^s \end{bmatrix}_1 = \mathcal{C}_1 \mathcal{D}_0 \begin{bmatrix} w_f^+ \\ w^- \\ w_f^s \end{bmatrix}_0, \tag{3.30}$$

where matrices $\mathcal{D}_0$ and $\mathcal{D}_1$ are obtained from (3.27) by introducing the additional reflection coefficients,

$$\mathcal{D}_0 = \begin{bmatrix} \eta_0^+ & \eta_0^- + R_0 \eta_0^+ - R_s' & -1 \\ \beta_0^+ & \beta_0^- + R_0 \beta_0^+ + \zeta_0 R_s' & \zeta_0 \\ 0 & R_s' & 1 \end{bmatrix}, \tag{3.31}$$

$$\mathcal{D}_1 = \begin{bmatrix} \eta_1^+ + R_1 \eta_1^- & \eta_1^- & -1 + R_s \eta_1^- \\ \beta_1^+ + R_1 \beta_1^- & \beta_1^- & \zeta_1 + R_s \beta_1^- \\ 0 & 0 & 1 \end{bmatrix}. \tag{3.32}$$

Waves with subscript $_f$ are known (forced at the inlet or at the outlet), and the rest are unknown. There exist several methods to solve this system of equations. Here, a modification of the method proposed by Cumpsty and Marble (1977) to solve the propagation of acoustic and entropy waves through a two-dimensional compact stator vane, is adapted to the one-dimensional non-compact nozzle. The matrix system of equation (3.30) can be rearranged to have the unknowns on one side of the equation and the forcing values of the waves on the other side. This is done by exchanging the second column of matrices $\mathcal{D}_1$ and $\mathcal{C}_1\mathcal{D}_0$ and changing the sign of each term. This operation leads to an equation $\mathcal{D}_{out}\mathbf{W}_{out} = \mathcal{D}_{in}\mathbf{W}_{in}$, where the vector $\mathbf{W}_{in}$ is composed of the forcing waves $w^+_{0,f}$, $w^-_{1,f}$ and $w^s_{0,f}$ and $\mathbf{W}_{out}$ contains the unknown waves w^+_1, w^-_0 and w^s_1. The system can be inverted and solved. If needed, vector $\mathbf{I}_0$ can then be calculated using (3.27) at the inlet. As matrix $\mathcal{C}$, and in some cases the reflection coefficients and the forcing waves, are frequency-dependent, the system should be solved individually for each frequency.

3.3.2 Choked flow

For choked flows, (3.7) cannot be inverted, as the matrix is singular at the throat, where $M = 1$. As (3.7) was obtained through linear combination of (3.1), it can be concluded that these equations present a singularity at the throat of a choked nozzle, as shown by Marble and Candel (1977) for the case of a nozzle with a linear velocity profile. This singularity is linked to the upstream-propagating acoustic wave, which changes the propagating direction at the throat. The boundary condition is no longer imposed at the nozzle outlet (as w^- propagates downstream) but at the nozzle throat, where the wave changes sign. The condition that should be imposed is that of $M'/M = 0$ at the throat. This condition is equivalent to the one obtained by Stow et al. (2002), considering that the solution is regular at the nozzle throat. This condition imposes that, in the choked throat, no fluctuations of the Mach number can be present, as the throat is the region with the minimal section. The condition $M'/M = 0$ can be shifted to the nozzle inlet when considering the compact hypothesis, as done by Marble and Candel (1977), but this cannot be done in the non-compact case, as the boundary condition should be applied at the nozzle throat. It can be shown that for the compact case this condition is the same as the one imposed by Marble and Candel (1977), as explained in Section 2.2.

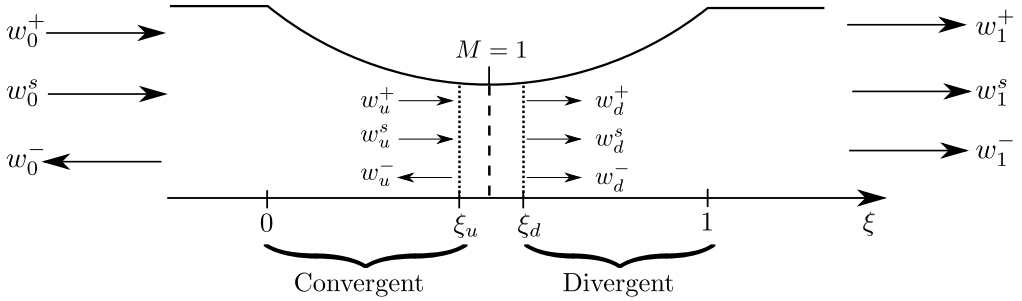

Figure 3.1 – *Sketch of the acoustic and entropy waves in a converging-diverging choked nozzle.*

To solve a converging-diverging nozzle with a choked flow, the two sections on both sides of the discontinuity will be calculated separately and matched together, as illustrated in figure 3.1. Firstly, the convergent subsonic region of the flow is calculated, as in Section 3.3.1, imposing two waves at the inlet (w_0^+ and w_0^s) and calculating the upstream-propagating acoustic wave at the outlet (w_u^-), using the condition $M'/M = 0$. Secondly, the supersonic part of the nozzle is calculated, imposing three waves at the inlet, obtained from the solution of the subsonic part and the analysis of the throat region.

To correctly impose the boundary conditions at the outlet of the subsonic half (w_u^-), and to calculate the three waves at the inlet of the supersonic region, the flow through the nozzle throat must be first analysed. A small slab with infinitesimally wide section through the throat is considered, as done by Moase et al. (2007) (as shown in figure 3.1), in which the Mach numbers at the inlet and outlet are $M_u = 1 - \epsilon$ and $M_d = 1 + \epsilon$, respectively, where subscripts u and d denote the quantities taken upstream and downstream of the compact nozzle throat region and $\epsilon \ll 1$. The boundary condition $M'/M = 0$ of (2.20) is applied at the nozzle throat, which is compact in the throat region. It can be shown (Marble and Candel, 1977; Stow et al., 2002) that, for this compact region, this condition applies at any section of the infinitesimally short nozzle (as seen in Section 2.2). Writing (2.20) at the outlet of the upstream subsonic half-section as a function of the three waves at the inlet (using (2.19)), and taking the limit $\epsilon \to 0$, the unknown reflected wave w_u^- can be calculated as a function of the two incoming waves,

$$w_u^- = R_u w_u^+ + R_s w_u^s, \tag{3.33}$$

with

$$R_u = \frac{3-\gamma}{\gamma+1} \qquad \text{and} \qquad R_s = \frac{-2}{\gamma+1}. \tag{3.34}$$

These reflection coefficients, R_u and R_s, must be imposed at the nozzle throat, allowing for the subsonic part of the nozzle to be solved as in Section 3.3.1.

For the supersonic half, the three waves should be imposed at the inlet using the relation $\mathbf{I}_u = \mathbf{I}_d$ for the compact region. The invariants at the outlet of the nozzle are calculated using the Magnus expansion in the supersonic section, and knowing that $\mathbf{I}_1 = \mathcal{C}^{(d)}\mathbf{I}_d$, where $\mathcal{C}^{(d)}$ is calculated only in the diverging part of the nozzle. Inverting (3.27), the waves at the outlet of the diverging section are calculated.

3.3.3 Supersonic flow with a shock wave

The transfer functions of a supersonic nozzle with a shock wave can be calculated by dividing the nozzle into two regions: the upstream region from the shock, which is computed as in Section 3.3.2, and the downstream region, calculated with the subsonic solution shown in Section 3.3.1. The shock wave acts as an interface between the two regions. The response of the shock wave to acoustic and entropy perturbations has been studied in depth (Marble and Candel, 1977; Kuo and Dowling, 1996; Stow et al., 2002; Moase et al., 2007; Goh and Morgans, 2011a; Leyko et al., 2011). The main steps of the method are summarised here. The reader is referred to Moase et al. (2007) and Goh and Morgans (2011a) for more details.

To begin with, the usual Rankine-Hugoniot shock relations are written below for the outlet Mach number, pressure, density and velocity as a func-

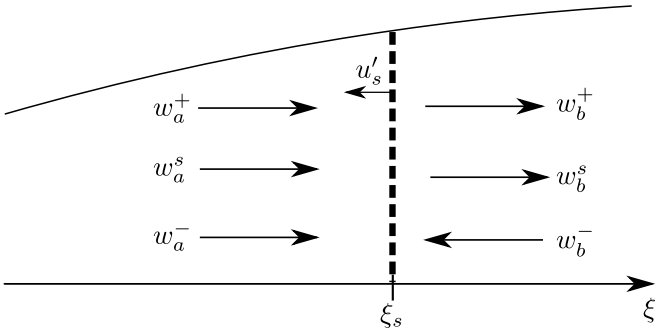

Figure 3.2 – *Sketch of a shock wave in a diverging section. u'_s is the movement of the shock wave due to the incoming perturbations.*

tion of the inlet Mach number, as in Stow et al. (2002),

$$M_b^2 = \frac{1 + \dfrac{\gamma-1}{2} M_a^2}{\gamma M_a^2 - \dfrac{\gamma-1}{2}}, \tag{3.35a}$$

$$\frac{p_b}{p_a} = \frac{2\gamma M_a^2 - (\gamma-1)}{\gamma+1} \tag{3.35b}$$

$$\frac{\rho_b}{\rho_a} = \frac{u_a}{u_b} = \frac{\dfrac{\gamma+1}{2} M_a^2}{1 + \dfrac{\gamma-1}{2} M_a^2}, \tag{3.35c}$$

where the subscripts $(\quad)_a$ and $(\quad)_b$ represent quantities taken upstream and downstream of the shock wave, as shown in figure 3.2. The shock is considered to oscillate about a mean position, ξ_s, with an amplitude, ξ'_s, due to the acoustic and entropy perturbations. These oscillations are assumed to be infinitesimally small. This can be ensured if $dA/d\xi > 0$ and is continuous at the shock location. The first order perturbations of the pressure, density and velocity equations through the shock wave in its reference frame give

$$\begin{aligned}
\frac{p'_{b,sh}}{\gamma p_b} - \frac{p'_{a,sh}}{\gamma p_a} &= \frac{4M_a^2}{(\gamma+1)} \left(\frac{p_a}{p_b}\right) \left(\frac{M'_{a,sh}}{M_a}\right), \\
\frac{\rho'_{b,sh}}{\rho_b} - \frac{\rho'_{a,sh}}{\rho_a} &= \frac{4}{M_a^2(\gamma+1)} \left(\frac{u_a}{u_b}\right) \left(\frac{M'_{a,sh}}{M_a}\right), \\
\frac{u'_{b,sh}}{u_b} - \frac{u'_{a,sh}}{u_a} &= \frac{-4}{M_a^2(\gamma+1)} \left(\frac{u_a}{u_b}\right) \left(\frac{M'_{a,sh}}{M_a}\right).
\end{aligned} \tag{3.36}$$

The subscript $(\quad)_{sh}$ represents the fluctuations seen by the shock wave in its reference frame, which can be decomposed into two terms: the absolute

fluctuation in the fixed reference frame, and an extra term caused by the movement of the shock wave inside a nozzle with a mean pressure/density gradient. Up to first order, they read

$$\begin{aligned} \frac{p'_{a,sh}}{\gamma p_a} &= \frac{p'_a}{\gamma p_a} + \frac{\xi'_s}{\gamma p_a}\frac{dp_a}{d\xi}, \\ \frac{\rho'_{a,sh}}{\rho_a} &= \frac{\rho'_a}{\rho'_a} + \frac{\xi'_s}{\rho_a}\frac{d\rho_a}{d\xi}, \end{aligned} \tag{3.37}$$

and similarly downstream of the shock wave. Note that the second term should be included to account for the displacement of the shock wave inside a nozzle with a mean flow gradient. The velocity and Mach number fluctuations seen by the shock wave are written as

$$\frac{u'_{a,sh}}{u_a} = \frac{u'_a}{u_a} + \frac{\xi'_s}{u_a}\frac{du_a}{d\xi} - \frac{1}{\bar{u}_a}\frac{d\xi'_s}{d\tau} = \frac{u'_a}{u_a} + \frac{\xi'_s}{u_a}\frac{du_a}{d\xi} - \frac{2\pi i\Omega}{M_a\bar{c}_a}\xi'_s, \tag{3.38}$$

$$\frac{M'_{a,sh}}{M_a} = \frac{M'_a}{M_a} + \frac{\xi'_s}{M_a}\frac{dM_a}{d\xi} - \frac{1}{M_a\bar{c}_a}\frac{d\xi'_s}{d\tau} = \frac{M'_a}{M_a} + \frac{\xi'_s}{M_a}\frac{dM_a}{d\xi} - \frac{2\pi i\Omega}{M_a\bar{c}_a}\xi'_s, \tag{3.39}$$

where the last term is caused by the movement of the shock wave, and M'_a/M_a is given through (2.20) as a function of the pressure, velocity and entropy fluctuations.

To close the system of equations, the mean pressure and density gradients are written as a function of the mean Mach number gradient, using the isentropic relations upstream and downstream of the shock wave. They read

$$\frac{1}{\gamma p}\frac{dp}{d\xi} = \frac{1}{\rho}\frac{d\rho}{d\xi} = \frac{-M}{1+\frac{\gamma-1}{2}M^2}\frac{dM}{d\xi}. \tag{3.40}$$

A similar expression was given in (3.3) for the mean velocity gradient. Finally, using the mass conservation through the shock wave, the Mach number gradient downstream can be written as a function of the upstream one,

$$\frac{M_b^2-1}{M_b\left(1+\frac{\gamma-1}{2}M_b^2\right)}\frac{dM_b}{d\xi} = \frac{M_a^2-1}{M_a\left(1+\frac{\gamma-1}{2}M_a^2\right)}\frac{dM_a}{d\xi}. \tag{3.41}$$

Using (3.37) and (3.38) in (3.36), and writing the mean pressure, velocity and density gradients as functions of the Mach gradient upstream of the shock wave (using (3.40), (3.41) and (3.3)), the equations for the fluctuating

primitive variables upstream and downstream of the nozzle shock read

$$\begin{aligned}
\frac{p_b'}{\gamma p_b} - \frac{p_a'}{\gamma p_a} &= \frac{4M_a^2}{(\gamma+1)}\left(\frac{p_a}{p_b}\right)\left[\frac{M_a'}{M_a} + \Gamma_p \xi_s'\right], \\
\frac{\rho_b'}{\rho_b} - \frac{\rho_a'}{\rho_a} &= \frac{4}{M_a^2(\gamma+1)}\left(\frac{u_a}{u_b}\right)\left[\frac{M_a'}{M_a} + \Gamma_\rho \xi_s'\right], \\
\frac{u_b'}{u_b} - \frac{u_a'}{u_a} &= \frac{-4}{M_a^2(\gamma+1)}\left(\frac{u_a}{u_b}\right)\left[\frac{M_a'}{M_a} + \Gamma_u \xi_s'\right],
\end{aligned} \tag{3.42}$$

where for simplicity the functions Γ are defined as

$$\begin{aligned}
\Gamma_p &= \left[1 - \frac{M_b^2 - M_a^2}{2M_a^2 M_b^2\left(M_b^2-1\right)}\right]\frac{1}{M_a}\frac{dM_a}{d\xi} - \frac{2\pi \mathrm{i}\Omega}{M_a \bar{c}_a}, \\
\Gamma_\rho &= \frac{1}{2}\left[1 + \frac{M_a^2-1}{M_b^2-1}\right]\frac{1}{M_a}\frac{dM_a}{d\xi} - \frac{2\pi \mathrm{i}\Omega}{M_a \bar{c}_a}, \\
\Gamma_u &= \frac{1}{2}\left[1 + \frac{M_a^2-1}{M_b^2-1}\right]\frac{1}{M_a}\frac{dM_a}{d\xi} - \left(\frac{M_a^2+1}{2}\right)\frac{2\pi \mathrm{i}\Omega}{M_a \bar{c}_a}.
\end{aligned} \tag{3.43}$$

The three equations of (3.42) can be combined to obtain two jump conditions independent of ξ_s'. The upstream fluctuating Mach number can be written as a function of the primitive variables: using (2.20) and knowing that $\rho'/\rho = \varphi - \sigma$ and using (2.19), the two jump conditions can be written as a function of the upstream- and downstream-propagating acoustic waves and the entropy wave and solved to obtain the transfer functions of Table 3.1.

The downstream subsonic region of the nozzle shock is calculated using the method presented in Section 3.3.1. At the inlet, the acoustic and the entropy waves coming from the shock waves have to be imposed. Using Table 3.1 they read

$$w_b^+ = \underbrace{\left[\frac{w_b^+}{w_a^+}\right]w_a^+ + \left[\frac{w_b^+}{w_a^-}\right]w_a^- + \left[\frac{w_b^+}{w_a^s}\right]w_a^s}_{w_{b,f}^+} + \underbrace{\left[\frac{w_b^+}{w_b^-}\right]}_{R_{in}} w_b^-, \tag{3.44}$$

$$w_b^s = \underbrace{\left[\frac{w_b^s}{w_a^+}\right]w_a^+ + \left[\frac{w_b^s}{w_a^-}\right]w_a^- + \left[\frac{w_b^s}{w_a^s}\right]w_a^s}_{w_{b,f}^s} + \underbrace{\left[\frac{w_b^s}{w_b^-}\right]}_{R_s'} w_b^-. \tag{3.45}$$

The downstream-propagating acoustic wave is composed of a forcing wave, $w_{b,f}^+$, corresponding to the first three terms of (3.44), and a reflection coefficient at the inlet equal to the last term. Similarly, the entropy wave

	w_b^+	w_b^s
Response to $w_a^+ = 1$	$\frac{\alpha^+}{\psi^+}$	$\phi\left(\frac{\alpha^+}{\psi^+} - 1\right) - \Lambda\left(1 - \frac{\gamma-1}{2}M_a\right)$
Response to $w_a^- = 1$	$\frac{\alpha^-}{\psi^+}$	$\phi\left(\frac{\alpha^-}{\psi^+} - 1\right) + \Lambda\left(1 + \frac{\gamma-1}{2}M_a\right)$
Response to $w_a^s = 1$	$M_a^2 M_b^2 \frac{\delta}{\psi^+}$	$1 + M_a^2 M_b^2 \frac{\delta}{\psi^+} + M_a\Lambda$
Response to $w_b^- = 1$	$-\frac{\psi^-}{\psi^+}$	$\phi\left(1 - \frac{\psi^-}{\psi^+}\right)$

$$\Lambda = \frac{1 - \left(\frac{\Gamma_\rho}{\Gamma_p}\right)}{M_a\left(1 + \frac{\gamma-1}{2}M_a^2\right)} \qquad \delta = \frac{2\left(1 - \frac{\Gamma_u}{\Gamma_p}\right)}{\left(1 + \frac{\gamma-1}{2}M_a^2\right)}$$

$$\alpha^\pm = \left(\frac{\Gamma_u}{\Gamma_p}\right) \pm M_a M_b^2\left[1 - \delta\left(1 \mp \frac{\gamma-1}{2}M_a\right)\right]$$

$$\phi = \frac{1}{2}\left[1 - \frac{1}{M_a^2 M_b^2}\left(\frac{\Gamma_\rho}{\Gamma_p}\right)\right] \qquad \psi^\pm = \left(\frac{\Gamma_u}{\Gamma_p}\right) \pm M_a^2 M_b$$

Table 3.1 – *Acoustic and entropy transfer functions through a shock wave.*

imposed at the inlet is divided into a forcing term (the first three terms of (3.45)) and an entropy reflection coefficient, R'_s, corresponding to the last term. Using these forcing waves and reflection coefficients, the subsonic region downstream of the shock can be calculated as in Section 3.3.1.

Chapter 4

Nozzle transfer functions at non-compact frequencies

The method described in Chapter 3 is used here to obtain the transfer functions of several nozzle geometries at all frequencies. The asymptotic expansion is performed up to fifth order in Ω, and the nozzle divided into several sections as shown in (3.24), depending on each case. It was shown that, with the nozzle divisions satisfying (3.22), a fifth order expansion in Ω is enough for the series to converge, and higher order terms are negligible for all cases considered in the present study. The integrals in the Magnus expansion are calculated using Simpson's rule. In Section 4.1 the method is used to calculate a nozzle with a linear steady velocity profile, comparing the result with the analytical solution of Marble and Candel (1977) presented in Section 2.3. A more realistic nozzle geometry is also considered to evaluate the influence of the exact profile on the transfer functions at non-zero frequencies. In Section 4.2, the invariant method is compared with the phase correction of the reflection coefficient through an effective nozzle length proposed by Stow et al. (2002), explained in Section 2.4, and with the extension proposed by Goh and Morgans (2011a) when considering a choked flow through the nozzle. The analytical model is then compared with the experimental data of Bell et al. (1973) in Section 4.3. Section 4.4 focuses on the transfer functions of subsonic converging-diverging nozzles. Finally, a parametric study on indirect to direct combustion noise is performed in Section 4.5, to extend the results of Leyko et al. (2009) to non-zero frequencies and provide some insight on how this ratio may vary at the exit of the turbine stage with increasing frequency.

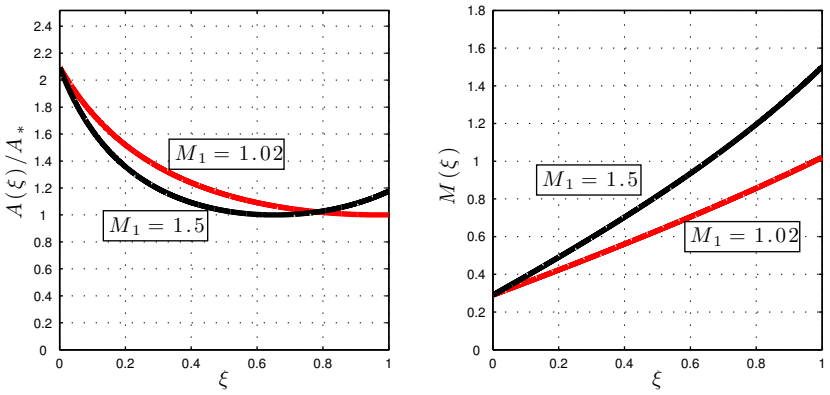

Figure 4.1 – *Section and Mach number of two linear steady velocity profile nozzles with inlet Mach number of* $M_0 = 0.29$ *and two different outlet Mach numbers.*

4.1 Comparison with a linear steady velocity choked nozzle

In this section, the invariant solution is compared with the analytical method proposed by Marble and Candel (1977) for a linear mean velocity profile nozzle, detailed in Section 2.3. This method is not general, and can be used only by assuming a specific nozzle geometry in which the steady velocity varies linearly with the axial coordinate (hereafter called the linear nozzle for simplicity). Two nozzles with a linear mean velocity profile are considered here, corresponding to an inlet Mach number of $M_0 = 0.29$ and two different outlet Mach numbers ($M_1 = 1.02$ and $M_1 = 1.5$). The nozzle Mach number profile is calculated using (2.23), as explained in Section 2.3, and the nozzle section is obtained using the steady quasi-one-dimensional Euler equations. It reads,

$$\frac{A}{A_*} = \frac{1}{M}\left[\left(\frac{2}{\gamma+1}\right)\left(1+\frac{\gamma-1}{2}M^2\right)\right]^{\frac{\gamma+1}{2(\gamma-1)}}, \tag{4.1}$$

where A_* is the critical section, and the Mach number is unity (equal in this case to the throat section, as the flow is choked). Figure 4.1 shows the nozzle section and the Mach number plotted as functions of the non-dimensional nozzle length, ξ, for both nozzles. The responses of the two nozzles to an entropy perturbation at the inlet are plotted in figure 4.2 as a function of the reduced frequency, Ω. The invariant method and the hypergeometric equations are used to solve both cases, showing that both methods give the same results when the same linear velocity profile is used, and tend

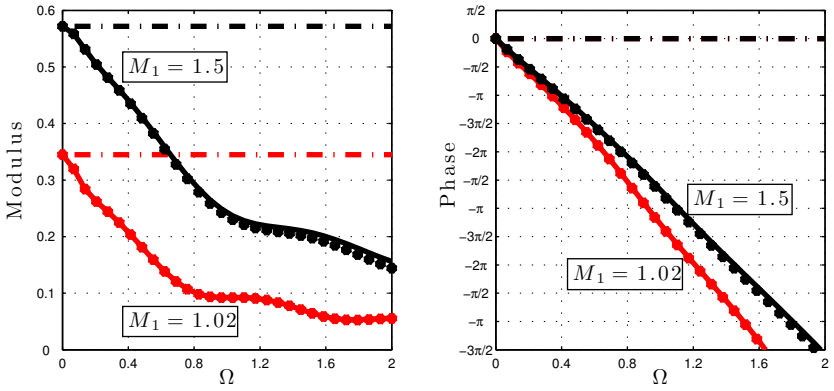

Figure 4.2 – *Amplitude and phase of the downstream-facing acoustic wave at the outlet, w_1^+, generated by an incoming entropy wave, $w_0^s = 1$, with $M_0 = 0.29$. ant method (——); hypergeometric equation (•) and compact solution (– · – · –).*

towards the compact solution for $\Omega = 0$. The indirect noise generated in this configuration decreases with increasing frequency, showing that the compact nozzle hypothesis is limited to low frequencies and that the modulus, and not only the phase, depends strongly on the frequency. Figure 4.3 shows the upstream-facing propagating acoustic wave at the outlet.

Both the invariant method and the hypergeometric equations can also be used to obtain the reflection coefficient of linear nozzles. In figure 4.4, the acoustic reflection coefficient of a choked nozzle with $M_0 = 0.29$ and $M_1 = 1.5$ is plotted for a unitary acoustic wave at the inlet. The modulus of the reflected acoustic wave is seen to tend towards zero as the frequency increases. Thus, the acoustic energy loss through the outlet boundary increases with frequency, which is of great importance when studying thermoacoustic instabilities. These results show the strong dependence of the transfer functions on frequency, demonstrating that the compact nozzle hypothesis may not be suited for these applications when considering non-zero frequencies. Figure 4.5 shows the upstream-propagating acoustic wave at the inlet generated by an entropy wave. This wave is responsible for low-frequency instabilities in combustion chambers, as mentioned by Goh and Morgans (2011b) and already observed in some industrial cases (Motheau et al., 2012).

It is interesting to compare the solutions obtained using the linear nozzle with a more realistic geometry. Commonly used nozzles usually have a long diverging region compared to the converging one. This is generally done to avoid flow separation at the diverging section, where an adverse pressure

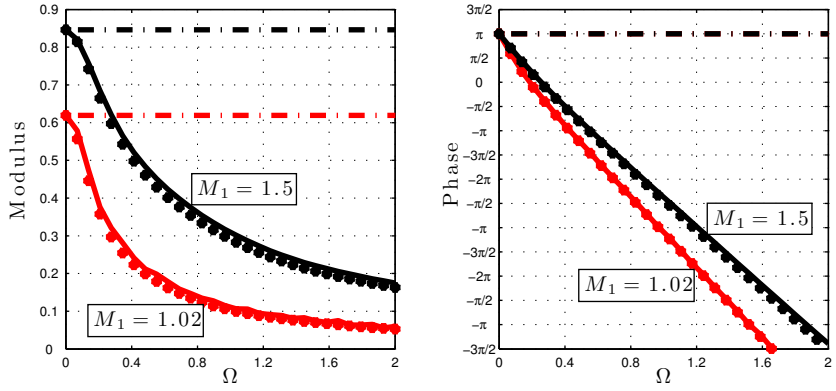

Figure 4.3 – *Amplitude and phase of the upstream-facing acoustic wave at the outlet, w_1^-, generated by an incoming entropy wave, $w_0^s = 1$, with $M_0 = 0.29$. Invariant method (——); hypergeometric equation (•) and compact solution (– · – · –).*

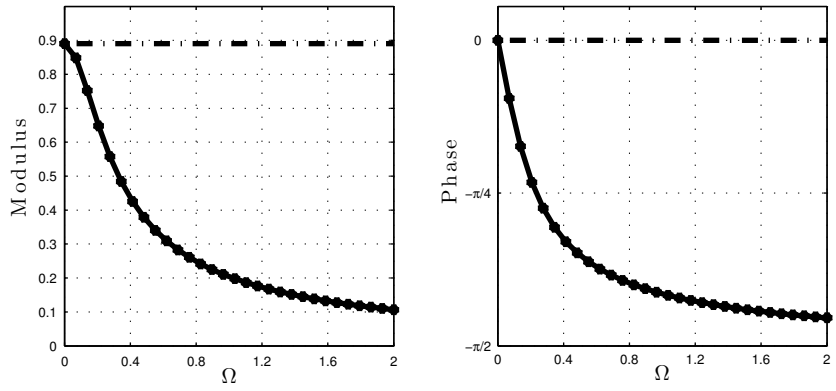

Figure 4.4 – *Amplitude and phase of the reflection coefficient (w_0^- due to w_0^+) for a linear steady velocity choked nozzle with $M_0 = 0.29$ and $M_1 = 1.5$. Invariant method (——); hypergeometric equation (•) and compact solution (– · – · –).*

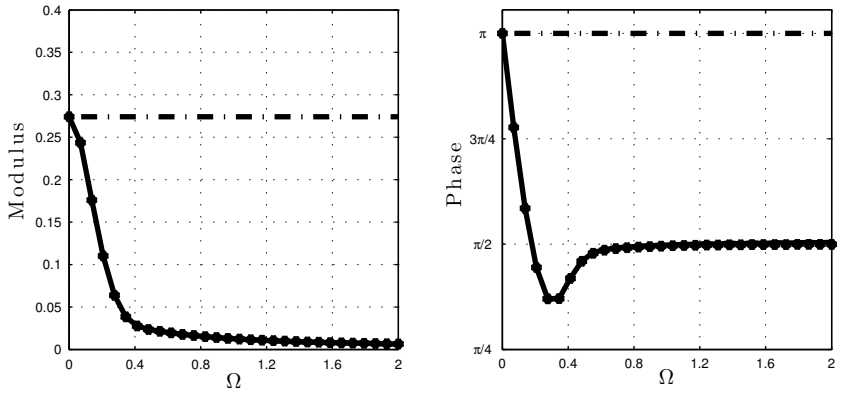

Figure 4.5 – *Amplitude and phase of the acoustic wave, w_0^-, generated by an incoming entropy wave, $w_0^s = 1$, with $M_0 = 0.29$ and $M_1 = 1.5$. Invariant method (——); hypergeometric equation (•).*

gradient exists. When comparing two different geometries with the same inlet and outlet Mach numbers, the compact solution at zero frequency predicts the same values for the transfer functions for both nozzles. This is not the case for non-zero frequencies where the transfer function depends strongly on the Mach number profile, $M(\xi)$, and therefore on the specific geometry considered, and not only on the inlet and outlet Mach numbers. The transfer functions of the linear nozzle are therefore compared with those of a more realistic geometry, with the same inlet and outlet Mach numbers, to evaluate the differences between the transfer functions at non-zero frequencies. The geometry studied here is given by a simple analytical expression dividing the converging and the diverging regions into two parts,

$$\frac{A(\xi)}{A_*} = \begin{cases} \frac{1}{2}\left(\frac{A_0}{A_*} - 1\right)\left[\cos\left(\pi\frac{\xi}{\xi_*}\right) + 1\right] + 1 & \text{if } \xi \in [0, \xi_*] \\ \\ 1 + \left(\frac{A_1}{A_*} - 1\right)\frac{\xi - \xi_*}{1 - \xi_*} & \text{if } \xi \in [\xi_*, 1] \end{cases}, \tag{4.2}$$

where $A(\xi)$ is the nozzle section. Subscript $(\ )_*$ represents the throat section where $M_* = 1$. The nozzle is fully described with three parameters: the non-dimensional converging length ($\xi_* = 0.15$ for the rest of this section) and the inlet and outlet dimensionless section ratios A_0/A_* and A_1/A_*, which are related to the inlet and outlet Mach numbers through (4.1). A cosine profile was chosen for the converging region to yield a smooth flow up to the throat, while the diverging section was chosen to be linear, so

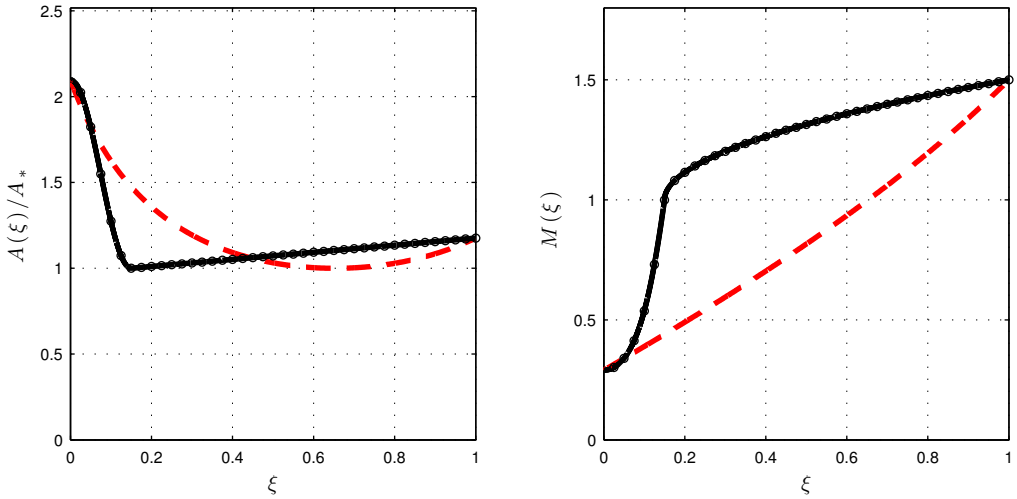

Figure 4.6 – *Section and Mach number of a converging-diverging nozzle. Geometry obtained with (4.2) (——) and with the linear steady velocity profile (– – –), with inlet and outlet Mach numbers $M_0 = 0.29$ and $M_1 = 1.5$ for both nozzles. (•) represents the nozzle subdivisions for the invariant method for calculation up to $\Omega = 5$.*

that the radius is proportional to $\sqrt{x}$, which is a usual feature of rocket engines. This allows a complete description of the nozzle with only three parameters. The nozzle geometry and Mach number are shown in figure 4.6 for the $M_0 = 0.29$ and $M_1 = 1.5$ case used here, compared with the previous geometry obtained for the linear nozzle. Note that the diverging region is larger in the realistic nozzle than in the linear one, and that the geometry and Mach number distribution are significantly different from that of the linear velocity profile.

Using the nozzle geometries shown in figure 4.6, the transfer functions of an incident acoustic wave are calculated. The subdivision used in the Magnus expansion to reach $\Omega = 5$ are also shown. Figure 4.7 shows the downstream-propagating acoustic wave at the outlet generated by an acoustic wave at the inlet, and figure 4.8 shows the reflection coefficient of the nozzle, calculated both for the linear nozzle using the hypergeometric solution of the Section 2.3, and for the realistic nozzle of (4.2) using the invariant method and the Magnus expansion. As expected, at zero frequency there is no difference between the two nozzles, but both the modulus and phase of the transfer functions present large differences when considering non-zero frequencies, even if the inlet and the outlet Mach numbers are the same.

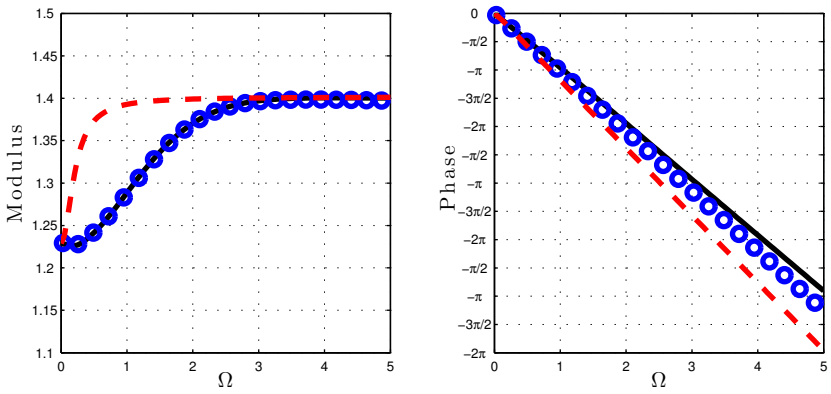

Figure 4.7 – *Amplitude and phase of the acoustic wave at the outlet, w_1^+, generated by an incoming acoustic wave at the inlet, w_0^+. Geometry obtained with (4.2) and solved using the invariant method (——) and numerically (∘); linear steady velocity profile (– – –).*

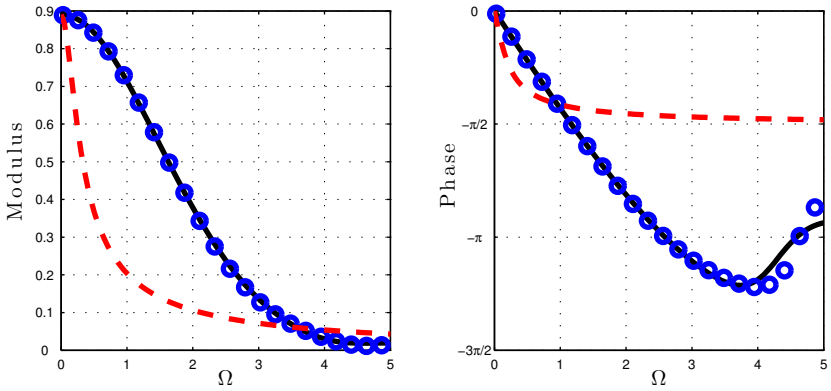

Figure 4.8 – *Amplitude and phase of the reflected acoustic wave at the inlet, w_0^-, generated by an incoming acoustic wave at the inlet, w_0^+. Geometry obtained with (4.2) and solved using the invariant method (——) and numerically (∘); linear steady velocity profile (– – –).*

This shows that, while for the compact case the transfer functions depend only on the inlet and the outlet Mach numbers, the non-compact solution depends strongly on the evolution of the mean flow through the nozzle and therefore on the nozzle geometry.

The transfer functions of the realistic nozzle geometry calculated with the Magnus expansion are also compared with a numerical solver (Silva, 2010; Giauque et al., 2012), solving the linearised Euler equations in the

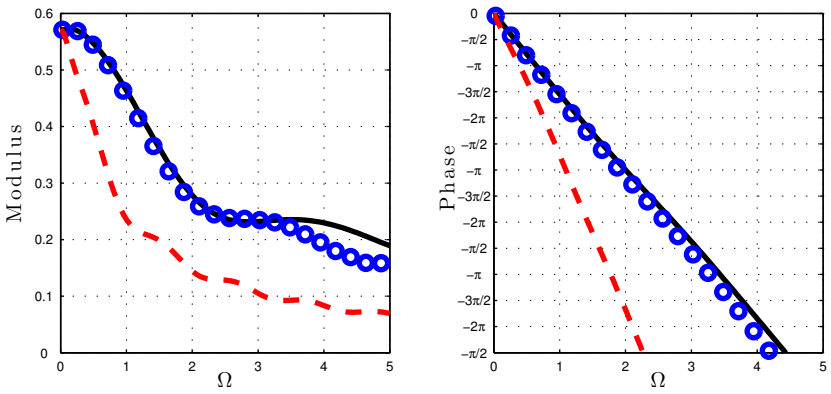

Figure 4.9 – *Amplitude and phase of the acoustic wave at the outlet, w_1^+, generated by an incoming entropy wave at the inlet, w_0^s. Geometry obtained with (4.2) and solved using the invariant method (——) and numerically (∘); linear steady velocity profile (– – –).*

frequency domain with a second order centered spatial scheme. The discretisation is such as to have at least 100 points per acoustic wavelength for $\Omega = 5$ at the inlet. It can be seen that the analytical method agrees with the numerical simulations, and some discrepancies can be found only at high values of the reduced frequency. Figure 4.9 shows the indirect noise generated by an entropy wave in the same nozzle. Again, it should be noted that the transfer function depends on the nozzle geometry (and not only on the inlet/outlet Mach number) for non-zero frequencies. The transfer functions of the realistic nozzle geometry are again compared with numerical simulations, showing a good agreement up to $\Omega = 3$, at which point the numerical scheme starts to present some dispersion of the entropy wave. The same numerical discretisation as for the acoustic transfer function has been used, and therefore about 30 points per entropy wavelength are used at $\Omega = 5$. The computational cost of solving the linearised Euler equations numerically is at least 100 times larger than computing the Magnus expansion of Section 3.2, and for a fixed numerical resolution (number of points per entropy wavelength) this difference increases as the minimum Mach number of the nozzle decreases.

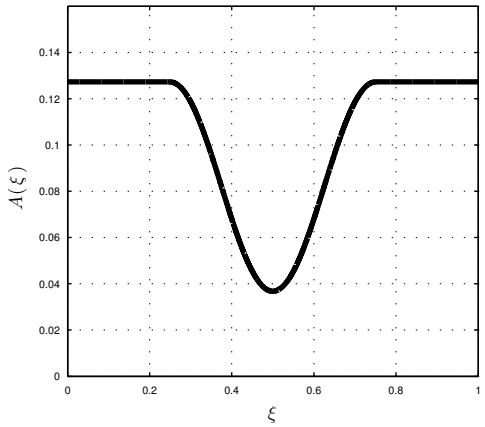

Figure 4.10 – *Plot of $A(\xi)$ of the nozzle of Stow et al. (2002).*

4.2 Comparison with the 'equivalent nozzle length' method for choked nozzles

In the previous section, the invariant method was compared with the linearised velocity profile method, showing that both methods give the same results. At the same time, it was shown that the non-compact response of nozzles depended strongly on the nozzle shape, and not only on the inlet and outlet Mach numbers, as is the case with the compact solution.

In this section, the invariant method will be compared with the 'equivalent nozzle length method', discussed briefly in Section 2.4. The geometry considered for this analysis is the one used by Stow et al. (2002) for their study (see figure 4.10), with a choked flow. Figure 4.11 shows the reflection coefficient of the choked nozzle obtained using both methods. It is shown that the effective nozzle length successfully corrects the phase of the reflection coefficient. The invariant method, however, corrects both the phase and the modulus of the transfer functions. The numerical results of Stow et al. (2002) are also reproduced in the figure for the sake of comparison. The equivalent nozzle length method was extended by Goh and Morgans (2011a) to compute the phase of the transmission coefficients for the acoustic and entropy waves. This method is based on the combination of several equivalent lengths through the convergent and the divergent sections, to obtain the correct phase prediction of the transfer functions of the nozzle in a similar way to the reflection coefficient (for more details see Goh and Morgans (2011a)). This method corrects only the phase shift of the fluc-

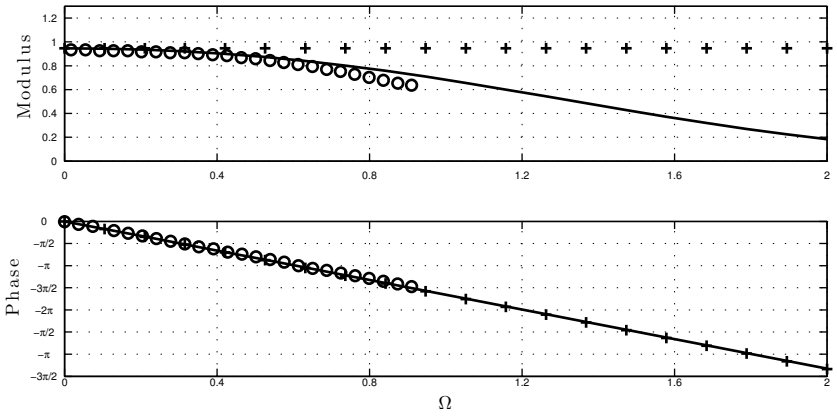

Figure 4.11 – *Amplitude and phase of the reflected acoustic wave at the inlet of the nozzle (w_0^- due to w_0^+). Stow's equivalent length method, (+), Stow's numerical results (∘), and invariant method (━━).*

tuations. However, when considering a shock wave in the divergent section (as explained in Section 3.3.3), a correction of the modulus is also obtained related to the shock wave itself, and not to the propagation of waves through the nozzle. Their results are compared here with the invariant method for three flow configurations: choked, choked with a shock wave at the outlet and choked with a shock wave in the divergent section. For simplicity, the geometry used is the same as the one used by Goh and Morgans (2011a), where the steady Mach number has been calculated analytically using the steady quasi-1D equations and is plotted in figure 4.12 for the three flow configurations studied hereafter.

Figures 4.13 and 4.14 show the acoustic wave at the outlet of the nozzle, generated by an acoustic and an entropy perturbation at the inlet for the choked case. The transfer function is computed using three different methods: the compact hypothesis of Marble and Candel (1977), the first order correction of the phase (Goh and Morgans, 2011a) and the invariant method previously presented. Results show that the equivalent length method of Goh gives a fair correction of the transmission coefficient phase for small frequencies only. The modulus of the transmission coefficient, however, is also found to vary with the frequency of the inlet perturbation due to the non-compact propagation of waves through the nozzle. This effect represents a significant difference at non-zero frequencies, which cannot be corrected with the equivalent nozzle length method, showing the advantage of the complete analytical solution of the linearised Euler equations up to

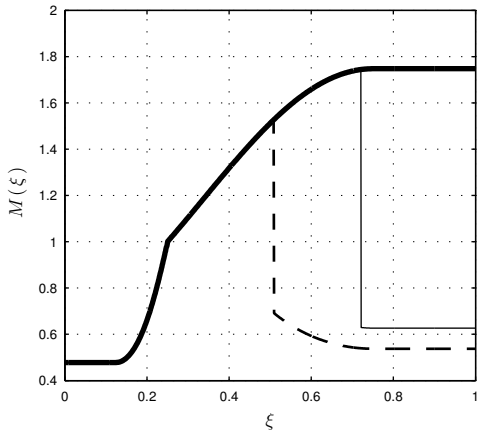

Figure 4.12 – *Plot of $M(\xi)$ for the nozzle used in Goh and Morgans (2011a) for three flow configurations: choked isentropic (thick line), choked with a shock wave at the nozzle outlet (thin line) and choked with a shock wave in the divergent (dashed line).*

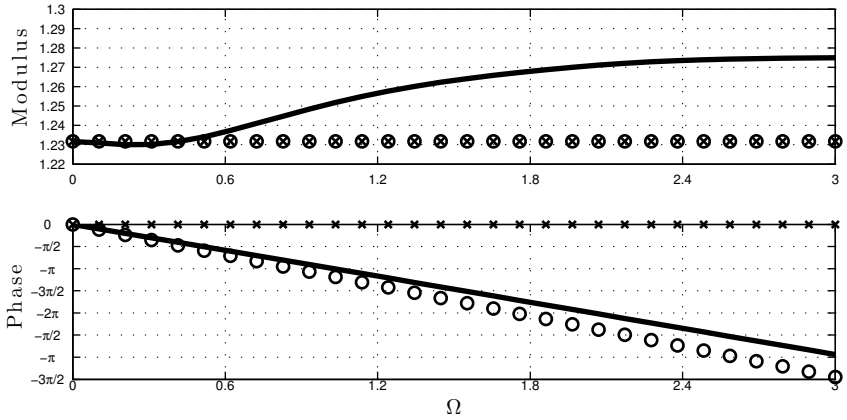

Figure 4.13 – *Amplitude and phase of the transmitted acoustic wave generated by an acoustic perturbation at the inlet for a choked nozzle. Equivalent nozzle length method (∘), Marble and Candel method (×) and invariant method (━━).*

any order in Ω.

When considering a flow with a shock wave inside the nozzle, the interaction of the acoustic waves with the shock has to be considered, as seen in Section 3.3.3. To begin with, the case of a shock wave at the outlet of the nozzle is considered, as done by Goh and Morgans (2011a). In this case, the terms $dM_a/d\xi$ of (3.43) are zero and the transfer functions through the shock wave therefore become frequency-independent. Figures 4.15 and 4.16

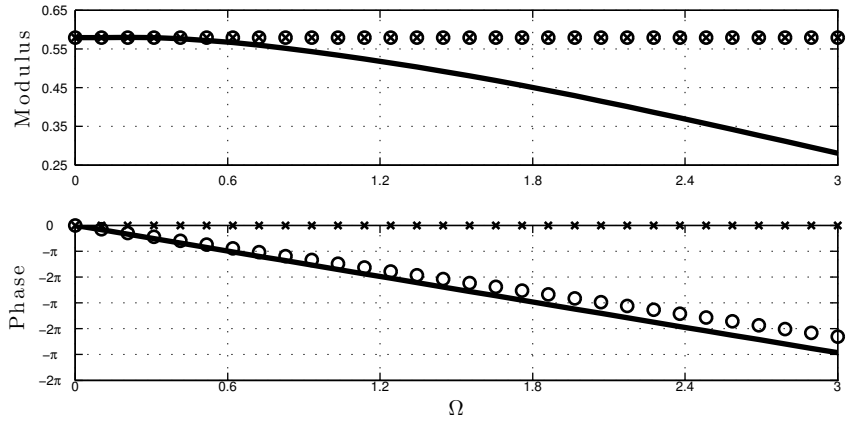

Figure 4.14 – *Amplitude and phase of the transmitted acoustic wave generated by an entropy perturbation at the inlet for a choked nozzle. Equivalent nozzle length method (∘), Marble and Candel method (×) and invariant method (——).*

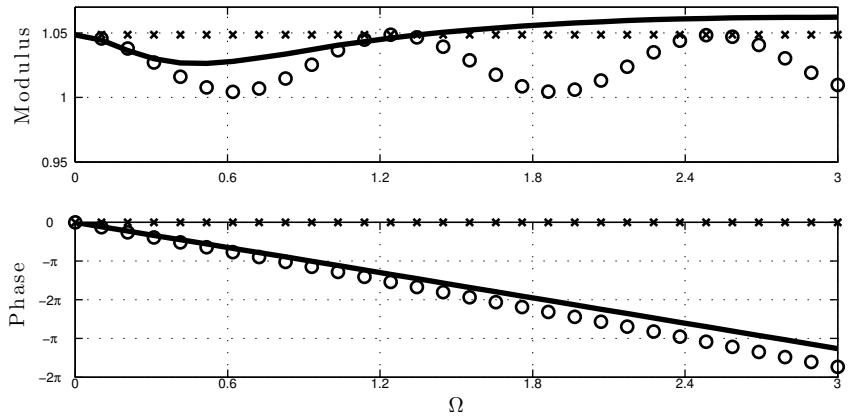

Figure 4.15 – *Amplitude and phase of the transmitted acoustic wave generated by an acoustic perturbation at the inlet for the choked case with a shock wave at the end of the nozzle. Equivalent nozzle length method (∘), Marble and Candel method (×) and invariant method (——).*

show the acoustic wave generated at the outlet by both an incoming acoustic and entropy wave at the inlet, respectively, calculated using Marble and Candel's compact solution for the propagation of waves through a nozzle with a shock wave, the equivalent length method of Goh and the invariant method. Both corrective methods again present a close agreement for low frequencies, although the first order correction of the phase through the equivalent nozzle length fails to correctly predict the modulus of the transfer functions at higher frequencies.

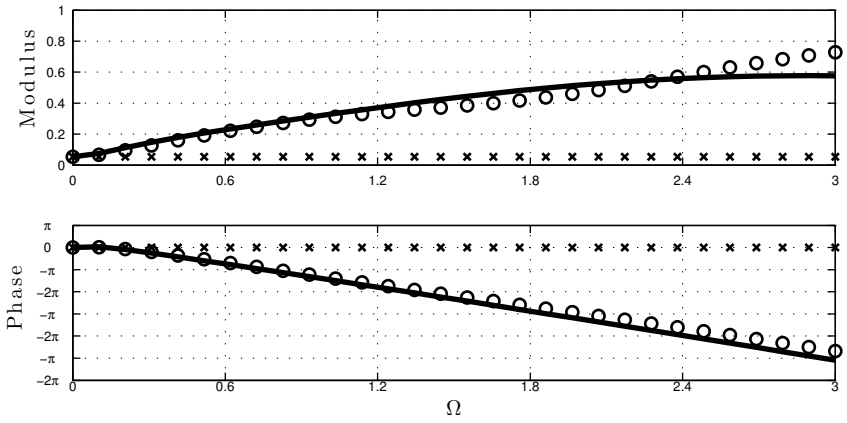

Figure 4.16 – *Amplitude and phase of the transmitted acoustic wave generated by an entropy perturbation at the inlet for the choked case with a shock wave at the end of the nozzle. Equivalent nozzle length method (∘), Marble and Candel method (×) and invariant method (——).*

The study of the stability of shock waves in a nozzle shows that they are stable only when located in the diverging region of the nozzle. This is why the study of the interaction of acoustic waves with the shock wave must be done when it is located in the divergent section. The shock wave will therefore fluctuate in a region of the nozzle where a mean density, pressure, Mach number and velocity gradient exist. Taking into account these mean flow gradients, the solution explained in Section 3.3.3 is obtained. In this case, the transfer functions of the acoustic and entropy waves through the shock wave are frequency-dependent regardless of the compactness of the nozzle. This is caused by the frequency dependence of the acoustic transfer functions through a shock wave, as seen in Table 3.1. Figures 4.17 and 4.18 show the acoustic wave at the outlet of the nozzle generated both by an acoustic and an entropy wave at the inlet, respectively, calculated using Marble and Candel's method, the equivalent nozzle length method of Goh and Morgans and the invariant method. Results show a good agreement for low frequencies between the invariant method and the equivalent nozzle length method, where the propagation of waves through the nozzle can be considered compact and therefore the frequency dependence of the solution is driven by the transfer functions of the shock wave (Table 3.1). At larger frequencies, however, discrepancies are found, caused by the variation of the modulus of the transfer functions of the nozzle upstream and downstream of the shock wave, which Goh and Morgans calculate using the compact nozzle assumption. It should be noted that Marble and Candel's solution shown

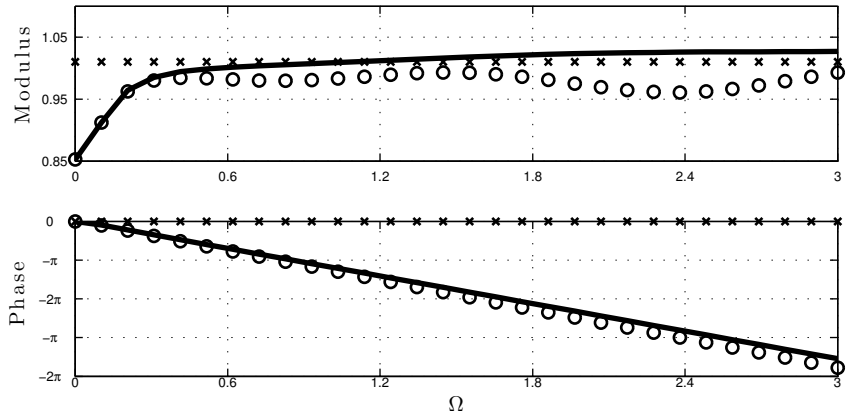

Figure 4.17 – *Amplitude and phase of the transmitted acoustic wave generated by an acoustic perturbation at the inlet for the choked case with a shock wave. Equivalent nozzle length method (∘), Marble and Candel method (×) and invariant method (——).*

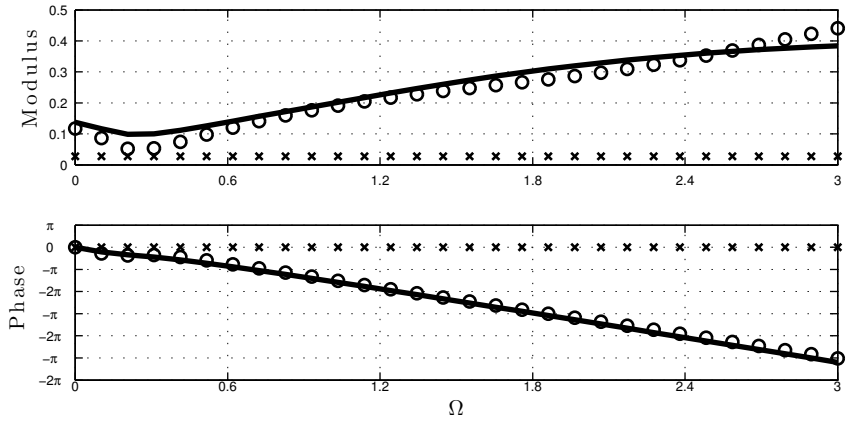

Figure 4.18 – *Amplitude and phase of the transmitted acoustic wave generated by an entropy perturbation at the inlet for the choked case with a shock wave. Equivalent nozzle length method (∘), Marble and Candel method (×) and invariant method (——).*

in figures 4.17 and 4.18 does not consider the mean Mach number gradient in (3.37-3.39), and therefore is constant in terms of frequency and does not agree with the solutions obtained in Section 3.3.3.

4.3 Comparison with experimental measurements

The analytical method proposed in Section 3.2 eliminates the compact assumption previously used to calculate the transfer functions of the nozzle, but is still based on strong assumptions. These simplifications, such as considering a steady, inviscid main flow, neglecting boundary layers or considering a 1D flow inside the nozzle, can only be verified when compared either with fully turbulent 3D high-fidelity numerical simulations in which every length-scale of the flow is considered, or with experimental data in real configurations. Zinn et al. (1973) and Bell et al. (1973) developed an experiment to measure the admittance of several rocket engine nozzle geometries, showing the influence of the nozzle geometry on the admittance at non-zero frequencies. The experiment is used in this section to validate the assumptions made in the invariant method.

The axisymmetric nozzles considered by Bell et al. (1973) are shown in figure 4.19, where the contour of the nozzle, $r(x)$, is plotted. They are made up of three sections: first a circular arc of radius r_{cc} starting at the inlet and turned at an angle of θ_1; this arc joins a conical section with the same half-angle, connecting with the third part, a circular arc of the same radius turned at an angle of θ_1. Knowing that the nozzles are all choked, the geometry of the converging section is fully defined with the inlet Mach number and the two geometrical parameters θ_1 and r_{cc}/r_c (the ratio of curvature of the inlet and outlet arcs over the nozzle inlet radius). As the nozzles are choked, the diverging section is not detailed as it has no effect on the reflecting properties at the inlet (waves do not propagate upstream in the supersonic part).

To compare against experimental data, the admittance (Y) will be used, which is defined as the inverse of the impedance of the nozzle (Z), and can be calculated as

$$Y = \frac{1}{Z} = \rho c \frac{u'}{p'}\bigg|_0 = \frac{M\nu}{\varphi}\bigg|_0 . \tag{4.3}$$

To calculate the admittance using the analytical method, the mean flow is obtained by solving (4.1), and therefore viscous effects, boundary layers and 2D/3D effects are neglected. The invariant equation is solved setting all incoming waves to zero, except the incoming acoustic wave $w_0^+ = 1$. The reflected wave w_0^- is obtained in this way and, using (2.19), the admittance

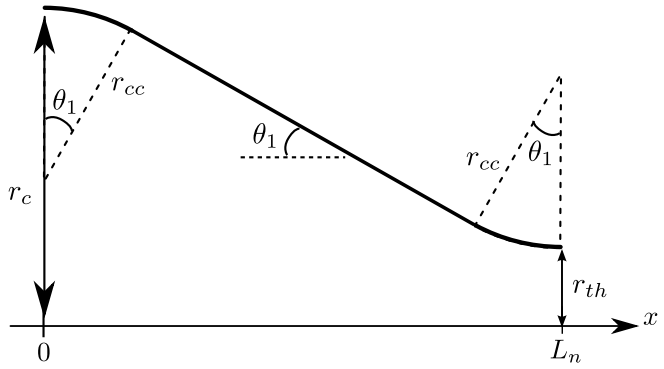

Figure 4.19 – *Axisymmetric nozzle geometry of Bell et al. (1973).*

can be calculated as

$$Y = \frac{w_0^+ - w_0^-}{w_0^+ + w_0^-} = \frac{1 - R_0}{1 + R_0}, \tag{4.4}$$

where $R_0 = w_0^-/w_0^+$ is the reflection coefficient. Results in this section are plotted as a function of the non-dimensional frequency $S = 2\pi f r_c/c_0$, as done by Bell et al. (1973), where the angular frequency $(2\pi f)$, the nozzle inlet radius (r_c) and sound speed (c_0) are used. This reduced frequency can be easily related to the one used in previous sections ($S = 2\pi\Omega r_c/L_n$), but S will be used in this section, as done by Bell et al. (1973), in order to be able to compare with their results.

Out of all the cases studied by Bell et al. (1973), three will be considered here: an inlet Mach number of 0.08, a radius ratio $r_{cc}/r_c = 0.44$ and three half-angles, $\theta_1 = 15$, 30 and 45. Figure 4.20 shows the admittance of the three nozzles computed with the analytical method of Section 3.2, compared to the experimental values. Bell et al. (1973) compared their results with Crocco's theory (Crocco and Sirignano, 1967), with which, under similar assumptions as used for the invariant theory, the nozzle admittance was obtained by integrating numerically a non-linear Riccati equation. These numerical results perfectly match the invariants solution but are not shown here (see figure 4 of Bell et al. (1973)). In figure 4.20 the analytical solution obtained with the flow invariants using the Magnus expansion compares well with the experimental data within the experimental error and the limitations of the invariant theory. This shows that the invariant theory can be used to compute reflection coefficients (impedances or admittances) of rocket engine nozzles or gas-turbine nozzles for combustion instability studies. The results also illustrate that the reflecting properties of 1D nozzles strongly depend on the geometry of the converging section when considering

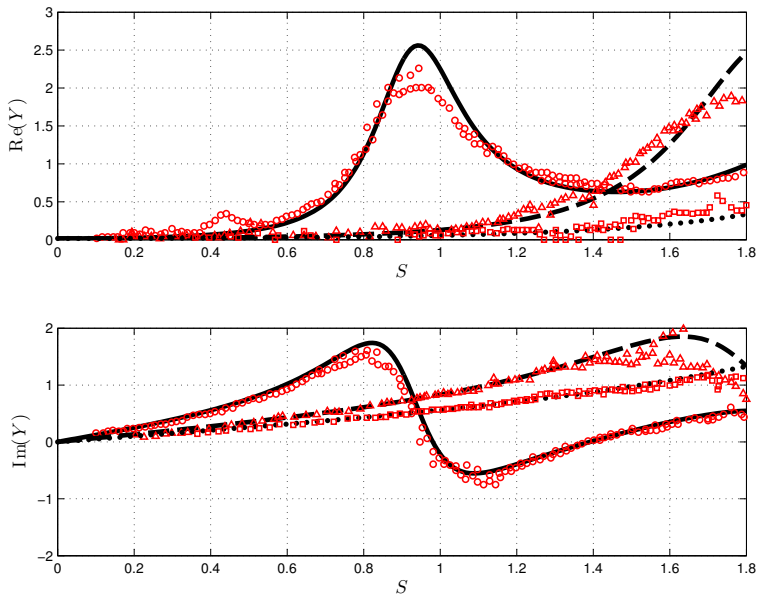

Figure 4.20 – *Real and imaginary parts of the acoustic admittance Y of three different choked nozzles; $M_0 = 0.08$, $r_{cc}/r_c = 0.44$. For $\theta_1 = 15$: analytical (——), experiments (∘). For $\theta_1 = 30$: analytical (– – –), experiments (△). For $\theta_1 = 45$: analytical (· · ·), experiments (▪).*

non-zero frequencies, showing the interest of an analytical method able to solve the propagation of waves through any nozzle geometry, even if strong assumptions are still being made.

4.4 Study of subsonic nozzles

The solution of the LEEs using the invariant method and the Magnus expansion proposed in Section 3.2 can also be used to solve subsonic nozzles of any considered geometry. The nozzle analysed here was used for the Entropy Wave Generator (EWG) experiment. This experiment, performed by Bake et al. (2009), studied the indirect noise generated by a convected entropy wave through a nozzle. The subsonic response of the nozzle is studied here as an example for several Mach number profiles, as seen in figure 4.21 and in Table. 4.1. To do so, a non-reflecting boundary condition is imposed both at the inlet and at the outlet, since we are only interested in the transfer functions. Figure 4.22 shows the acoustic transmitted and reflected waves generated by a unitary entropy wave at the inlet for several throat Mach

	Inlet Mach Number (M_0)	Throat Mach Number (M_T)	Outlet Mach Number (M_1)
Case 1	0.0305	0.6	0.0171
Case 2	0.0331	0.7	0.0186
Case 3	0.0349	0.8	0.0196

Table 4.1 – *Mach numbers in the EWG nozzle for the three mean flow configurations considered.*

numbers. The result shows that the response of the nozzle at non-zero frequencies is significantly different from the solution obtained at $\Omega = 0$. For instance, at $\Omega = 0.1$ the transmitted wave is 40 times larger than the one predicted by the compact theory, and it keeps on increasing with frequency. A similar response is found in the case of the reflected acoustic wave. The compact analysis is therefore limited to very low frequencies in the case of converging-diverging nozzles. The increase of indirect noise generated by the nozzle at non-zero frequencies is caused by the strong acceleration and deceleration of the mean flow in the nozzle throat. This acceleration and deceleration has no effect at zero frequencies, as the indirect noise generated by the converging section is cancelled out by the one generated in the diverging region. This occurs because the indirect noise is generated by the mean velocity gradient of the nozzle, which is positive in the convergent section and negative in the divergent section for subsonic nozzles. At non-zero frequencies, however, the acoustic waves are not perfectly cancelled out due to the phase shift linked to the different propagation speeds of acoustic and entropy waves inside the nozzle. For this reason, indirect noise increases drastically at non-zero frequencies. This does not occur in choked nozzles, as shown in figure 4.2, as the mean velocity gradient is always positive.

Figure 4.22 also shows that, when considering the compact nozzle solution, the response of the nozzle is almost unaltered when changing the Mach number profile. For zero frequencies, the transfer function is only dependent on the inlet and outlet Mach numbers (see Table 2.1), which are only slightly changed for the three cases studied here. However, for increasing frequencies the Mach number profile is shown to have a strong influence on the entropy transfer functions. The entropy transfer function depends on the complete Mach number profile and, in the case of the converging-diverging

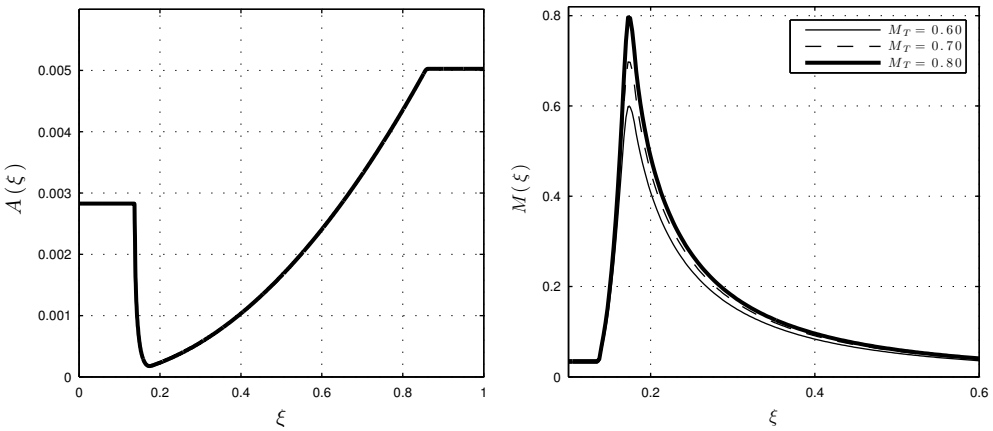

(a) Section (b) Mach number

Figure 4.21 – *Section of the EWG nozzle, and three Mach number profiles, corresponding to three different throat Mach numbers.*

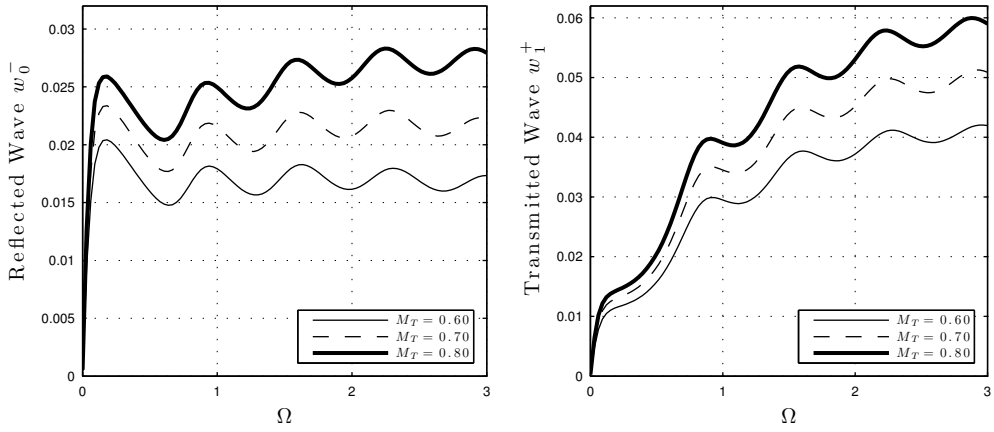

(a) Reflected (b) Transmitted

Figure 4.22 – *Amplitude of the transmitted and reflected acoustic waves generated by an entropy wave in the EWG nozzle, for different throat Mach numbers calculated using the invariant method.*

nozzle studied here, the small variations of Mach number at the inlet induce large variations of the throat Mach number, as seen in Table. 4.1, which will in turn strongly modify the transfer functions at non-zero frequencies.

Figure 4.23 shows the same plot as in figure 4.22 for the case M_T = 0.7, calculated using the Magnus expansion at different orders to show the

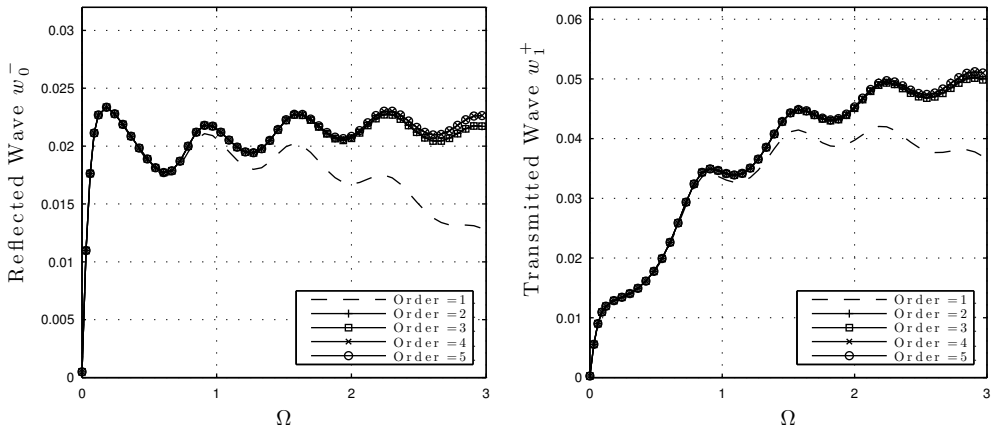

(a) Reflected (b) Transmitted

Figure 4.23 – *Amplitude of the transmitted and reflected acoustic waves generated by an entropy wave in the EWG nozzle, for M_T = 0.7 calculated using the invariant method at different orders of the Magnus expansion.*

convergence of the method. It can be seen that an order four or five is enough to calculate the modulus of the entropy transfer functions.

The EWG nozzle geometry can be used to study the response of a subsonic nozzle to acoustic perturbations. In figure 4.24 the reflection and transmission coefficients similarly show that the solution for non-zero frequencies strongly differs from the compact solution at $\Omega = 0$. The evolution of the reflection coefficient of this subsonic nozzle is the inverse of the one observed in the choked nozzle (Figure 4.4): in the choked case the reflection coefficient at $\Omega = 0$ is about 0.9 and tends towards zero when Ω increases, while for the subsonic case the reflection coefficient is small at $\Omega = 0$ and increases thereafter towards one.

In the case of acoustic disturbances entering the nozzle, the influence of the Mach number profile through the nozzle is very limited. Figure 4.24 shows that the three cases studied are almost identical.

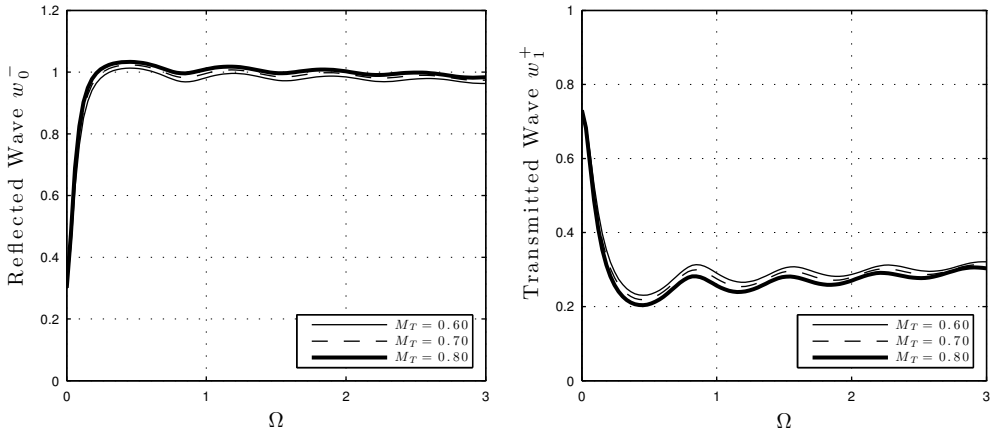

Figure 4.24 – *Amplitude of the acoustic transmission and reflection coefficients of the EWG nozzle calculated using the invariant method.*

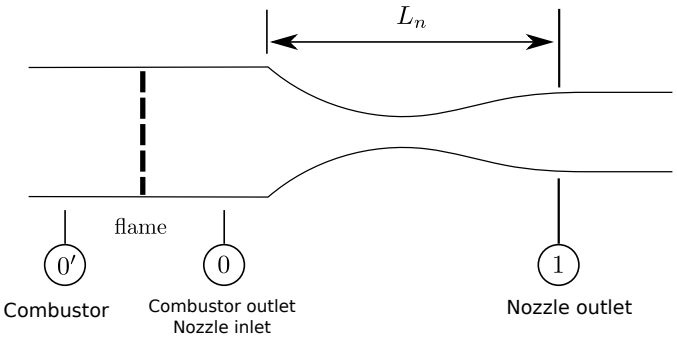

Figure 4.25 – *Simplified model of a combustor used by Leyko et al. (2009).*

4.5 Parametric study on direct and indirect combustion noise

The analytical solution of the LEEs using the invariant method can be used to perform a parametric study of combustion noise at the outlet of a combustion chamber, which is critical for an accurate estimate of transmission losses through turbine stages and could explain the observed aft spectra of small turbo-engines and helicopter turbo-shaft engines. When a turbulent confined flame fluctuates, it generates both entropy and acoustic waves. The propagation of these waves generates two types of noise: direct noise, produced by the acoustic waves that propagate through the turbine stages and reach the outlet, and indirect noise, generated inside the turbomachinery by the acceleration of entropy waves generated during combustion. The relative importance of indirect noise is therefore linked to the propagation of waves through a non-uniform flow. Leyko et al. (2009) compared the direct and indirect combustion noise generated in a model combustor. The analysis performed was based on a simple tube with a one-dimensional cold flame followed by a compact converging-diverging nozzle, as illustrated in figure 4.25. A cold flame is a simplification in which a flame is considered to generate only fluctuating heat release, with no mean value. With this simplification, the mean flow upstream and downstream of the flame are assumed to be equal, as was done by Leyko et al. (2009). Using this simple model, the ratio of indirect to direct noise generated by a fluctuating heat release was estimated for different Mach numbers using the compact nozzle hypothesis. To solve the compact cold flame, Leyko et al. (2009) used the compact equations (2.16a)-(2.16c), written between the inlet and the outlet of the cold flame, with a fluctuating heat source term, $\dot{Q}'$, in both the energy and the entropy equations:

$$\left(\dot{m}'\right)_{0'} = \left(\dot{m}'\right)_0, \tag{4.5}$$

$$\left(c_p \dot{m} T_t'\right)_{0'} + \dot{Q}' = \left(c_p \dot{m} T_t'\right)_0, \tag{4.6}$$

$$\left(\dot{m} s'\right)_{0'} + \frac{\dot{Q}'}{T} = \left(\dot{m} s'\right)_0. \tag{4.7}$$

Defining the dimensionless fluctuating heat release as $q' = \dot{Q}'/(\dot{m} c_p T)$ and knowing that $M_{0'} = M_0$ for the cold flame, the equations can be written

using the primitive variables:

$$(\varphi+\nu-\sigma)_{0'} = (\varphi+\nu-\sigma)_0\,, \tag{4.8}$$

$$\left((\gamma-1)M^2\nu+(\gamma-1)\varphi+\sigma\right)_{0'}+q' = \left((\gamma-1)M^2\nu+(\gamma-1)\varphi+\sigma\right)_0 \tag{4.9}$$

$$(\sigma)_{0'}+q' = (\sigma)_0\,. \tag{4.10}$$

Using the wave definition (2.19) and imposing no incoming waves ($w^+_{0'}=0,\ w^s_{0'}=0,\ w^-_0=0$), the outgoing entropy and acoustic waves generated by the heat release fluctuation, q', read

$$w^s_0 = q', \quad w^+_0 = \frac{M_0}{1+M_0}q' \quad \text{and} \quad w^-_{0'} = \frac{M_0}{1-M_0}q'. \tag{4.11}$$

The ratio of indirect to direct combustion noise, η, is defined as the ratio of the acoustic waves generated at the outlet of the nozzle by the entropy waves (indirect noise), to the acoustic waves at the outlet generated by the propagation of the acoustic waves produced by the fluctuating heat release. It follows that

$$\eta = \underbrace{\frac{w^+_1}{w^s_0}}_{\text{entropy TF}} \times \underbrace{\frac{w^s_0}{w^+_0}}_{\text{wave ratio}} \times \underbrace{\left[\frac{w^+_1}{w^+_0}\right]^{-1}}_{\text{acoustic TF}}, \tag{4.12}$$

where the 'wave ratio' term is obtained from (4.11). The first term is the entropy transfer function of the nozzle, which gives the acoustic wave generated by a unitary entropy wave. Similarily, the third term is the acoustic transfer function. Leyko et al. (2009) calculated both transfer functions using the compact nozzle hypothesis (Tables 2.1 and 2.2), obtaining an analytical expression

$$\eta = \frac{1}{M_0}\frac{(M_1-M_0)(M_1+M_0)}{2\left(1+\frac{1}{2}(\gamma-1)M_1^2\right)} \qquad \text{for subsonic nozzles, and} \tag{4.13}$$

$$\eta = \frac{1+M_0}{M_0}\frac{(M_1-M_0)}{2\left(1+\frac{1}{2}(\gamma-1)M_1\right)} \qquad \text{for the choked case.} \tag{4.14}$$

Using this compact solution, Leyko et al. (2009) evaluated the ratio of indirect to direct noise for different inlet and outlet Mach numbers. The invariant method is used here to obtain the indirect to direct noise ratio as a function of the frequency of the fluctuating heat release. To do so, the nozzle geometry of (4.2) is considered for the choked cases. In the subsonic case only a converging section is used for simplicity. The invariant method is solved for different inlet and outlet Mach numbers to calculate the indirect

to direct noise ratio, η, for reduced frequencies Ω from 0 to 2.5. In total 2,500 different nozzle geometries are solved at six frequencies, the complete calculation taking less than 2.5 hours on a single CPU (2.66 GHz). Figure 4.26 shows the noise ratio as a function of the inlet and the outlet Mach numbers for several frequencies. The results show a perfect agreement between the compact solution and the invariants one calculated at $\Omega = 0$. For larger frequencies, the indirect to direct noise ratio decreases as Ω increases, which means indirect noise is only significant at low frequencies and could be neglected at high frequencies.

The results can be analysed through previous results obtained in Section 4.1. Figure 4.2 shows that, for choked nozzles, the indirect noise generated by a unitary entropy wave at the inlet decreases with increasing frequency. On the other hand, the direct noise generated by an acoustic wave at the inlet (shown in figure 4.7 for the same nozzle) increases slightly with Ω and then remains constant. The effect of both terms will add up to give an indirect to direct noise ratio, η, that will decrease with Ω. In the subsonic region of figure 4.26 it can also be seen that the indirect to direct noise ratio decreases with increasing frequency. However, this result can be shown to depend on the nozzle geometry considered. As previously stated, a converging geometry has been used to perform the parametric study. Section 4.4 showed the case of a subsonic converging-diverging nozzle, with low inlet and outlet Mach numbers but a strong acceleration of the flow at the nozzle throat. The results in figures 4.22 and 4.24 show that indirect noise increases with frequency and that direct noise decreases, giving therefore an indirect to direct noise ratio that will strongly increase with frequency for the considered nozzle geometry. This shows the importance of an analytical solution valid for any nozzle geometry and any flow condition.

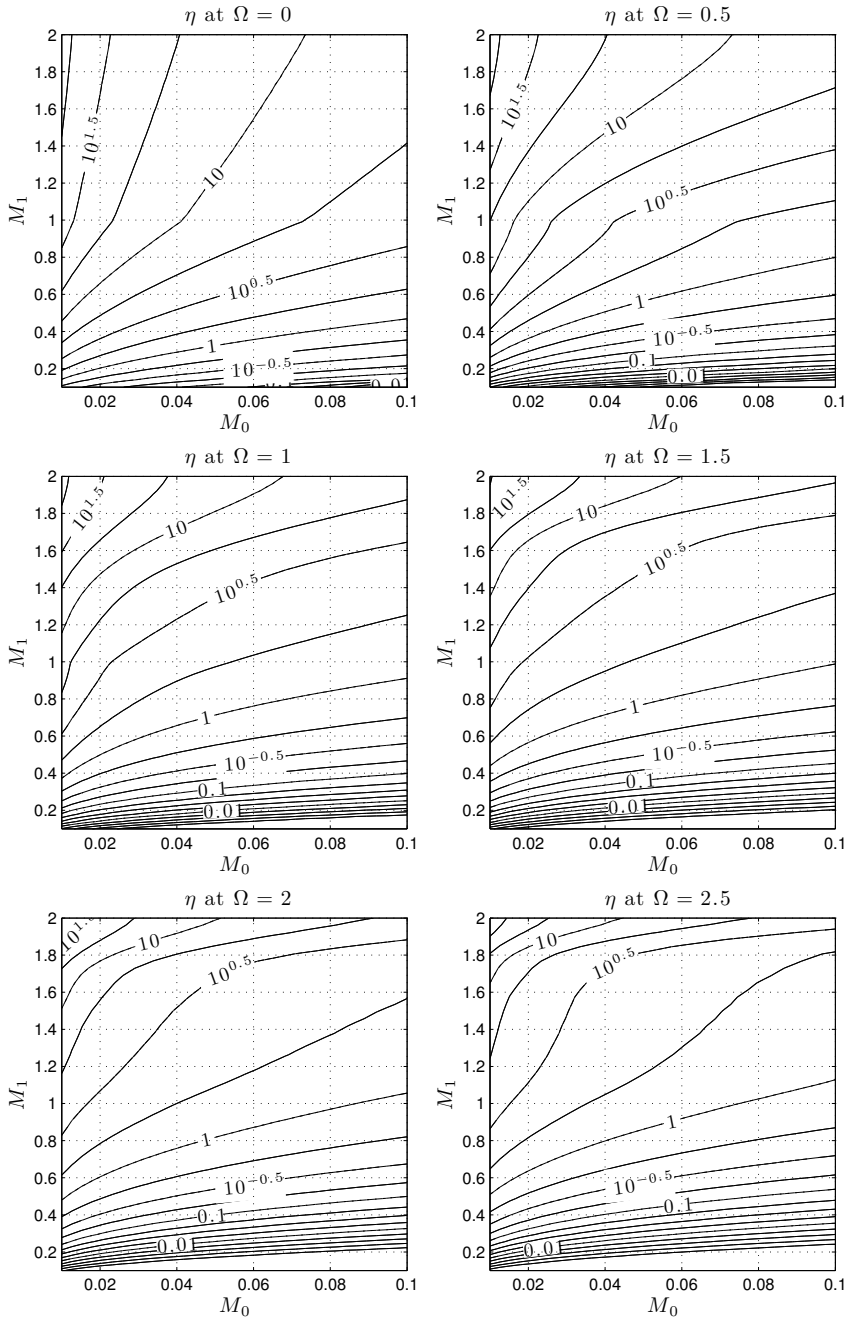

Figure 4.26 – *Indirect to direct noise ratio, η, calculated using the invariant method as a function of the inlet and the outlet Mach numbers of the nozzle, M_0 and M_1, for different frequencies.*

Conclusions

An analytical solution for the one-dimensional linearised Euler equations has been found, combining the invariants equations with the Magnus solution of a linear system of differential equations with varying coefficients. Boundary conditions have been applied for both subsonic and choked cases. This solution has been successfully validated with the analytical solution found by Marble and Candel (1977) for the case of a nozzle with a linear steady velocity profile. The analytical method through the flow invariants extends the solution of both Stow et al. (2002) and Goh and Morgans (2011a), predicting both the phase and the modulus of the transfer functions as a function of frequency in any flow configuration with any nozzle geometry, and generalising the solution up to any order in the asymptotic expansion. The present solution also removes the inherent assumption of a piecewise-linear approximation of the velocity profile in the nozzle, used by Moase et al. (2007) in their generalisation of the hypergeometric solution of Marble and Candel (1977). It can deal with any arbitrary velocity profile in C^0, or equivalently any nozzle geometry and back-pressure. Therefore, the present method based on the invariants equation and the Magnus expansion extends and unifies all existing asymptotic or piecewise solutions to the quasi-one-dimensional linearised Euler equations, and prevents any convergence, dispersion and dissipation issues and computational cost associated with numerical methods.

The results show that the transfer functions of choked nozzles vary strongly with the frequency of the perturbation. This strong variation affects both the transmission and the reflection coefficients of entropy and acoustic waves, and should be taken into account to correctly predict combustion noise and thermoacoustic instabilities.

The linear steady velocity nozzle profile has also been compared with

more realistic nozzles, where the geometry is given through other design constraints such as preventing flow separation in the diverging region. This comparison showed that for non-zero frequencies the transfer functions are dependent on the considered geometry, and differ from one nozzle to another, even if the inlet and outlet Mach numbers are equal. This demonstrates the interest of a general analytical solution in which any nozzle geometry can be solved in any flow configuration.

The subsonic flow has also been investigated using the invariants method. Results showed that, for the converging-diverging subsonic nozzle used in the EWG experiment, the acoustic waves generated by entropy waves (indirect noise) strongly depend on the frequency of the perturbation. A similar conclusion was drawn when studying the acoustic response of the nozzle, showing again that the non-compact effect should be taken into account when studying noise propagation through accelerating and decelerating flows.

The assumptions made when using the one-dimensional linearised Euler equations limit the results to frequencies lower than the first cut-off frequency and, at the same time, to 1D inviscid flows. The solution has been compared with experimental data from rocket engine nozzles showing a significant agreement, regardless of the assumptions made. This shows that the method can be used to obtain a correct estimate of the reflection coefficient of nozzles, even if the flow details, turbulence and boundary layers are neglected. An improvement of the method could be to consider the boundary-layer displacement thickness to obtain a more realistic mean flow through the nozzle before solving the invariants equations, instead of computing the mean Mach number from an inviscid quasi-1D flow as done here. Parallely, the comparison with experimental data shows that the reflecting properties of a choked nozzle strongly depend on the geometry considered at non-zero frequencies, and that the invariants method is able to predict this behaviour for both the modulus and the phase of the reflecting properties. This is particularly important for the analysis of combustion instabilities as the reflecting condition of choked nozzles monitors the energy loss through the outlet, and therefore the stability of the mode itself.

A parametric study of indirect to direct noise ratio has been finally carried out. This study generalises the work done by Leyko et al. (2009) who made a parametric study of nozzles for the compact case. The non-compact parametric study shows that, for the family of nozzles considered, the indirect to direct noise ratio as defined by Leyko et al. (2009) globally

decreases with frequency, and consequently the indirect noise source should prevail only at low frequencies.

Part II

Propagation of waves through turbine stages

Table of Contents

Introduction **89**

5 Two-dimensional analytical method **93**

5.1 Introduction and assumptions 93

5.2 Wave decomposition 95

5.2.1 Entropy wave 96

5.2.2 Vorticity wave 97

5.2.3 Acoustic waves 98

5.3 Jump conditions through the blade row 100

5.3.1 Stator vane 101

5.3.2 Rotor blade 103

5.4 Solution of the equations and boundary conditions 105

6 Numerical simulations **109**

6.1 Numerical methods 110

6.1.1 Numerical methods for rotation 111

Method A: ALE method 111

Method B: MISCOG method 113

Method C: No-deformation method 113

6.1.2 Boundary conditions and forcing term 114

6.1.3 Post-processing of the waves 118

6.2 Rotor case study 120

Acoustic wave 122

Entropy wave 123

6.3 Stator-Rotor case study 128
Acoustic wave 128
Entropy wave 130

Conclusions **139**

Introduction

The first part of this thesis focuses on the study of waves propagating through non-homogeneous quasi-1D flows. It was seen that the transfer functions of the nozzle depend strongly on both the frequency and the nozzle geometry. The analytical method explained in Chapter 3 is able to compute these transfer functions without any assumption on the nozzle geometry or on the flow. The method has been validated with other analytical methods and numerical results showing, at the same time, the interest of a general analytical solution for any nozzle geometry. The analytical method is able to reproduce the experimental measurements of the reflection coefficients performed by Bell and Zinn (1973) of a quasi-1D choked nozzle, for several nozzle geometries and for any frequency. However, the method still considers a quasi-1D flow through the nozzle, and the real 3D effects cannot be accounted for. Indeed, the flow through a turbine stage has a strong azimuthal component due to the flow deviation of the stator and rotor blades. This deviation is likely to affect the propagation of waves through turbine stages and should be accounted for in the modelling of the turbine stages, as shown by Leyko (2010). Figure 5.0 shows the transfer functions of a stator blade computed using both a 2D and a 1D compact model, illustrating the importance of the 2D effects.

Several analytical and semi-analytical models exist to predict the propagation of acoustic waves through turbine blades in a 2D configuration, such as those developed by Muir (1977a,b), where the blade is treated as a discontinuity and therefore is assumed infinitely short. Kaji and Okazaki (1970a,b) proposed a method for studying the propagation of waves through blades with finite length and finite spacing between them, but with no flow deviation. The model developed by Posson et al. (2010) accounts for cascade effects and the generation of noise by three-dimensional vortical gusts, whilst still considering a flat plate with no flow deviation. These models con-

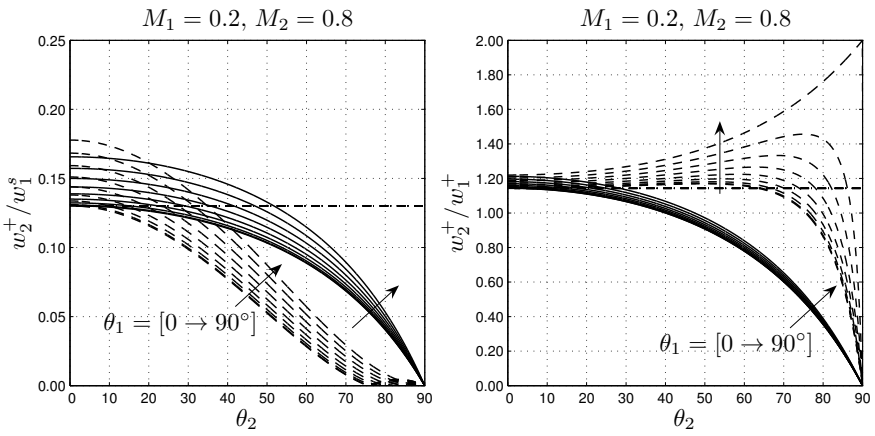

(a) Entropy (b) Acoustic

Figure 5.0 – *Acoustic response of a stator blade at the outlet (2) to a perturbation at the inlet (1) for different flow orientations θ (in degree). Computed using the 2D compact model of Cumpsty and Marble (——); 1D compact model Marble and Candel with Mach number based on the overall velocity magnitude (– · –), or on the axial velocity component (– – –). Figure reproduced from Leyko (2010).*

sider only acoustic and vorticity waves, neglecting entropy fluctuations and therefore indirect noise. To include the effects of entropy waves, Cumpsty and Marble (1977) extended the 1D analytical model of Marble and Candel (1977) for the case of a stator vane in a 2D configuration, accounting for the effect of the flow deviation and including therefore vorticity waves in the model. The method is based on similar assumptions to those used by Marble and Candel (1977) and described in Section 2.2, such as the low frequency assumption. This method was compared by Leyko (2010) with numerical simulations for the case of a single stator vane, showing that the compact low frequency limit of the analytical method predicted correctly the transfer functions (both the reflected and transmitted acoustic waves) generated by acoustic and entropy waves. For the case of direct noise, the compact solution was shown to be valid over a wide range of frequencies. This was not the case for indirect noise, where it was shown that the entropy wave was strongly deformed due to the presence of the stator blade. The indirect noise was nevertheless shown to be correctly predicted for low frequencies, which are dominant in combustion noise applications.

The objective of this section is to analyse the propagation of waves through a complete turbine engine stage. The 2D analytical model of Cumpsty and Marble (1977) is first explained in Chapter 5, taking into account

the effect of the rotor blade. To validate the model, numerical simulations will be used. The set-up of the simulations is explained in Chapter 6, results are discussed in Sections 6.2 and 6.3, and conclusions are finally drawn at the end of Part II.

Note that the method described here (which is the basis of the CHORUS methodology to compute combustion noise, which will be described in detail in Part III) does not incorporate the non-zero frequencies effects discussed in Part I: all derivation discussed here corresponds to a compact limit where the frequency goes to zero. How to incorporate the non-compact effects (Part I) with the rotation effects (Part II) remains an open issue for the moment.

Chapter 5

Analytical method for the propagation of waves through turbine blades

5.1 Introduction and assumptions

This chapter presents the analytical method developed by Cumpsty and Marble (1977) for predicting the propagation of waves through stator blades, considering both fixed and rotating blades. The method is still based on the compact assumption, which considers the wavelengths of the perturbations to be long compared to the axial length of the turbine stages. Under this assumption, the acoustic and entropy waves propagate quasi-steadily through turbine stages and simple jump conditions can be written between the inlet and the outlet of each turbine row, similarly to those for the compact method of Marble and Candel (1977) discussed in Section 2.2 of Chapter 2. In this sense, the present methodology (which is the basis of the reduced-order tool CHORUS), does not include the latest development presented in Chapter 3 and is limited to the compact assumption. The reason for this is that CHORUS must include multiple other effects due to the fact that a real turbine is not a simple nozzle: the flow deviation in the azimuthal direction generated by both stator and rotor stages is not negligible and cannot be taken into account when considering a 1D nozzle. Rotation effects should also be included to account for enthalpy jumps. To account for these effects, a 2D configuration is considered and the steady flow upstream

and downstream from each blade row is assumed to be uniform. Figure 5.1 shows a sketch of the configuration used for this study: an infinitely thin blade row acts as an interface between two regions of uniform flow. Vector **w** represents the mean flow velocity (with modulus w and an angle θ with the axial direction), and **k** is the wave vector: the direction of propagation of the considered wave (similarly with modulus k and angle ν).

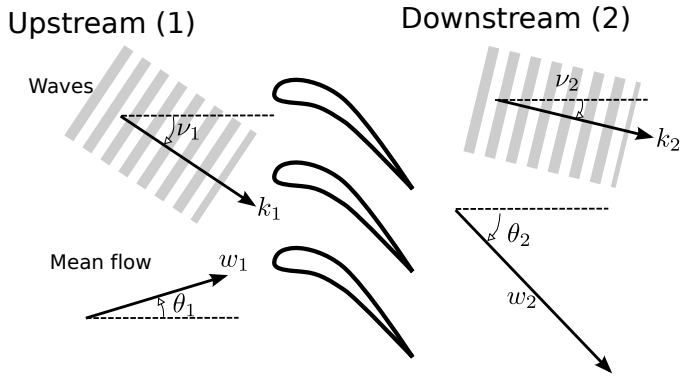

Figure 5.1 – *Sketch of the studied configuration.*

The flow is described using four variables: the modulus of the steady velocity w, its angle θ, the mean pressure p and the mean density of the flow ρ. The mean flow is perturbed by small fluctuations, which can be described with four primitive variables: the entropy perturbation s', the mean speed perturbation w', the pressure fluctuation p' and the perturbation on the mean flow angle θ'.

To begin with, the analytical method in the compact limit studies the propagation of waves in the upstream and downstream regions of the blade row, where the flow is considered steady and homogeneous. The acoustic, entropy and vorticity waves are related in this way with the primitive dimensionless fluctuating variables s'/c_p, w'/c, $p'/\gamma p$ and θ'. In the second step, the closure equations at the interfaces between the upstream and downstream regions of the turbine blades are obtained using the compact assumption, yielding four matching conditions relating both regions. In this way four equations are obtained relating the known incoming waves (generated in the combustion chamber for example) with the unknown outgoing waves: direct and indirect combustion noise at the outlet of the turbine.

5.2 Wave decomposition

To relate the fluctuating primitive variables with the waves propagating through the flow, the 2D linearised Euler equations (LEE) in a steady uniform flow are written, following Cumpsty and Marble (1977). These equations are obtained by linearising the 2D Euler equations about a mean steady homogeneous flow, and therefore they are limited to the inter-blades region only. They read

$$\frac{D}{Dt}\left(\frac{\rho'}{\rho}\right) + \frac{\partial u'}{\partial x} + \frac{\partial v'}{\partial y} = 0, \tag{5.1a}$$

$$\frac{D}{Dt}(u') = -\frac{1}{\rho}\frac{\partial p'}{\partial x}, \tag{5.1b}$$

$$\frac{D}{Dt}(v') = -\frac{1}{\rho}\frac{\partial p'}{\partial y}, \tag{5.1c}$$

$$\frac{D}{Dt}\left(\frac{s'}{c_p}\right) = \frac{D}{Dt}\left(\frac{p'}{\gamma p} - \frac{\rho'}{\rho}\right) = 0, \tag{5.1d}$$

where the material derivative

$$\frac{D}{Dt} = \frac{\partial}{\partial t} + \mathbf{w}\cdot\nabla = \frac{\partial}{\partial t} + u\frac{\partial}{\partial x} + v\frac{\partial}{\partial y} \tag{5.2}$$

is used, with $u = w\cos\theta$ and $v = w\sin\theta$ the axial and circumferential components of the mean velocity. The fluctuating variables u' and v' are the velocity perturbations in the x and y directions respectively. They can be related to w' and θ' using simple trigonometric relations,

$$\frac{u'}{u} = \frac{w'}{w} - \theta'\tan\theta, \qquad \frac{v'}{v} = \frac{w'}{w} + \theta'/\tan\theta. \tag{5.3}$$

The system of equations given in (5.1) describes the propagation of waves in a homogeneous steady two-dimensional flow. Any wave ϕ (acoustic, entropy or vorticity) can be written as

$$w^{\phi} = A_{\phi}\exp[-i(\omega t - \mathbf{k}_{\phi}\cdot\mathbf{x})], \tag{5.4}$$

where A_{ϕ} represents the amplitude, ω the angular frequency, $\mathbf{x}$ the vector in the fixed reference frame, t the time and $\mathbf{k}_{\phi}$ the wave vector, which can be expressed as a combination of the axial and circumferential components,

$$\mathbf{k}_{\phi}\cdot\mathbf{x} = k_{\phi,x}x + k_{\phi,y}y, \quad \text{with} \quad k_{\phi,x} = k_{\phi}\cos\nu_{\phi} \quad \text{and} \quad k_{\phi,y} = k_{\phi}\sin\nu_{\phi}. \tag{5.5}$$

Here, ν is the angle of the propagating wave, and k the modulus of the wave vector $\mathbf{k}$, as shown in figure 5.1. For simplicity, the wave vector will be scaled using the mean sound speed and the frequency, giving the dimensionless wave vector, $\mathbf{K} = \mathbf{k}c/\omega$ (with c the mean sound speed). When considering Marble and Candel (1977), note that when the wave propagates through the turbine stages it conserves its frequency and the circumferential component of the wave vector, k_y, related to the azimuthal mode number, m, through $k_y = m/R$, where R is the mean radius of the meridian plane of the turbine. This is not the case for the dimensionless circumferential component of the wave vector as the mean sound speed does change through blade rows.

Equations (5.1) can be used to relate, for each wave, the wave vector ($\mathbf{k}$) with the angular frequency (ω), the mean Mach number and flow direction (M and θ).

5.2.1 Entropy wave

The entropy wave, $w^s = s'/c_p$, can be written in the form

$$w^s = \frac{s'}{c_p} = A_s \exp[-i(\omega t - \mathbf{k}_s \cdot \mathbf{x})]. \tag{5.6}$$

The dispersion equation is obtained combining equation (5.6) with the propagation equation of the entropy wave, (5.1d). It reads

$$K_s M \cos(\nu_s - \theta) - 1 = 0. \tag{5.7}$$

This dispersion equation is used to obtain the axial component of the wave vector ($K_{s,x}$, related to the propagation speed), as a function of the circumferential component, the frequency and the mean flow Mach number and direction.

By definition, the entropy wave does not generate pressure or velocity perturbations and therefore the fluctuation of primitive variables (s'/Cp,

w'/c, $p'/\gamma p$ and θ') generated by the entropy wave are

$$\left\{\begin{array}{c} s'/c_p \\ w'/c \\ p'/\gamma p \\ \theta' \end{array}\right\}_s = \left\{\begin{array}{c} 1 \\ 0 \\ 0 \\ 0 \end{array}\right\} w^s. \tag{5.8}$$

5.2.2 Vorticity wave

The vorticity wave is written as

$$\xi' = \frac{\partial v'}{\partial x} - \frac{\partial u'}{\partial y}. \tag{5.9}$$

The propagating equation for the vorticity wave can be deduced from equations (5.1b) and (5.1c). Deriving (5.1b) with respect to y, and (5.1c) with respect to x leads to

$$\begin{aligned} \frac{\partial}{\partial y}\left(\frac{D}{Dt}(u')\right) &= -\frac{1}{\rho}\frac{\partial^2 p'}{\partial x \partial y}, \\ \frac{\partial}{\partial x}\left(\frac{D}{Dt}(v')\right) &= -\frac{1}{\rho}\frac{\partial^2 p'}{\partial y \partial x}. \end{aligned} \tag{5.10}$$

Subtracting both relations and using Schwartz's theorem, the pressure term is eliminated, leading to the vorticity equation

$$\frac{D}{Dt}\left(\xi'\right) = 0. \tag{5.11}$$

As done with the entropy wave, the vorticity wave is written in the form,

$$w^v = \frac{\xi'}{\omega} = A_v \exp[-i(\omega t - \mathbf{k}_v \cdot \mathbf{x})] \tag{5.12}$$

and by combining (5.11) and (5.12), the dispersion equation of the vorticity wave is obtained, namely

$$K_v M \cos\left(\nu_v - \theta\right) - 1 = 0. \tag{5.13}$$

Up to first order, no pressure or entropy fluctuations are associated with this wave. Using (5.1d) it can be proved that there are no density fluctuations either. Equation (5.1a) can be reduced to

$$\frac{\partial u'}{\partial x} + \frac{\partial v'}{\partial y} = 0 \tag{5.14}$$

and by using (5.12), the resulting velocity field can be written as

$$\begin{aligned} \frac{u'}{c} &= -i\frac{\xi'}{\omega}\frac{\sin(\nu_v)}{K_v}, \\ \frac{v'}{c} &= i\frac{\xi'}{\omega}\frac{\cos(\nu_v)}{K_v}. \end{aligned} \tag{5.15}$$

With equation (5.3), these fluctuations are recast in terms of w' and θ', namely

$$\begin{aligned} \frac{w'}{c} &= -i\frac{\xi'}{\omega}\frac{\sin(\nu_v - \theta)}{K_v}, \\ \theta' &= i\frac{\xi'}{\omega}\frac{\cos(\nu_v - \theta)}{MK_v}. \end{aligned} \tag{5.16}$$

Using the non-dimensional form of the vorticity wave, $w^v = \xi'/\omega$, the fluctuations of the primitive variables generated by this wave are

$$\left\{ \begin{array}{c} s'/c_p \\ w'/c \\ p'/\gamma p \\ \theta' \end{array} \right\}_v = \left\{ \begin{array}{c} 0 \\ -i\dfrac{\sin(\nu_v - \theta)}{K_v} \\ 0 \\ i\dfrac{\cos(\nu_v - \theta)}{MK_v} \end{array} \right\} w^v. \tag{5.17}$$

5.2.3 Acoustic waves

A propagating equation for pressure fluctuations can be obtained by combining equations (5.1a)-(5.1d): (5.1d) is first used to eliminate the density term of (5.1a) and the total derivative of the resulting equation is taken,

$$\left[\left(\frac{D}{Dt}\right)^2\right]\left(\frac{p'}{\gamma p}\right) + \frac{D}{Dt}\left(\frac{\partial u'}{\partial x}\right) + \frac{D}{Dt}\left(\frac{\partial v'}{\partial y}\right) = 0. \tag{5.18}$$

Combining (5.18) with the total derivative of (5.1b) and (5.1c), and knowing that $c^2 = \gamma p/\rho$, the propagating equation for the pressure perturbations reads

$$\left[\left(\frac{D}{Dt}\right)^2 - c^2\left(\frac{\partial^2}{\partial x^2} + \frac{\partial^2}{\partial y^2}\right)\right]\left(\frac{p'}{\gamma p}\right) = 0. \tag{5.19}$$

Using the waveform of equation (5.4) for the acoustic wave,

$$w^{\pm} = \left(\frac{p'}{\gamma p}\right)_{\pm} = A_{\pm}\exp[-i(\omega t - \mathbf{k}_{\pm}\cdot\mathbf{x})], \tag{5.20}$$

the dispersion equation follows,

$$\left(1 - K_{\pm}M\cos\left(\nu_{\pm} - \theta\right)\right)^2 - K_{\pm}^2 = 0, \tag{5.21}$$

where $K_{\pm}$ is the modulus of the non-dimensional wave vector. As the acoustic dispersion equation has two solutions, the subscript $(\pm)$ stands for the acoustic perturbation propagating downstream $(+)$ and upstream $(-)$. The equation can be written as a function of the axial and circumferential components ($K_{\pm,x}$ and $K_{\pm,y}$) using (5.5),

$$\left(1 - K_{\pm,x}M\cos\theta - K_{\pm,y}M\sin\theta\right)^2 - K_{\pm,x}^2 - K_{\pm,y}^2 = 0. \tag{5.22}$$

When solving for (5.22), $K_{\pm,x}$ can be either a real or a complex value. The real values are acoustic waves propagating without attenuation through the mean steady flow. On the other hand, complex values correspond to evanescent waves that cannot propagate in the considered flow. Solving for (5.22) yields the condition

$$\left(1 - K_{\pm,y}M\sin\theta\right)^2 - \left(1 - M^2\sin^2\theta\right)K_{\pm,y}^2 < 0, \tag{5.23}$$

which gives two critical values for the dimensionless azimuthal component of the wave vector,

$$K_{\pm,y} = M\sin\theta \pm \sqrt{M^2\sin^2\theta + 1}. \tag{5.24}$$

For a given mean flow, this relation gives a critical value of $K_{\pm,y} = ck_{\pm,y}/\omega$. This shows that for any circumferential acoustic mode $k_{\pm,y}$, there exists a cut-off frequency below which the acoustic waves will not propagate.

The fluctuation of primitive variables generated by the wave can be obtained from (5.1a)-(5.1d), knowing that the wave is isentropic and irrotational, and reads

$$\left\{\begin{array}{c} s'/c_p \\ w'/c \\ p'/\gamma p \\ \theta' \end{array}\right\}_{\pm} = \left\{\begin{array}{c} 0 \\ K_{\pm}\cos\left(\nu_{\pm}-\theta\right)/\left[1-K_{\pm}M\cos\left(\nu_{\pm}-\theta\right)\right] \\ 1 \\ K_{\pm}\sin\left(\nu_{\pm}-\theta\right)/\left[M\left(1-K_{\pm}M\cos\left(\nu_{\pm}-\theta\right)\right)\right] \end{array}\right\} w^{\pm}. \quad (5.25)$$

The primitive fluctuating variables are written as a function of the four waves in a matrix form by adding the contribution of each wave, namely

$$\left\{\begin{array}{c} s'/c_p \\ w'/c \\ p'/\gamma p \\ \theta' \end{array}\right\} = [\mathcal{M}]\cdot\left\{\begin{array}{c} w^{s} \\ w^{v} \\ w^{+} \\ w^{-} \end{array}\right\}, \quad (5.26)$$

where matrix $[\mathcal{M}]$ is given by the combination of equations (5.8), (5.17) and (5.25), and follows

$$[\mathcal{M}] = \begin{bmatrix} 1 & 0 & 0 & 0 \\ 0 & -i\dfrac{\sin\left(\nu_v-\theta\right)}{K_v} & \dfrac{K_{+}\cos\left(\nu_{+}-\theta\right)}{\left(1-K_{+}M\cos\left(\nu_{+}-\theta\right)\right)} & \dfrac{K_{-}\cos\left(\nu_{-}-\theta\right)}{\left(1-K_{-}M\cos\left(\nu_{-}-\theta\right)\right)} \\ 0 & 0 & 1 & 1 \\ 0 & i\dfrac{\cos\left(\nu_v-\theta\right)}{K_v M} & \dfrac{K_{+}\sin\left(\nu_{+}-\theta\right)}{M\left(1-K_{+}M\cos\left(\nu_{+}-\theta\right)\right)} & \dfrac{K_{-}\sin\left(\nu_{-}-\theta\right)}{M\left(1-K_{-}M\cos\left(\nu_{-}-\theta\right)\right)} \end{bmatrix}. \quad (5.27)$$

5.3 Jump conditions through the blade row

Once the primitive variables are related to the acoustic, entropy and vorticity waves through equation (5.27), both at the upstream and downstream regions of a blade, only a relation between the primitive variables at both sides is needed to completely define the problem. Since the blade row is

assumed to be axially compact, the upstream and downstream flows can be related through a jump condition. As shown in equation (5.26), four equations are needed to relate the waves on both sides of the blade row. These conditions are obtained using the conservation of mass, energy and entropy fluctuations, plus a fourth equation on the circumferential component of the flow, obtained through the Kutta condition. Since energy is not conserved through rotating blades, the study of the stator vane and of the rotor blade must be done separately.

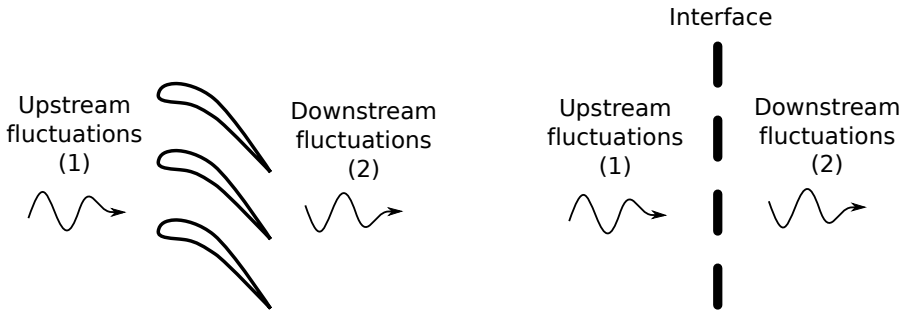

(a) Real configuration (b) Modelled configuration

Figure 5.2 – *Sketch of the jump conditions using the compact blade assumption.*

5.3.1 Stator vane

For the stator vane, the conservation equations of mass, total temperature and entropy fluctuations, used by Cumpsty and Marble (1977), read

$$\begin{aligned}
\left(\frac{\dot{m}'}{\dot{m}}\right)_1 &= \left(\frac{\dot{m}'}{\dot{m}}\right)_2, \\
\left(\frac{T_t'}{T_t}\right)_1 &= \left(\frac{T_t'}{T_t}\right)_2, \\
\left(\frac{s'}{c_p}\right)_1 &= \left(\frac{s'}{c_p}\right)_2.
\end{aligned} \tag{5.28}$$

Subscripts 1 and 2 represent the flows upstream and downstream of the blade row as shown in figure 5.1. These equations should be written as a function of the primitive variables used previously (s', p', w' and θ'). For

the mass and temperature fluctuations this gives

$$\left(\frac{\dot{m}'}{\dot{m}}\right) = \frac{p'}{\gamma p} + \frac{1}{M}\frac{w'}{c} - \theta' \tan\theta, \tag{5.29}$$

$$\left(\frac{T_t'}{T_t}\right) = \frac{1}{1 + \dfrac{(\gamma-1)}{2}M^2}\left[(\gamma-1)\frac{p'}{\gamma p} + \frac{s'}{c_p} + (\gamma-1)M\frac{w'}{c}\right]. \tag{5.30}$$

These equations should be completed with a fourth condition. Cumpsty and Marble (1977) used the Kutta condition at the outlet of the blade. In the potential-flow theory the Kutta condition proposes that, in the steady flow around an airfoil, the effect of viscosity is incorporated by a single condition imposed to remove the trailing-edge velocity singularity in the solution. This condition fixes the circulation around the airfoil such that the rear stagnation point is located at the trailing-edge. For unsteady flows, the Kutta condition used by Cumpsty and Marble (1977) states that the flow deviation, θ_2, is equal to the geometrical angle of the trailing edge, and therefore it's perturbation should be zero ($\theta_2' = 0$). Imposing the correct condition at the trailing edge of the blade row is of great importance for correctly predicting the generation of noise by the trailing edge and, in our case, the acoustic transfer functions of the stator blade. Cumpsty and Marble (1977) suggest using a more general form of the Kutta condition, given by

$$\theta_2' = \beta\theta_1', \tag{5.31}$$

where β is measured when experimental data is available or calculated through semi-empirical methods. In the limit of low frequencies used in this context, the Kutta condition with $\beta = 0$ is generally valid as the flow evolves quasi-steadily.

Using equations. (5.28) and (5.31), and writing them as a function of the primitive variables using (5.29)-(5.30), the jump conditions are obtained, and may be written in a matrix form for simplicity, giving

$$[\mathcal{E}_1]\cdot\begin{Bmatrix} s'/c_p \\ w'/c \\ p'/\gamma p \\ \theta' \end{Bmatrix}_1 = [\mathcal{E}_2]\cdot\begin{Bmatrix} s'/c_p \\ w'/c \\ p'/\gamma p \\ \theta' \end{Bmatrix}_2, \tag{5.32}$$

with $[\mathcal{E}_1]$ and $[\mathcal{E}_2]$ defined as,

$$[\mathcal{E}_1] = \begin{bmatrix} 1 & 0 & 0 & 0 \\ -1 & \frac{1}{M_1} & 1 & -\tan\theta_1 \\ \frac{\mu_1}{\gamma-1} & \mu_1 M_1 & \mu_1 & 0 \\ 0 & 0 & 0 & \beta \end{bmatrix},$$

$$[\mathcal{E}_2] = \begin{bmatrix} 1 & 0 & 0 & 0 \\ -1 & \frac{1}{M_2} & 1 & -\tan\theta_2 \\ \frac{\mu_2}{\gamma-1} & \mu_2 M_2 & \mu_2 & 0 \\ 0 & 0 & 0 & 1 \end{bmatrix}, \tag{5.33}$$

where $\mu = 1/[1 + (\gamma - 1)M^2/2]$ is used for simplicity.

5.3.2 Rotor blade

For the rotor blade, the conservation of total enthalpy used in Section 5.3.1 is no longer verified. Instead, the rothalpy can be used as a conserved variable throughout the turbomachine. The rothalpy is defined as

$$I = h_t - Uv, \tag{5.34}$$

where h_t is the specific total enthalpy, U is the rotating speed of the blade and v the circumferential component of the absolute speed, as seen in figure 5.3. For the rotating speed, a different value will be considered at the inlet and outlet for the sake of generality, though in most high-pressure axial turbines, $U_1 = U_2$. The conservation of rothalpy can be easily shown using the energy equation and the Euler equation for turbomachines, namely

$$\Delta h_t = \tau, \quad \text{and} \quad \tau = \Delta(Uv) = U_2 \cdot v_2 - U_1 \cdot v_1. \tag{5.35}$$

Considering small perturbations, a generalised form of the energy equation can be written as

$$\frac{I_1'}{I_1} = \frac{I_2'}{I_2}, \tag{5.36}$$

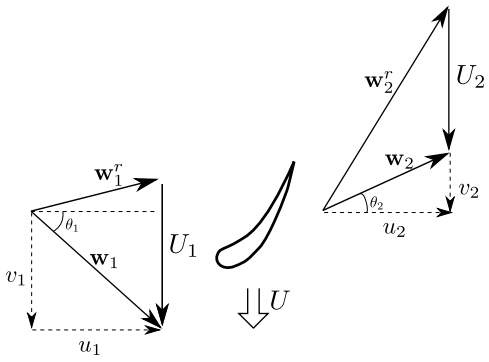

Figure 5.3 – *Sketch of the flow through a rotor blade. Superscript* $(\,)^r$ *represents the variables in the rotor reference frame.*

which substitutes the relation given in equation (5.28) for the total temperature jump. The rothalpy fluctuation is written as a function of the primitive variables

$$\frac{I'}{I} = \frac{h_t' - Uv'}{h_t - Uv} = \frac{\dfrac{h_t'}{h_t} - \dfrac{Uv}{h_t}\dfrac{v'}{v}}{1 - \dfrac{Uv}{h_t}}. \tag{5.37}$$

Knowing that $h_t = c_p T_t$ and defining the parameter ζ as

$$\zeta = \frac{Uv}{h_t}, \tag{5.38}$$

equation (5.37) can be re-written as

$$\frac{I'}{I} = \frac{1}{1-\zeta}\left[\frac{T_t'}{T_t} - \zeta\left(\frac{v'}{v}\right)\right]. \tag{5.39}$$

It can be seen from equation (5.38) that for $U = 0$, ζ is found to be zero, and the conservation of the total temperature used for the stator is recovered. Equation (5.36) therefore replaces the second equation of (5.28) when considering rotating blades. The fluctuating circumferential velocity, v'/v, can be eliminated using (5.3), giving finally

$$\frac{I'}{I} = \frac{1}{1-\zeta}\left[\frac{T_t'}{T_t} - \zeta\left(\frac{1}{M}\frac{w'}{c} + \frac{\theta'}{\tan\theta}\right)\right], \tag{5.40}$$

and used to replace the energy equation in (5.33).

For the rotor, the Kutta condition must be imposed in its reference frame, leading to

$$\left(\theta'\right)_2^r = \beta\left(\theta'\right)_1^r, \tag{5.41}$$

where $(\theta')^r$ is the fluctuation of the direction of the relative velocity. Using this formulation, $\beta = 0$ imposes the Kutta condition where the flow deviation at the outlet of the rotor is fixed by the geometry. Note that this value of $\beta = 0$ is used here, in contrast to Duran and Moreau (2012) as the angle $(\theta')^r$ is considered in the relative frame. The above condition can be re-written as a function of the fixed reference-frame variables, using figure 5.3 and simple trigonometric relations, namely as

$$(\theta')^r = \theta' \left(1 + \frac{U}{w^r}\right) + \frac{w'}{w}\frac{U}{w^r}. \tag{5.42}$$

The jump conditions for the rotor case are written in a matrix form similar to equations (5.32) and (5.33).

5.4 Solution of the equations and boundary conditions

The matrix system is used to solve the problem imposing the correct boundary conditions. These are, in the subsonic case, w^+, w^s and w^v at the inlet, and w^- at the outlet of the blade row. The waves coming from the combustion chamber must first be decomposed by modes, related to k_y, and by frequencies ω. The propagation equations are solved for each pair (k_y, ω) for which the dispersion equations can be used to obtain the value of the complete wave vector, $\mathbf{K}$, at both sides of the blade row for each wave. Using this information, matrix $\mathcal{M}$ and $\mathcal{E}$ can then be calculated on both sides of the blade row.

For a single row the problem is solved by writing (5.32) as a function of the waves (using (5.26)),

$$\underbrace{[\mathcal{E}_u]\cdot[\mathcal{M}_u]}_{[\mathcal{B}_u]}\cdot\mathbf{W}_u = \underbrace{[\mathcal{E}_d]\cdot[\mathcal{M}_d]}_{[\mathcal{B}_d]}\cdot\mathbf{W}_2, \tag{5.43}$$

between the upstream (u) and downstream regions of the blade, where $\mathbf{W}_u = [w^s, w^v, w^+, w^-]_u$ and similarly for $\mathbf{W}_d$.

The boundary conditions for the problem must impose only the incoming waves at each boundary, but the upstream-propagating acoustic wave must

be imposed at the outlet while the downstream-propagating acoustic wave, the entropy and vorticity waves are imposed at the inlet of the turbine stage. For this reason, the fourth column of matrices $[\mathcal{B}_1]$ and $[\mathcal{B}_2]$ should be permuted (and changed signs) in order to have a matrix system with the imposed waves on the right-hand side of the equations and the unknowns on the left-hand side. The resulting matrices, named $[\mathcal{A}_{in}]$ and $[\mathcal{A}_{out}]$ give the system of equations

$$[\mathcal{A}_{out}] \cdot \widetilde{\mathbf{W}}_{out} = [\mathcal{A}_{in}] \cdot \widetilde{\mathbf{W}}_{in}, \tag{5.44}$$

where $\widetilde{\mathbf{W}}_{in} = \left[w_u^s, w_u^v, w_u^+, w_d^-\right]$ is the incoming wave vector (known) and $\widetilde{\mathbf{W}}_{out} = \left[w_d^s, w_d^v, w_d^+, w_u^-\right]$ the outgoing wave vector (unknown). This system of equations can be inverted to obtain the outgoing waves.

For the case of multiple blade rows, the phase-shift of the waves through the blade-row spacing is taken into account. This is done using the matrix $[\mathcal{T}]$, in which the diagonal terms are the phase-shift of the waves, namely

$$[\mathcal{T}_2] = \begin{bmatrix} \exp\left(ik_x^s L\right) & 0 & 0 & 0 \\ 0 & \exp\left(ik_x^v L\right) & 0 & 0 \\ 0 & & \exp\left(ik_x^+ L\right) & 0 \\ 0 & 0 & 0 & \exp\left(ik_x^- L\right) \end{bmatrix}, \tag{5.45}$$

where L is the distance between rows. Considering $\mathbf{W}_u^i$ and $\mathbf{W}_d^i$, the vector of waves upstream and downstream of the *i-th* blade row. Equation (5.43) relates both sides through

$$\left[\mathcal{B}_1^i\right] \cdot \mathbf{W}_u^i = \left[\mathcal{B}_2^i\right] \cdot \mathbf{W}_d^i. \tag{5.46}$$

The downstream vector of waves can be related to the following blade row through $\mathbf{W}_u^{i+1} = [\mathcal{T}^i] \cdot \mathbf{W}_d^i$. Combining the successive stages of the turbine, a relation between the inlet and the outlet waves of the turbomachine can be written in a matrix form, giving

$$\left[\prod_{i=1}^{N_r-1} \left\{\left[\mathcal{B}_1^{i+1}\right] \mathcal{T}^i \left[\mathcal{B}_2^i\right]^{-1}\right\}\right] \left[\mathcal{B}_1^1\right] \cdot \mathbf{W}_u^1 = \left[\mathcal{B}_2^{N_r}\right] \cdot \mathbf{W}_d^{N_r}, \tag{5.47}$$

where N_r is the number of rows. The system of equations can finally be permuted as before to obtain a system of equations as in (5.44), which can be inverted to obtain the outgoing waves,

$$\widetilde{\mathbf{W}}_{out} = [\mathcal{A}_{out}]^{-1} [\mathcal{A}_{in}] \cdot \widetilde{\mathbf{W}}_{in}. \tag{5.48}$$

The combination of several blade rows leads to a transfer function which is frequency dependent due to the phase-shift of (5.45), even if the compact assumption is being made for each individual blade. The result is therefore still limited to low frequencies.

Note that when the parameter of the Kutta condition β is equal to zero, the system of equations is singular and cannot be inverted. In practice, hereafter the condition is relaxed by using a small value, $\beta = 10^{-9}$ for both the stator and the rotor blades.

Chapter 6

Numerical simulations of waves propagating through turbine blades

The analytical method proposed in Chapter 5 is still based on strong assumptions. Firstly, the stator and rotor blades are considered a discontinuity in the flow, and therefore the compact assumption is made. As seen in Part I the response of a nozzle at non-zero frequencies can differ strongly from the compact response, and this may also be the case too for the 2D flow. The difference in the 2D model is that the turbine stage is modelled by considering the succession of compact stator and rotor blades, but a non-compact propagation of waves through the region in between the blades.

In Part III we will use this analytical method in a real engine, but before this stage, it is useful to verify its accuracy. This step is extremely difficult experimentally but it can be done numerically by comparing the analytical model with a numerical simulation of waves propagating through a stator rotor system using AVBP (Schønfeld and Rudgyard, 1999). Therefore the objective of the numerical simulations described in this chapter is to obtain the real transfer functions of a turbine stage, in order to compare it with the analytical method and evaluate the possible errors made. The case of a single stator blade has already been studied by Leyko et al. (2010, 2013); Zhao et al. (2012); Mishra and Bodony (2013). In this work, we will therefore focus first on the rotor case before studying the stator-rotor configuration, where the extension of the theory to rotating blades is analysed and the

effect of the combination of successive turbine rows can be seen.

Such a simulation involves a very large range of characteristic time scales, as explained by Leyko et al. (2010): on the one hand, the small details of the turbulent flow should be resolved, and on the other hand, the frequency of the acoustic and entropy perturbations must be small enough. For this reason, the analysis is performed in a 2D configuration, shown in figure 6.1 for the case of the stator-rotor case. This has two main implications: firstly, the flow is considered 2D and therefore no realistic turbulent mixing is computed as the large 2D structures generated at the trailing edge of the blades cannot develop into fine 3D turbulence; secondly, only longitudinal plane waves with no circumferential component can be studied as the computation is limited to one stator-rotor using periodic boundary conditions. This configuration could be seen to be representative of HP turbines with small spans, neglecting hub and tip clearance effects.

In all cases, such an exercise requires propagating waves through moving obstacles (the blades), a CFD task which requires significant attention. This was done in AVBP and the corresponding methods are described in Section 6.1. Results for the rotor stage submitted to acoustic and entropy waves are described in Section 6.2 and a stator-rotor configuration is considered in Section 6.3. For all cases, the reflected and transmitted waves are measured in AVBP for all frequencies and compared to the analytical model of Chapter 5. Note that a by-product of this study is that, since multiple methods were also used for the simulation of the moving parts of the stages, a comparison between ALE and a new movement-grid technique will also be made.

6.1 Numerical methods

The AVBP code (Schønfeld and Rudgyard, 1999) is used to compute the 2D flow first through a single rotor blade, followed by a complete turbine stage (stator-rotor). The Smagorinski sub-grid turbulence model is used for stability purposes and not to model turbulence, and the laminar and turbulent Prandtl numbers are kept high to reduce heat diffusion and isolate this effect from the transmission problem addressed in this thesis. All simulations are performed using the TTG4A numerical scheme, which is third order in space and fourth order in time. The mesh grid is fine enough ($\Delta x_{max} \approx 1$ mm) to

correctly solve all the frequencies of interest: f_{max} = 5000 Hz, corresponding to an acoustic wavelength of $\lambda_{ac} \approx 160$ mm and an entropy wavelength of $\lambda_{en} \approx 26$ mm.

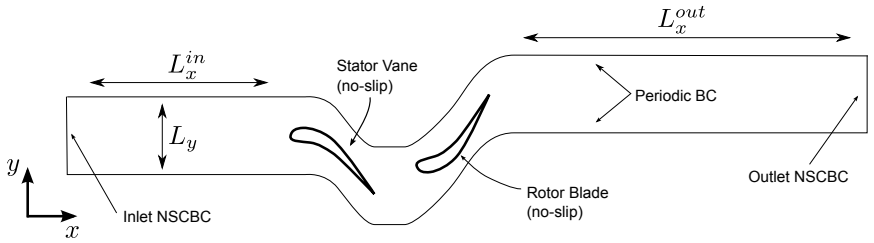

Figure 6.1 – *Sketch of the computational domain of the stator-rotor configuration.* L_y = 50 *mm,* L_x^{in} = 150 *mm and* L_x^{out} = 450 *mm.*

6.1.1 Numerical methods for rotation

In order to compute the flow on a moving mesh and the wave propagation two different approaches are used: the ALE formulation (Method A) and the MISCOG coupling (Method B). The ability of both methods to correctly compute the propagation of waves through turbine stages will be compared and validated. A third method will be used for the single rotor blade as no relative displacement exists. In this third method (Method C), the complete computational domain is translated at the blade speed and no mesh deformation exists.

Method A: ALE method

The rotation of the blade is imposed using the Arbitrary Lagrangian-Eulerian (ALE) method (Noh, 1964; Hirt et al., 1974; Moureau et al., 2004), where the mesh nodes may be moved with an imposed velocity given by an analytical expression. The velocity of the rotor, U = 500 m/s, is imposed in the central region of the domain shown in figure 6.2, the inlet and outlet regions remaining fixed. In two regions immediately upstream and downstream of the rotor blade (shaded regions in figure 6.2) the grid is deformed with a linear velocity matching both sides, going from U to zero. The mesh is deformed due to the deformation velocity gradient, as shown in figure 6.3. The angle of the deformation, ς, can be approximated as

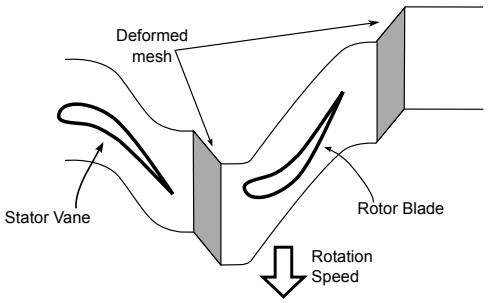

Figure 6.2 – *Sketch of the stator-rotor showing the moving region and the deformed mesh for the ALE method.*

$$\varsigma \approx \frac{dU}{dx}\Delta t. \tag{6.1}$$

The deformation of the mesh is therefore smaller when the gradient is smaller, but this means that the deformation region should be larger, and this distance is limited by the presence of the stator upstream. In practice, the deformed region is 15 mm long, giving a deformation velocity gradient of $dU/dt \approx 33000$ s^{-1}. When the mesh deformation is too strong, the computation must be stopped and the solution interpolated on a new mesh, a procedure which is standard in AVBP for piston engine computations (Granet et al., 2010). Interpolation between five different meshes at five different relative positions of the rotor blade ensures an acceptable mesh quality throughout the whole simulation, with a maximum value of $\varsigma < 19°$. Figure 6.4 shows the deformation of the mesh for the stator-rotor simulation.

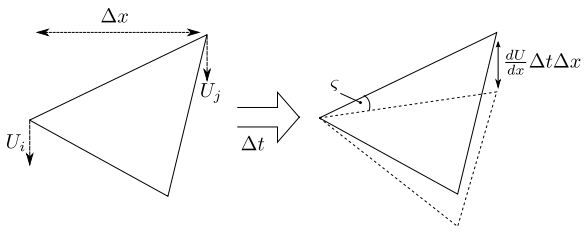

Figure 6.3 – *Analysis of the mesh deformation for the ALE method.*

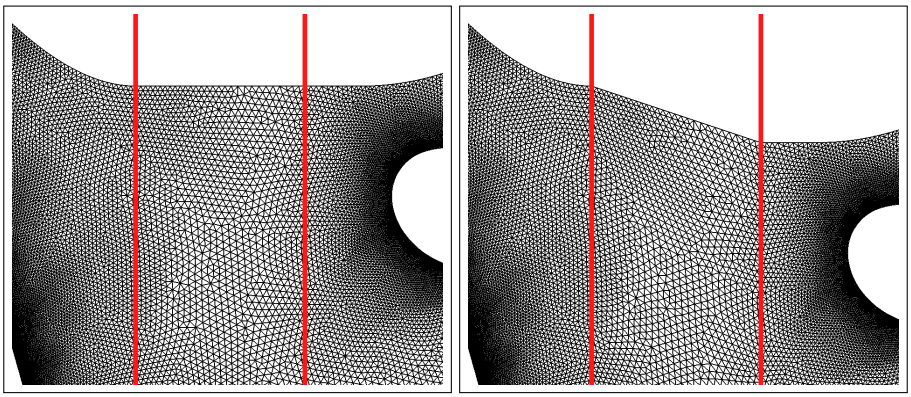

(a) Mesh before deformation (b) Maximum deformation

Figure 6.4 – *Detail of the mesh deformation of figure 6.2 for the region between the stator and the rotor blades. Two vertical lines delimit the deformed region.*

Method B: MISCOG method

The mesh deformation induced by the ALE approach can be detrimental to accuracy and efficiency. Another method for moving grids, introduced by Wang et al. (2013) has therefore been tested. In this method, called MISCOG (Multi Instances Solver Coupled via Overlapping Grids) the stator and rotor are simulated separately in two separate instances of AVBP and coupled at the interface using Open-PALM (Buis et al., 2006) through an interpolation of the nodes in the overlapped region, as shown in figure 6.5. The number of nodes in the overlapping region where the interpolation is performed is such as to verify the stability criteria, which depends on the order of the discretisation scheme used, as explained by Wang et al. (2013). This method has been shown to correctly propagate both acoustic and hydrodynamic perturbations through the interface with little dissipation or numerical errors.

Method C: No-deformation method

For the rotor case only, the solution can be computed with no mesh deformation as no relative displacement between blades exists. In this method the complete computational domain is translated at the blade speed (with no deformation of the mesh). The method can be considered as the ALE method applied to a single rotor blade, where the velocity U = 500 m/s is

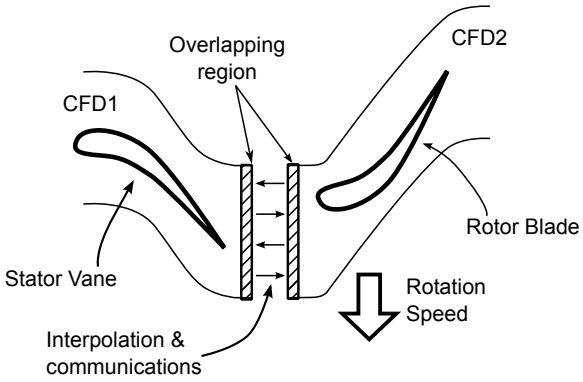

Figure 6.5 – *Sketch of the interface between the two simulations: CFD1 and CFD2 for the MISCOG method.*

Method \ Case	Rotor blade	Stator-rotor
ALE	x	x
MISCOG	x	x
No-deformation	x	

Table 6.1 – *Combination of the two cases and the three methods used. 'x' indicates the simulation performed.*

prescribed in the complete computational domain and no interpolation is therefore required.

Table 6.1 shows the simulations performed to compute first the single rotor blade, followed by the stator-rotor case.

6.1.2 Boundary conditions and forcing term

Boundary conditions are a key element to ensure a correct simulation, especially when dealing with acoustic problems. Figure 6.1 shows the boundary conditions used in the stator-rotor case. Periodicity is imposed at the top and bottom boundaries and a no-slip boundary condition is used for the stator and rotor walls, with a wall-model (high-Reynolds approach) used to impose the wall shear stress.

At the outlet boundary pressure is imposed using the NSCBC method developed by Poinsot and Lele (1992), in order to reduce the reflection of acoustic waves. In this method the acoustic wave entering the domain is written as

$$\frac{\partial w^-}{\partial t} - L^- = 0. \tag{6.2}$$

The value of L^- is imposed as a function of the difference between the local and the target pressure, multiplied by the relaxation parameter, namely

$$L^- = \kappa_p(p - p_{ref})/(\gamma p_{ref}), \tag{6.3}$$

where κ_p is the relaxation coefficient, given in s^{-1}, and p_{ref} the reference pressure. Large values of κ_p impose a reflecting boundary condition and low values a non-reflecting one. In practice $\kappa_p = 0$ cannot be used as the reflected wave would be set to zero and the outlet pressure may drift from the reference value. Intermediate values of κ_p prescribe a partially reflecting boundary. Selle et al. (2004) showed that this boundary condition is equivalent to a first-order low-pass filter,

$$R_{out} = \frac{-1}{1 - 2i\omega/\kappa_p}. \tag{6.4}$$

In figure 6.6, the reflection coefficient can be seen to be smaller than 5% of the incident wave when $\omega/\kappa_p > 10$. In practice, a modification of the

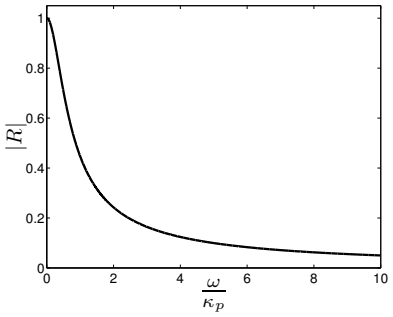

Figure 6.6 – *Reflection coefficient of the outlet boundary condition.*

NSCBC boundaries at the outlet, as done by Yoo et al. (2005) and Granet et al. (2010), is implemented to ensure that the vortices generated by the trailing edge of the blades are convected without generating noise.

The inlet boundary condition is treated in the same way but with the relaxation parameter as a function of velocity, namely

$$\frac{\partial w^+}{\partial t} - L^+ = 0, \quad \text{with} \quad L^+ = \kappa_u(u - u_{ref})/c \tag{6.5}$$

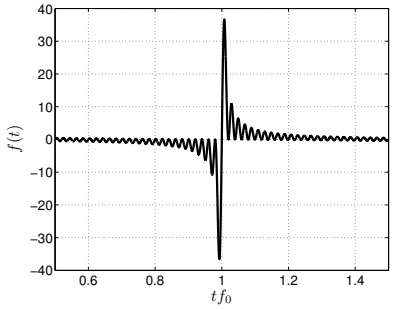

Figure 6.7 – *Function $f(t)$ used to pulse the boundary conditions plotted with $N = 50$.*

for the downstream propagating acoustic wave and

$$\frac{\partial w^s}{\partial t} - L^s = 0, \quad \text{with} \quad L^s = \kappa_T (T - T_{ref})/T_{ref} \tag{6.6}$$

for the entropy wave. The inlet reflection coefficient can be shown to have the same behaviour as the outlet boundary condition.

To calculate the acoustic and entropy transfer functions, the boundary conditions are forced starting from a statistically converged mean flow through the blade rows. Two separate simulations are therefore performed for each case: a first one in which an acoustic forcing term is introduced through the inlet boundary condition, and a second one in which the entropy wave is forced at the inlet. The acoustic forcing term at the boundary is described as,

$$w_f^+ = A^+ f(t), \quad \text{with} \quad f(t) = \sum_{k=1}^{N} sin(2\pi k f_0 t), \tag{6.7}$$

where A^+ is a sufficiently small amplitude such as to consider the response to be linear. The entropy forcing term reads,

$$w_f^s = A^s f(t). \tag{6.8}$$

Function $f(t)$ is composed of N frequencies in order to compute the transfer functions at several frequencies in a single simulation and is shown in figure 6.7 (Leyko et al., 2013). In this case $N = 50$ and the fundamental frequency chosen is $f_0 = 100$ Hz.

The use of function, $f(t)$, presents a major drawback as it presents a large peak value of 36.5. This means that the forcing wave $w_f^{+,s}$ (acoustic or

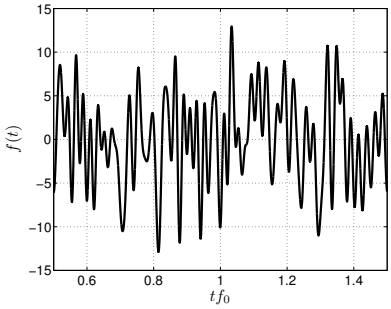

Figure 6.8 – *Function $f_r(t)$ used to pulse the boundary conditions plotted with $N = 50$.*

entropy) will have a maximum amplitude 36.5 times larger than the amplitude of the individual sinusoidal waves. Since the objective is to study the propagation of small amplitude waves, the maximum value of $w_f^{+,s}$ should be kept low to avoid non-linear effects. On the contrary, the amplitude of the waves should be large enough so that the waves introduced through the boundaries are larger than the noise generated by the rotor. For this reason, it is interesting to reduce the maximum value of $f(t)$ (and therefore of the signal $w_f^{+,s}$ without reducing the individual waves' amplitude $A^{+,s}$). To do so, a random phase-shift is added to the function,

$$f_r(t) = \sum_{k=1}^{N} sin(2\pi k f_0 t + 2\pi r_k), \tag{6.9}$$

where r_k is a random number between 0 and 1. The resulting function for a given set of random numbers is shown in figure 6.8, showing a peak value of 13. This function is used to allow a larger amplitude of the forced waves without causing a non-linear response. The Fourier transform of both functions $f(t)$ and $f_r(t)$ is, in both cases, a Dirac function at each of the considered frequencies, though for the case of $f_r(t)$ these Dirac functions present random phases. In the following, and unless stated otherwise, $f_r(t)$ will be used for the forcing term as it allows a larger amplitude of the forced waves and therefore a larger signal-to-noise ratio.

The forcing functions have to be imposed in the boundary condition through the NSCBC method. For the acoustic forcing, the L^+ term of equation. (6.5) is modified to add the contribution of the acoustic forcing wave,

$$L^+ = \kappa_u(u - u_{ref} - u_f^+)/(c_{ref}) + \partial w_f^+/\partial t. \tag{6.10}$$

In the above, the term $u_f^+ = c_{ref} w_f^+$ is the velocity perturbation generated by the forced acoustic wave, and is introduced so that the NSCBC method

does not try to suppress the velocity fluctuations induced by the injected wave. When the acoustic wave, w_f^+, is injected at the inlet, the temperature fluctuations generated by the acoustic wave, $T_f^+ = T_{ref} w_f^+ (\gamma - 1)/\gamma$, must be introduced in the term L^s,

$$L^s = \kappa_T (T - T_{ref} - T_f^+)/T_{ref}. \tag{6.11}$$

Failure to do so would lead to extra entropy waves generated at the same time, due to the NSCBC conditions trying to fix the temperature to the reference value T_{ref}.

The forcing of the entropy wave is done in the same way: The entropy wave L^s is modified to include the forcing term and the temperature fluctuations due to this forcing, T_f^s,

$$L^s = \kappa_T (T - T_{ref} - T_f^s)/T_{ref} + \partial w_f^s/\partial t, \tag{6.12}$$

and the acoustic equation is left unaltered as the entropy wave does not induce any velocity fluctuations,

$$L^+ = \kappa_u (u - u_{ref})/c_{ref}. \tag{6.13}$$

To avoid reflected waves at both boundaries the relaxation coefficients of the NSCBC boundaries are set to $\kappa = 10\ s^{-1}$, ensuring no drift of the mean flow and reducing the reflection of waves.

To ensure statistic convergence of the results, the simulation is run for 65 periods of the lowest frequency, where the first 5 periods are discarded and the remaining 60 used for post-processing of the signal.

6.1.3 Post-processing of the waves

Figure 6.9 shows the vorticity field of the stator-rotor case at an instant prior to the injection of the waves through the boundary condition. Though no turbulence is injected at the inlet, the no-slip condition at the stator and rotor generates a trailing-edge vortex shedding. These eddies are not real turbulence as they cannot stretch in the spanwise direction, and are most likely too large because of the 2D configuration of the study, but their presence perturbs the entropy and acoustic waves.

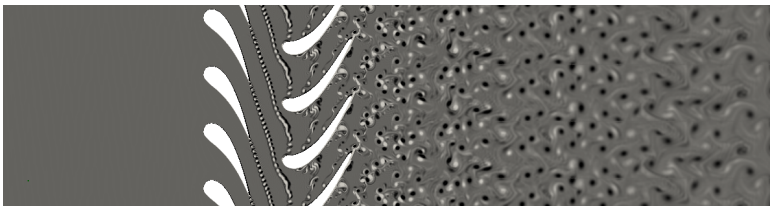

Figure 6.9 – *Vorticity field of the flow for the stator-rotor case.*

For this reason, post-processing is performed in the long inlet and outlet regions to calculate the transmitted and reflected waves for each simulation. The post-processing is performed in 5 steps, as done by Leyko et al. (2010) for a single stator blade:

1. **Steady state calculation:** The mean flow variables are calculated at the inlet and outlet.
2. **Wave calculation:** Primitive variables (s'/c_p, w'/c, $p'/\gamma p$ and θ') are calculated at each point as a function of time. Using matrix $[\mathbf{M}]$ given in equation. (5.27), the four waves w^s, w^v, w^+, w^- are calculated as a function of x, y and t, both at the inlet and outlet regions.
3. **Integration along the transverse direction:** The waves are averaged along the transverse direction through integration since only plane waves are considered in this study. For a wave ϕ,
$$w_x^\phi(x,t) = \frac{1}{L_y}\int_0^{L_y} w^\phi(x,y,t)dy. \tag{6.14}$$
4. **Fourier Transform:** The Fourier transform is performed at the discrete frequencies considered in (6.7):
$$\hat{w}_x^\phi(x,k) = \left|\frac{1}{t_f}\int_0^{t_f} w_x^\phi(x,t)\exp(2\pi \mathrm{i} f_0 k t)dt\right|. \tag{6.15}$$
5. **Integration along the propagating direction:** the Fourier transform is finally integrated along the x-axis to average the solution, giving
$$w^\phi(k) = \sqrt{\frac{1}{L_x}\int_0^{L_x}\left[\hat{w}_x^\phi(x,k)\exp(-2\pi \mathrm{i} f_0 k x/u_\phi)\right]^2 dx}. \tag{6.16}$$
where u_ϕ is the propagating velocity of the considered wave ($u+c$ and $u-c$ for the acoustic waves and u for the convective waves). The exponential term is included in order to average only the waves propagating with the correct speed.

	Rotor	
	Inlet	Outlet
Mach	0.653	0.366
θ	-75.76	-60
c [m/s]	774.3	767.6
γ	1.3	1.3
U [m/s]	-500	
Π	0.77	
$\psi = -\frac{\Delta h_t}{U^2}$	0.49	

Table 6.2 – *Mean flow characteristics through the rotor blade.*

6.2 Rotor case study

Previous studies, such as that of Leyko et al. (2010), focused on the propagation of waves through a single stator vane. This was also the case of Mishra and Bodony (2013) who performed a similar study to that of Leyko et al. (2010), but considered entropy waves only. In this section the case of a single rotating blade will be considered. The objective here is double: on the one hand the analytical model for the propagation of waves through rotating blades will be validated, both for acoustic and entropy waves; on the other hand, the two different numerical methods for the propagation of waves through rotating blades will be tested and validated before being used with the complete turbine stage.

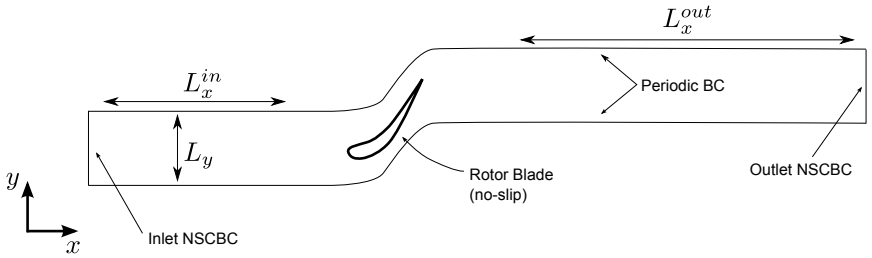

Figure 6.10 – *Sketch of the computational domain of the rotor configuration.*

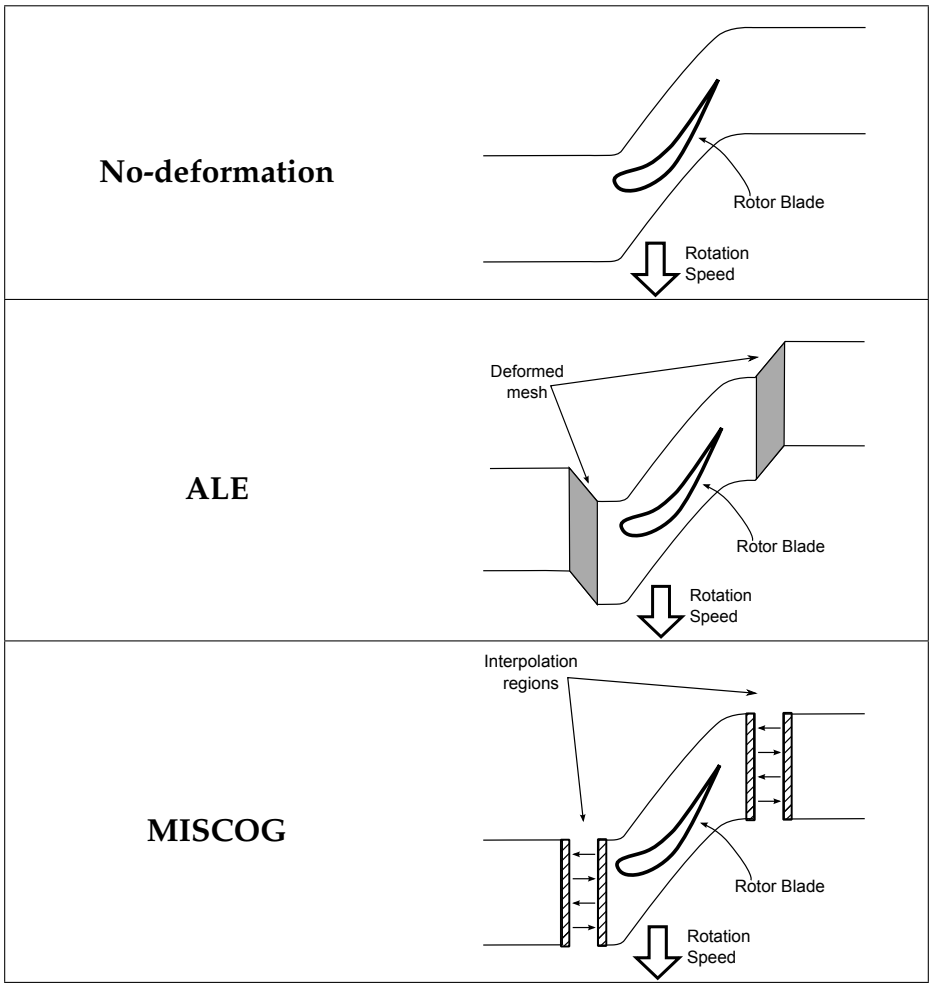

Table 6.3 – *The three methods used for the rotor simulation.*

The configuration is shown in figure 6.10, and the mean flow described in table 6.2. As the configuration consists of a single rotor blade, there is no need for a deforming mesh. For this reason the no-deformation method is first applied as explained in Section 6.1.1, in which the rotor velocity is prescribed in all the mesh (no mesh deformation and no interpolation are therefore needed).

In order to validate the numerical methods explained in Section 6.1.1 (the ALE and the MISCOG methods), the same rotor configuration is also computed with the two other methods. This allows for a comparison between them and the reference non-deforming simulation in order to assess the pos-

sible numerical errors induced before performing the complete stator-rotor simulation, which cannot be done using the non-deforming method and will be done using only the two methods as explained in table 6.1. The objective of this validation is to be aware of the possible numerical errors induced by the ALE and the MISCOG methods, as the no-deformation method cannot be used in the case of a complete turbine stage. Table 6.3 shows the three methods used.

Acoustic wave

Figure 6.11 shows the modulus of the acoustic transfer functions of the rotor blade as a function of frequency. The analytical theory is shown as a solid line, which is constant as the model predicts no frequency-dependence of the transfer functions (due to the compact assumption). This analytical solution is, as explained in Chapter 5, valid only for the low frequency limit. The three numerical simulations are also shown in the figure as symbols: (x) for the non-deforming simulation, ($\bullet$) for the ALE method and ($+$) for the MISCOG approach. The reduced frequency, as defined in Chapter 3, $\Omega = fL_n/c_1 = 0.1$, with L_n the rotor's axial length and c_1 the inlet sound-speed, is shown in both figures.

To begin with, it can be seen that the analytical theory and the numerical simulation present a strong agreement for the low frequency limit, which is one of the assumptions used to derive the analytical model. The second result is that despite this match at low frequencies, analytical and CFD results differ for higher frequencies: the reflected wave presents a strong non-compact response, with a peak value of around 0.6 at $f \approx 2800$ Hz, while for the low frequency limit the reflected wave is 0.3. This is not the case of the transmitted wave, where the compact theory is in good agreement with the numerical simulations for a wide range of frequencies, with relatively small differences.

Another important result is that the three numerical simulations are in close agreement and are almost superposed. This shows that both the ALE and the MISCOG methods are able to correctly compute the transmission of waves. The ALE method however presents a slight difference with the non-deforming and the MISCOG methods at a frequency of 2200 Hz. This is due to the interpolation frequency of the ALE method which generates a res-

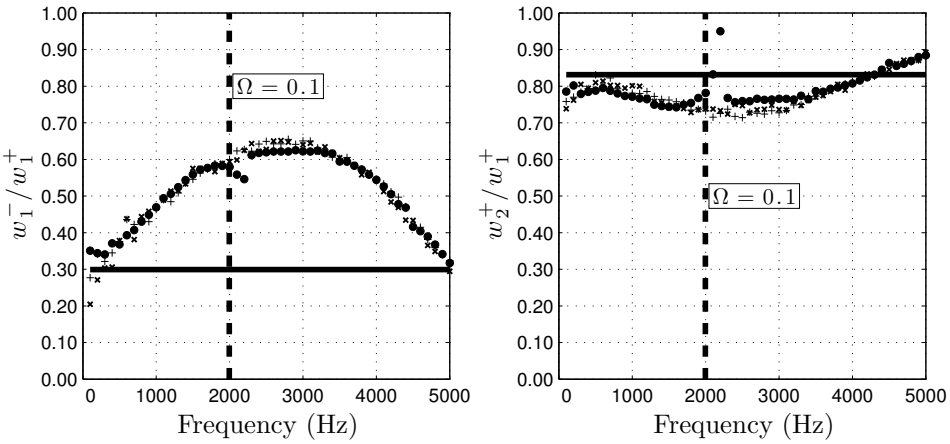

(a) Reflected wave

(b) Transmitted wave

Figure 6.11 – *Acoustic transfer functions. (——): Analytical theory; (x): No-deformation method; (•): ALE method; (+): MISCOG method.*

onance frequency as explained by Wang et al. (2013). This frequency occurs in the MISCOG method too but is not seen in this case as the interpolating frequency is a lot larger (the MISCOG method interpolates every time-step while the ALE method interpolates only when the mesh deformation is too large).

Entropy wave

The entropy transfer functions are plotted in figure 6.12, where again the analytical method is compared with numerical simulations. Results show a good agreement at low frequencies between the analytical method and the numerical simulation. The results obtained through numerical simulations present larger scattering than in the acoustic case. This is due to the lower signal-to-noise ratio in the entropy wave case than in the acoustic one. Indeed, the acoustic wave generated by the entropy one (indirect noise) is $w_2^+/w_1^s \approx 0.02$ while the direct noise is $w_2^+/w_1^+ \approx 0.8$ as seen in figure 6.11. This large differences seen in the transfer functions do not mean, however, that indirect noise is negligible compared with direct noise, as the ratio of entropy to acoustic waves generated by the combustion chamber should still have to be taken into account.

For the non-compact frequencies, the numerical simulations show that

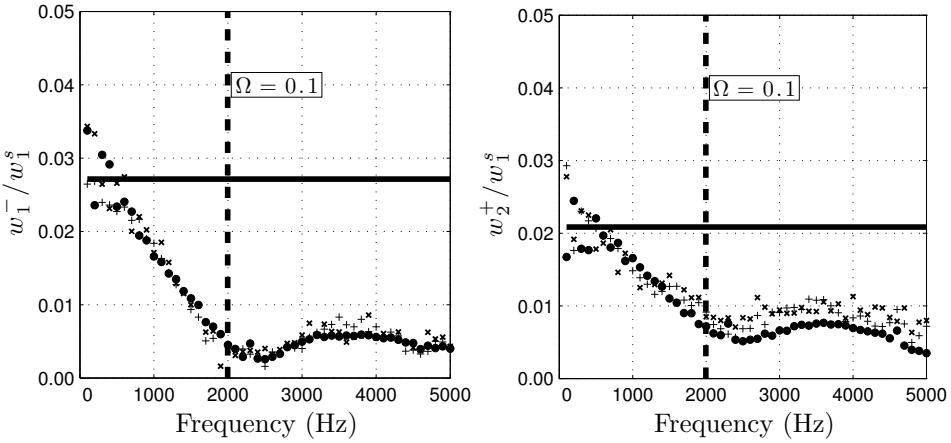

(a) Reflected wave (b) Transmitted wave

Figure 6.12 – *Entropy transfer functions. (——): Analytical theory; (x): No-deformation method; (•): ALE method; (+): MISCOG method.*

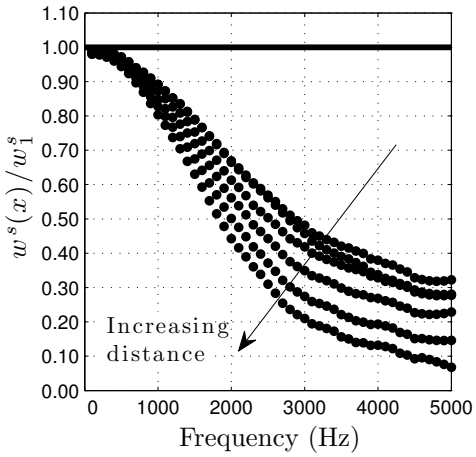

Figure 6.13 – *Entropy transmission through the rotor blade. (——): Analytical method; (•): Numerical simulations at different x locations, increasing from the trailing edge to a one-chord distance downstream.*

the analytical method clearly over-predicts the noise generated. This occurs because the amplitude of the plane entropy wave is reduced as it passes through the rotor blade, as seen in figure 6.13, an effect which is not considered in the analytical method presented in Chapter 5, where the entropy wave is supposed to propagate unaltered through the stator and rotor blades. Figure 6.13 shows that the entropy wave at the trailing edge is already significantly reduced. This shows that the dissipation of the entropy wave occurs in two steps: first the amplitude of the plane wave is reduced due to

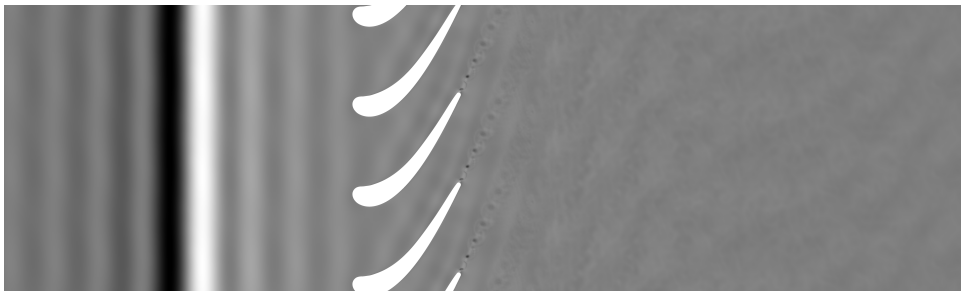

(a) $tf_0 = 0.1$

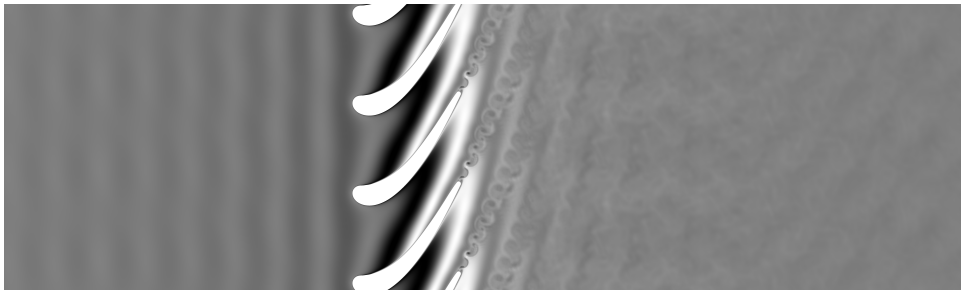

(b) $tf_0 = 0.2$

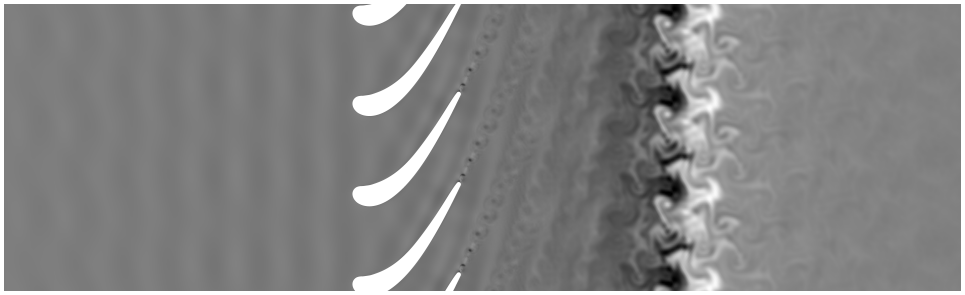

(c) $tf_0 = 0.3$

Figure 6.14 – *Instantaneous fields of the entropy wave propagating through the rotor blade, calculated using the MISCOG method. Note that the forcing function $f(t)$ from figure 6.7 is used here for a better visualisation of the flow.*

the passage through the blade, and then the wave is further attenuated as it travels downstream from the leading edge of the blade. To understand these two steps, the entropy wave through the rotor blades is shown in figure 6.14 for several instants. For a better visualisation of the flow, function $f(t)$ from figure 6.7 is used instead of $f_r(t)$ of figure 6.8. The initially plane entropy wave is first deformed by the mean flow through the blades. This was already shown by Leyko (2010) for the case of the single stator blade: the no-slip condition on the blades and the acceleration of the flow on the suction side of the blade (and the deceleration on the pressure side) imposes

an azimuthal dependency (y) of the mean flow which was neglected in the analytical model in the first place. The 2D flow prescribes a propagating velocity to the entropy wave which is dependent on the azimuthal direction, deforming in this way the initially plane front at the length-scale of the pitch length, L_y. This deformation transforms the plane wave into a sum of higher-order modes. It is important to note that the total entropy fluctuation is not dissipated but re-distributed into higher-order propagating modes. Figure 6.14 shows at the same time the mixing downstream from the rotor blade, which is responsible for the further attenuation shown in figure 6.13 for increasing distances from the leading edge.

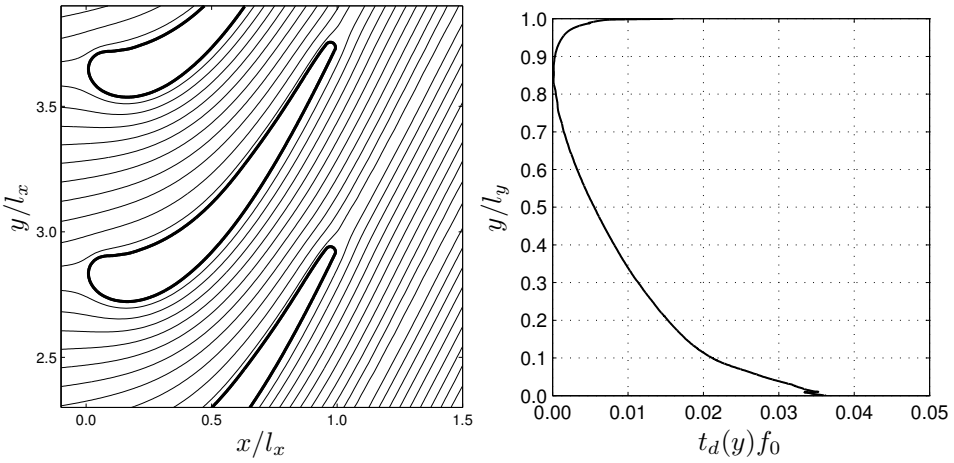

(a) Streamlines through the rotor blade

(b) Time-delay, $t_d(y)$, of the rotor.

Figure 6.15 – *Streamlines through the rotor blade in the rotating reference frame (a) and the time-delay function, $t_d(y)$, calculated using the mean flow the rotor.*

Leyko (2010) used the mean flow through the stator blade to predict the deformation of the entropy wave amplitude at the trailing edge of a stator blade due to the mechanism described above. In this way the attenuation of the plane mode (due to the re-distribution of entropy into higher-order modes and not to dissipation) can be modelled. To do so, the streamlines through the rotor are shown in figure 6.15(a). Using the mean flow velocity, the time delay in arrival of the streamlines at the outlet, $t_d(y)$, can be calculated and is plotted in figure 6.15(b), showing the azimuthal dependency of the flow. This time delay is responsible for the deformation of the initially plane entropy wave, and the scattering into higher-order modes. Leyko (2010) used this time delay to calculate the attenuation of the plane

mode propagating through the stator, giving

$$D_0(f) = \left| \frac{1}{L_y} \int_0^{L_y} \exp\{2\pi i f t_d(y)\}\, dy \right|. \tag{6.17}$$

The value of the attenuation given through this expression is plotted in figure 6.16 for the rotor blade. The model is able to correctly predict the attenuation due to this mechanism. The model, however, does not consider the attenuation of the entropy wave downstream from the trailing edge, as seen in figure 6.13, which is due to the mixing of the plane wave by the downstream turbulent mean flow. This type of mixing has been studied in detail by Morgans et al. (2013) in the case of a turbulent channel-flow.

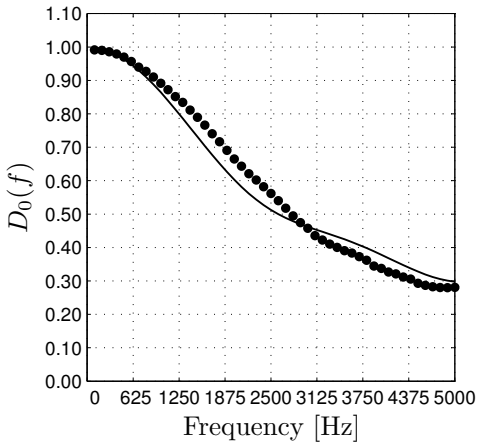

Figure 6.16 – *Attenuation of the entropy wave due to the deformation of the plane mode by the mean flow through the rotor, $D_0(f)$, calculated using $t_d(y)$ of figure 6.15(b) (——), and obtained numerically at the outlet of the rotor blade (•).*

Function $D_0(f)$ represents the 'attenuation' of the plane mode due to the deformation of the wave, and can be used to correct the entropy transfer functions. The entropy wave generating indirect noise (and indirect reflected waves) is considered to be the injected plane entropy wave attenuated by the function $D_0(f)$ in the analytical model. Results are plotted in figure 6.17, showing a better agreement with numerical results. The new transfer functions go towards zero as the frequency increases due to the higher attenuation of the entropy wave at these frequencies.

Finally, the comparison of the two numerical methods for the rotation of the mesh shows a good agreement with the non-deforming mesh. The MISCOG method gives better results as it does not generate spurious acoustic waves at 2200 Hz (which are mainly seen in the acoustic case). This is of

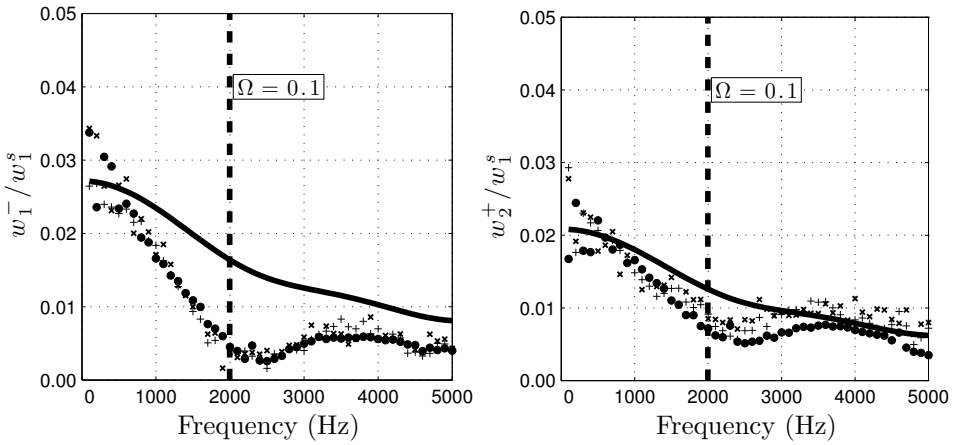

(a) Reflected wave

(b) Transmitted wave

Figure 6.17 – *Entropy transfer functions for the rotor blade with the attenuation function model, $D_0(f)$. (——): Analytical method; (x): No-deformation method; (•): ALE method; (+): MISCOG method.*

great importance for the next section, where the stator-rotor configuration will be studied and the non-deforming method cannot be used.

6.3 Stator-Rotor case study

The complete turbine stage (stator-rotor configuration of figure 6.1) is computed using the two mesh movement methods explained in Section 6.1, as seen in table 6.4. Even if these two methods were validated in the previous section already, both methods (ALE and MISCOG) will still be used to compare their results. The mean flow characteristics are described in table 6.5. Using these mean flow variables, the analytical theory of Chapter 5 is used to compute the acoustic and entropy transfer functions of the turbine stage. This analytical solution is then compared with the numerical simulations performed with both methods for rotation.

Acoustic wave

The acoustic reflection and transmission coefficients are plotted in figure 6.18, comparing the analytical method with the numerical simulations

ALE	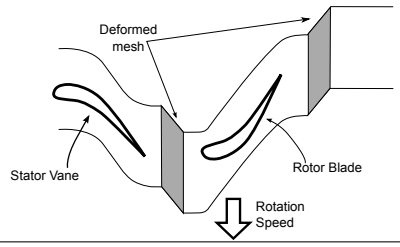
MISCOG	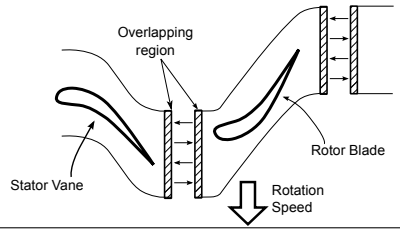

Table 6.4 – *The two methods used for the stator-rotor simulation.*

	Stator		Rotor	
	Inlet	Outlet	Inlet	Outlet
Mach	0.166	0.661	0.661	0.31
θ	0	-71.8	-71.8	-32.7
c [m/s]	798.3	773.0	773.0	755.1
γ	1.32	1.32	1.32	1.32
U [m/s]	0		-500	
Π	1		0.67	
$\psi = -\frac{\Delta h_t}{U^2}$	0		0.75	
L $[m]$	0.04		0.06	

Table 6.5 – *Mean flow characteristics of the stator-rotor case.*

of the stator-rotor stage. It should be noted that, even if the analytical method is frequency dependent, it is still based on the compact assumption and therefore is strictly valid only for low frequencies. It is interesting to note that the method performs well for frequencies ranging from 0 to 2000 Hz, and even up to 4000 Hz in the case of the transmitted wave. The value of the reduced frequency $\Omega = fL_s/c_s = 0.1$ (where c_s is the inlet sound speed of the stator and L_s the stator axial length) is also plotted. The analytical method predicts within reasonable precision the transmitted and reflected acoustic waves even for non-zero frequencies. Both numerical methods agree, validating the numerical results. The spurious solution found in the rotor case at a frequency of 2200 Hz is not recovered in this simulation. The larger scatter of numerical results for the transmitted acoustic wave is due to the noise generated by the stator's and rotor's wake.

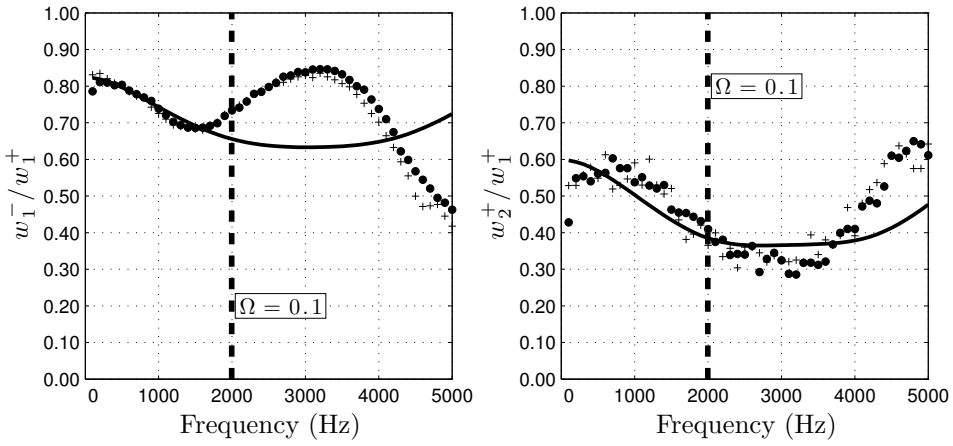

(a) Reflected wave

(b) Transmitted wave

Figure 6.18 – *Acoustic transfer functions. (——): Analytical method; (•): ALE method; (+): MISCOG method.*

Entropy wave

The transfer functions of the stator-rotor stage forced with entropy waves are plotted in figure 6.19. The analytical method and the numerical simulations agree for the low frequency range, where the compact assumption is valid. Both numerical simulations agree on most of the spectrum, except again for the larger scattering of the transmitted wave in the

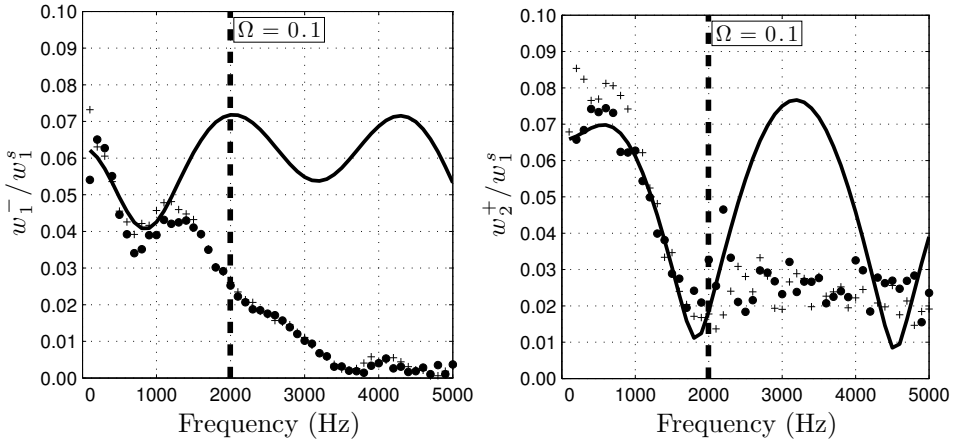

(a) Reflected wave (b) Transmitted wave

Figure 6.19 – *Entropy transfer functions. (——): Analytical theory; (•): ALE method; (+): MISCOG method.*

MISCOG method. This is most likely due to the resolution of the mean flow for the MISCOG method, which generates better resolved and convected stator wakes and stator-rotor interaction, yielding larger broadband noise. The ALE method does not present this problem as the small scale turbulence is dissipated through the deforming region and the interpolation. It can also be noted that the frequency dependence of the transfer functions is recovered at low frequency using the method of Chapter 5, even if the compact assumption is made. In particular, for the indirect noise generated by an unitary entropy wave, figure 6.19(b), results are valid for reduced frequencies up to $\Omega = 0.1$, or equivalently $f = 2000$ Hz. This is not the case for the reflected wave where the analytical solution and the numerical simulations start to diverge at around $f = 700$ Hz.

For larger frequencies, however, large discrepancies exist between the numerical transfer functions and the analytical ones. Both the reflected and transmitted coefficients, calculated numerically, tend towards zero while the analytical method does not. As explained in the rotor case, this is due to the attenuation of the plane entropy wave. The entropy wave through the stator-rotor configuration is shown in figure 6.20 for several instants, showing the deformation of the wave when traversing both the stator and the rotor blade, and the turbulent mixing downstream from the rotor blade. Figure 6.21 shows the entropy transmitted to the outlet of the stator-rotor as a function of the frequency, showing that it is not conserved throughout

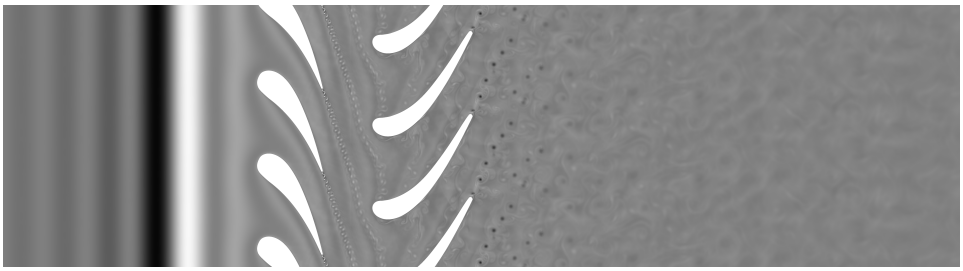

(a) $tf_0 = 0.1$

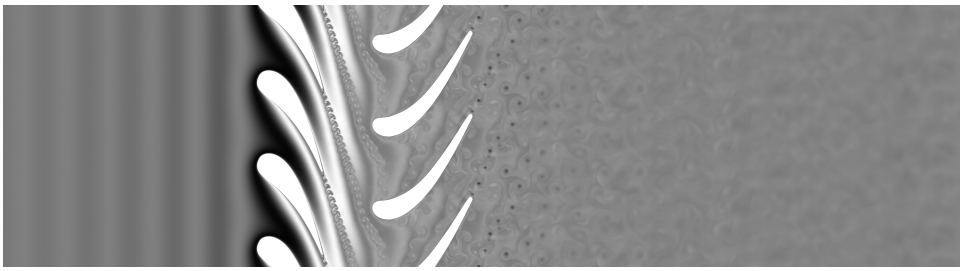

(b) $tf_0 = 0.15$

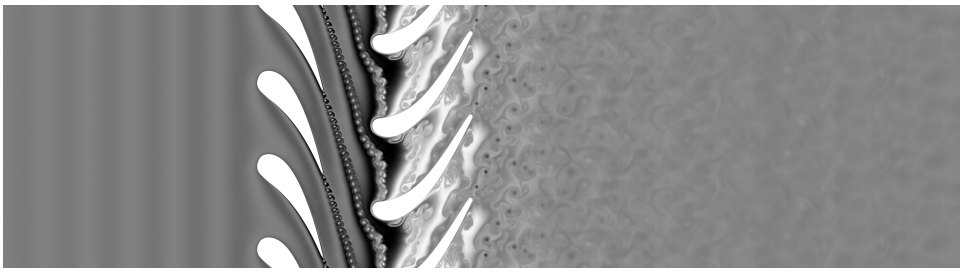

(c) $tf_0 = 0.18$

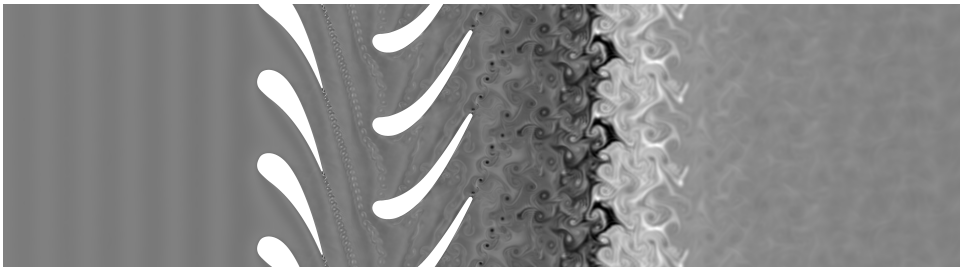

(d) $tf_0 = 0.24$

Figure 6.20 – *Instantaneous fields of the entropy wave propagating through the stator-rotor configuration, calculated using the MISCOG method. Note that the forcing function $f(t)$ from figure 6.7 is used here for a better visualisation of the flow.*

the stages.

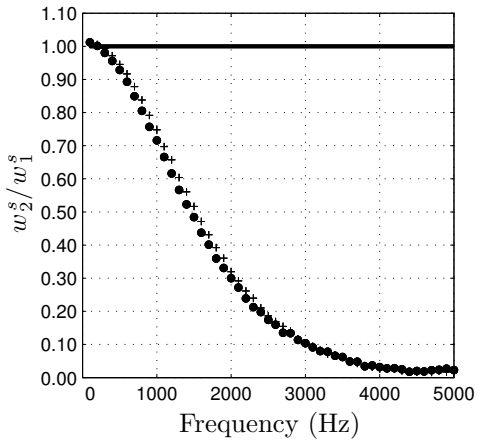

Figure 6.21 – *Entropy transmission throughout the stator-rotor. (——): Analytical model; (•): ALE method; (+): MISCOG method.*

The same method used for the single rotor case is here applied to the stator-rotor configuration. The streamlines for the stator and the rotor cases are shown in figure 6.22(a) and figure 6.22(b). Using the mean flow velocity, the time delay in arrival of the streamlines at the outlet, $t_d(y)$, is calculated and plotted in figure 6.23 for both the stator and rotor blades.

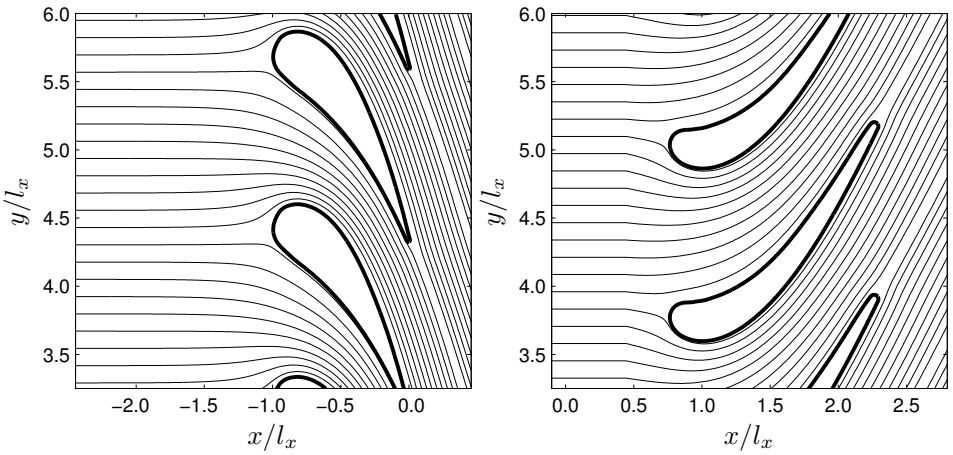

(a) Stator (b) Rotor (in rotating frame)

Figure 6.22 – *Streamlines through the turbine blades obtained using the mean flow of the MISCOG simulation.*

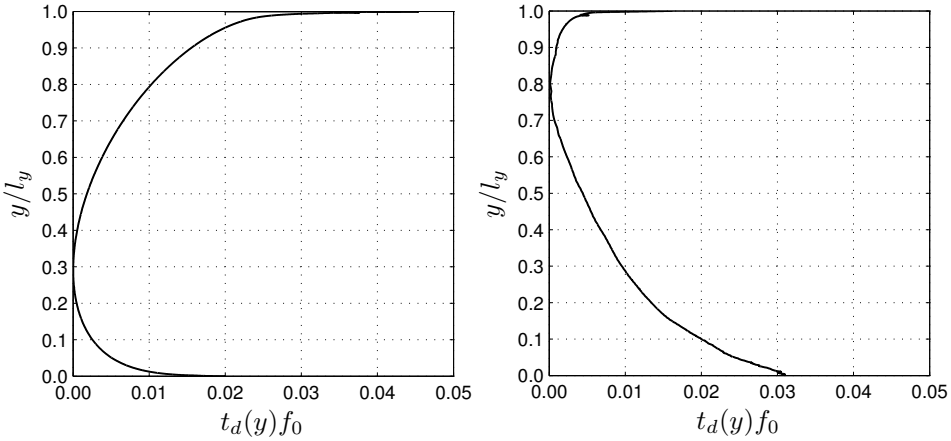

(a) Stator (b) Rotor

Figure 6.23 – *Value of $t_d(y)$ obtained using the mean flow of the MISCOG simulation.*

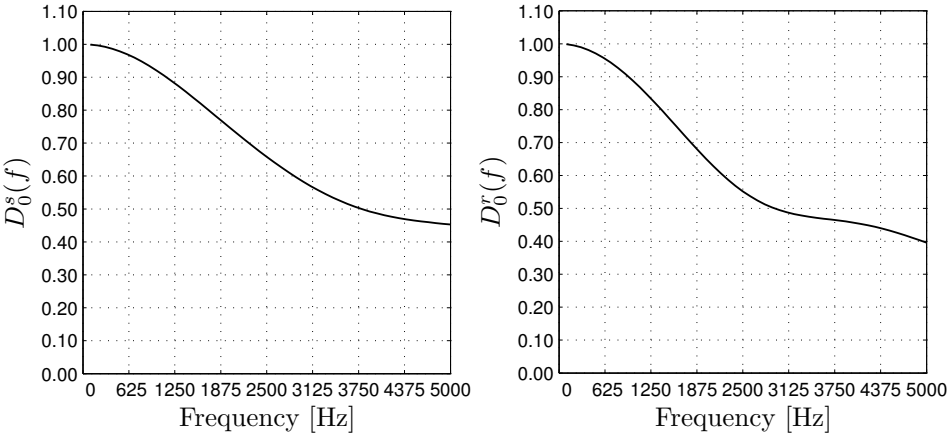

(a) Stator (b) Rotor

Figure 6.24 – *Attenuation of the entropy wave due to the mean flow, $D_0^s(f)$ and $D_0^r(f)$ calculated using $t_d(y)$ of figure 6.23.*

The value of the attenuation given through equation (6.17) is plotted in figure 6.24 for the stator and the rotor blade independently. Leyko et al. (2013) showed that this method was able to predict, within reasonable precision, the attenuation of the plane entropy wave when propagating through a single stator blade. This was seen to be the case for the rotor blade in Section 6.3 too. The total entropy attenuation of the plane mode can be obtained as a convolution of both transfer functions, which in the frequency domain results in the multiplication of $D_0^s(f)$ and $D_0^r(f)$. The result is

shown in figure 6.25, as a function of frequency, compared with the numerical results, showing that the model improves the constant entropy assumption of the analytical method and provides a reasonable estimate for the attenuation in the stage. The model of Section 6.2, used for the attenuation of the entropy wave, represents only the attenuation due to the deformation of the wave when passing through the blade row. It does not take into account the mixing due to the propagation of the entropy wave through the inter-blade spacing (figure 6.13), in which the flow presents large turbulence levels and the entropy wave is dissipated. This explains the under-prediction of the attenuation of the entropy wave by the model when compared with the numerical simulations.

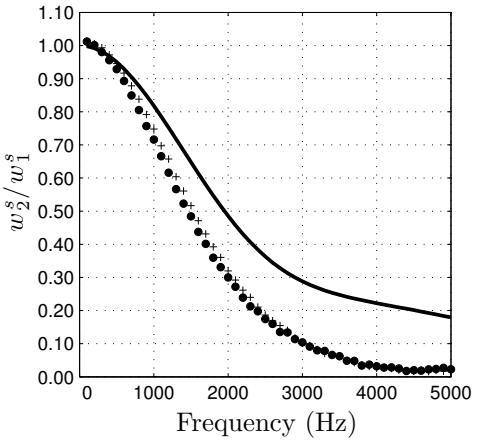

Figure 6.25 – *Entropy transmission through the stator-rotor. (——): Model for the entropy attenuation; (•): ALE method; (+): MISCOG method.*

The analytical method can then be corrected introducing the attenuation functions $D_0^s(f)$ and $D_0^r(f)$ into the analytical model to provide the entropy transfer functions when considering its attenuation, as done for the rotor case. Results are plotted in figure 6.26, showing a better agreement with numerical results. The new transfer functions tend towards zero as the frequency increases due to the higher attenuation of the plane entropy wave at these frequencies, providing a good estimate of the entropy transfer functions, and in particular indirect noise generation, when considering the attenuation of the entropy wave.

It is interesting to check if the noise levels of the stator-rotor interaction are lower than the measured noise levels due to the forcing. This is particularly important for the case of the entropy wave, as it generates acoustic

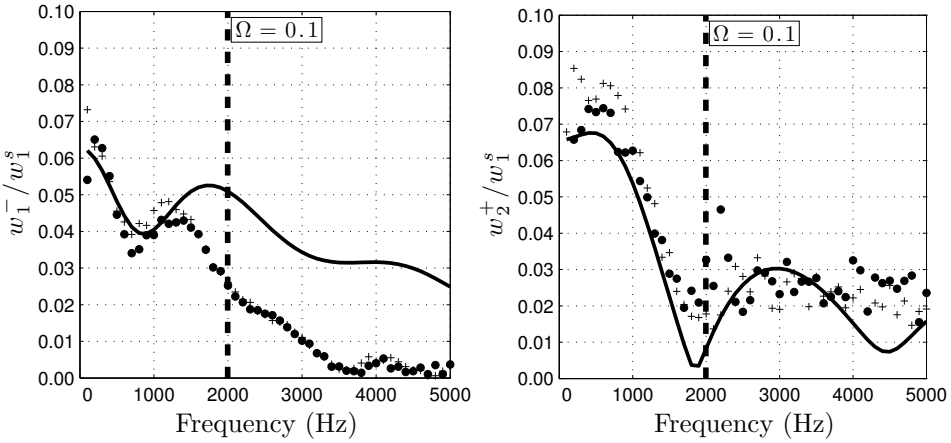

(a) Reflected wave (b) Transmitted wave

Figure 6.26 – *Entropy transfer functions. (——): Analytical method with correction on the entropy wave; (•): ALE method; (+): MISCOG method.*

waves of the order of 0.05 times its magnitude. As the entropy levels have to be kept low to remain linear, the acoustic wave generated by this wave is even lower and may have a signal-to-noise ratio too low to be measured. Figure 6.27 shows the absolute value of the acoustic waves generated by the entropy wave forced at the inlet computed using the MISCOG method.

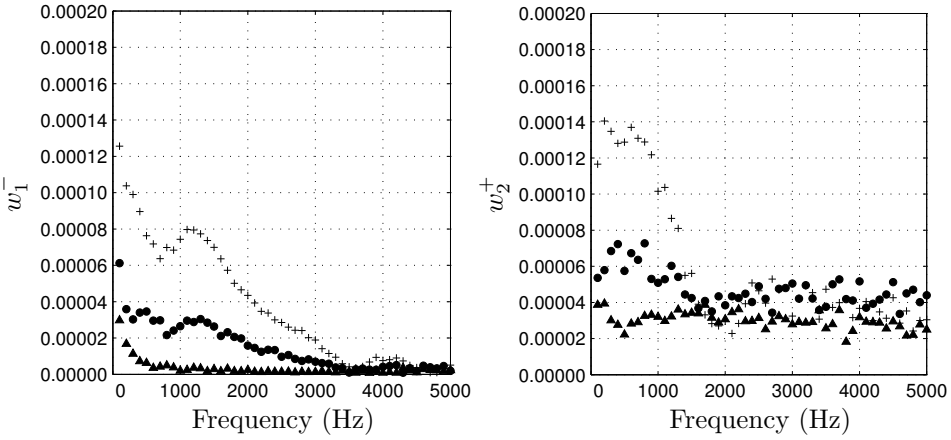

(a) Reflected wave (b) Transmitted wave

Figure 6.27 – *Acoustic waves at the inlet (a) and at the outlet (b). (▲): Reference simulation with no forcing; (•): forcing the entropy wave at the inlet using $f(t)$ from figure 6.7; (+): forcing the entropy wave at the inlet using $f_r(t)$ from figure 6.8.*

Results show the value of the background noise generated by the configuration, which is obtained with a reference simulation in which no wave is forced. The acoustic waves w^+ generated by the entropy forcing are also shown in figure 6.27 for the forcing term $f_r(t)$ from figure 6.8 (as explained previously, this is the forcing term used to obtain all the transfer functions). The levels of reflected acoustic wave generated by the entropy wave are larger than the noise levels at low frequencies. At high frequencies, however, the amplitude of the acoustic wave generated by the entropy wave is reduced as shown previously, and noise levels become relatively important in comparison, polluting the solution. This is also the case of the transmitted wave, where it can be seen that the noise levels of the reference simulations are a lot larger than at the inlet due to the interaction of turbulence with the rotor blade. In this case the signal-to-noise ratio is too low for frequencies larger than 2000 Hz.

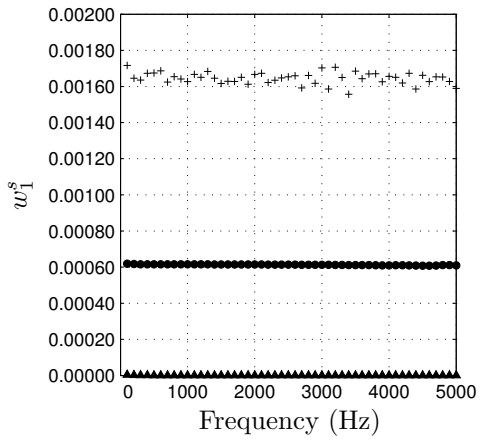

Figure 6.28 – *Entropy waves forced the inlet. (▲): Reference simulation with no forcing; (•): forcing the entropy wave at the inlet using $f(t)$ from figure 6.7; (+): forcing the entropy wave at the inlet using $f_r(t)$ from figure 6.8.*

Figure 6.27 shows at the same time a simulation performed using function $f(t)$ from figure 6.7. As previously explained, this function present a larger maximum value than $f_r(t)$ and therefore the forcing amplitude of the entropy wave must be much lower for the forcing wave to remain linear. For this reason the acoustic waves generated by this forcing are 2.7 times lower than with $f_r(t)$, reducing therefore the signal-to-noise ratio by a factor of 2.7. Figure 6.28 shows that the amplitude of the entropy wave forced is 2.7 times larger for the case where the forcing is performed with $f_r(t)$ than for the simulation with $f(t)$, while the maximum amplitude of the signal

remains of the same order thanks to the random phase-shift introduced in $f_r(t)$.

Conclusions

An analytical method based on the compact row assumption has been presented to solve the propagation of acoustic, entropy and vorticity waves through a turbine. This method, based on the conservation of the fluctuating mass, rothalpy and entropy, uses the Cumpsty and Marble (1977) method, applying it to rotating blades in which the enthalpy jump is considered. This method is able to compute both the propagation of acoustic and entropy waves through turbine blades, which are responsible for direct and indirect combustion noise respectively. The method is based on a 2D configuration and considers therefore the flow deviation induced by the stator and rotor blades, which was neglected in Part I when considering only quasi-1D nozzles, as well as vorticity waves and the circumferential modal component of the perturbations. The method, however, is based on a compact assumption as it considers the stator and rotor blades to be short compared to the acoustic wavelength.

To validate the analytical method, results have been compared with numerical simulations for the cases of a single rotor blade and a stator-rotor stage. To compute the relative displacement of the stator and the rotor blade, two different numerical methods have been used to compute the Navier-Stokes equations in moving meshes. They were compared with a non-deforming simulation in the case of the rotor blade in order to validate the numerical methods. The comparison shows that both methods (ALE and MISCOG) are able to correctly compute the propagation of acoustic and entropy waves through the turbine stages. Small differences between the two numerical methods are explained and caused by both the interpolations performed and by the dissipation induced by the interpolation of the ALE method, which reduces turbulence levels in the downstream region and therefore presents less self-noise levels. The coupling method used in the MISCOG method allows for a better convection of vortex and entropy

though the interfaces than the ALE method.

The comparison of the numerical results with the analytical model shows that the response of the rotor configuration was correctly predicted for frequencies up to 2000 Hz in the case of the acoustic transmission coefficient. The analytical solution is able to correctly predict the acoustic reflection coefficient, but the compact solution and the numerical simulations present larger discrepancies at non-compact frequencies than for the transmission coefficient. The entropy transfer function calculated using the analytical method is in good agreement with the numerical simulations for the compact frequencies, but presents, however, large discrepancies at high frequencies. It has been found that this is caused by the deformation of the initially plane entropy wave generating higher order modes. This occurs due to the circumferential dependency of the mean flow through the stator and rotor blades, which deforms the initially plane waves due to the no-slip condition and the acceleration of the flow in the suction side of the blade, as already observed by Leyko et al. (2013). The attenuation of the plane entropy wave in this case is due to the re distribution of entropy into higher order modes and not due to turbulence mixing or heat conduction. For the stator-rotor configuration similar results were found: the acoustic transfer functions were correctly predicted by the analytical method, while the entropy transfer functions were over-predicted at non-compact frequencies because the attenuation of the entropy was not taken into account in the Cumpsty and Marble (1977) model.

Using Leyko's model for plane entropy wave dissipation, a correction has been introduced into the model to account for the loss of amplitude of the plane entropy wave while propagating through the fixed and rotating blades. The correction is supported by the numerical results up to higher frequencies for both the rotor and stator-rotor configurations. This shows that the plane entropy wave is strongly attenuated when propagating through turbine blades and that this should be taken into account to correctly predict indirect combustion noise. Results show that the method can be used to predict, within reasonable accuracy, the acoustic and entropy transfer functions for frequencies up to 2000 Hz.

Part III

Predicting combustion noise combining LES and analytical tools for the propagation of waves

Table of Contents

Introduction **145**

7 Description of the methodology **147**

7.1 Compressible reactive LES of the combustion chamber 147

7.2 The CHORUS post-processing 150

7.2.1 Primitive variables 151

7.2.2 Waves at the outlet of the combustion chamber 153

7.2.3 Transmission through the turbine stages 155

7.2.4 Acoustic power computation 157

8 Application to an aero-engine **159**

8.1 LES of the combustion chamber 159

8.1.1 Flow description 162

8.2 Waves in the combustion chamber 164

8.3 Direct and indirect combustion noise 165

Conclusions **171**

General conclusions and perspectives **173**

Introduction

Parts I and II have focused on the propagation of waves through non-homogeneous flows. Results show that analytical methods can predict the propagation of acoustic and entropy waves through turbine blades with reasonable accuracy. In Part II the analytical method of Cumpsty and Marble (1977) was shown to correctly predict the propagation of acoustic waves and the generation of indirect noise for both a single rotor blade and a complete turbine stage (stator-rotor). This propagation is essential when computing combustion noise and has to be taken into account to predict indirect noise. The method considers acoustic, entropy and vorticity waves, and can be used with both fixed and rotating blades.

The analytical methods explained in the previous chapters are used in this part to compute the noise generated at the outlet of an aero-engine. A complete numerical simulation of combustion noise will require the numerical set-up to include the complete combustion chamber with the turbine stages (as explained in Section 1.4). This is unfeasible with actual computational resources and for this reason numerical tools have to be combined with analytical methods to reduce the CPU cost.

CHORUS is a tool for the prediction of combustion noise which applies this hybrid methodology. The development started during the PhD of Leyko (2010) and was continued in this work. Chapter 7 presents the method and the assumptions made: Section 7.1 focuses first on the LES methodology of the combustion chamber and Section 7.2 details how the waves are extracted from the LES and propagated through the turbine stages. Chapter 8 presents the results of a practical application of the methodology for computing the combustion-generated noise of a real aero-engine.

Note that CHORUS methodology is restricted to the low frequency (com-

pact) limit because the analytical model of Part I does not account for the deviation of the flow and for enthalpy jumps found in turbine stages. For this reason, the analytical model of Part II is used.

Chapter 7

Description of the methodology

In this chapter the CHORUS methodology is presented. The method first requires a Large Eddy Simulation (LES) of the combustion chamber using the AVBP solver (Schønfeld and Rudgyard, 1999), providing the noise sources generated by the interaction of the flame with the turbulent flow. At the outlet of the combustion chamber the LES data is post-processed using CHORUS. CHORUS extracts the acoustic, entropy and vorticity waves at the outlet of the combustion chamber and propagates them through the turbine stages using the analytical method of Cumpsty and Marble (1977).

7.1 Compressible reactive LES of the combustion chamber

To correctly predict combustion noise, the combustion process and the generation of acoustic, entropy and vorticity waves within the combustion chamber must first be accurately solved. In this section the LES method is briefly described, however, the reader is referred to Pope (2000) for more details on the LES methodology, and to Poinsot and Veynante (2011) for more details on reactive LES.

Since noise sources (in this case the flame dynamics) must be captured accurately, RANS simulations are actually not adapted as the unsteady

features of the flow would have to be modelled. The unsteadiness of the heat release is mainly due to turbulence-flame interactions and to acoustics-flame interactions, and for this reason a resolved compressible reactive Large Eddy Simulation (LES) is more suited. A proper LES simulation can solve the large turbulent structures of the flow, which are responsible for the low-frequency wrinkling of the flame and therefore the unsteady heat release that generates noise. Small-scale turbulence is not resolved and must be modelled appropriately (Smagorinsky, 1963) to consider its dissipation in the mean flow.

The flame model is of great importance too. The flame thickness is usually smaller than the grid size of any LES simulation and must be modelled or thickened artificially to be properly resolved in the computational mesh, including in this way an extra layer of modelling. The modelled flame has to react correctly to velocity, temperature and in some cases mixture fraction fluctuations in the flame front, and therefore the model can be a key element when computing combustion noise. The flamelet formulation has been used for non-premixed cases (Ihme and Pitsch, 2012) while the G-equation (Matalon and Matkowsky, 1982; Kerstein, 1988) is more adapted for modelling the flame in premixed combustion cases. A more general method is to use the thickened flame model (Butler and O'Rourke, 1977) which has the advantage of dealing with both premixed and non-premixed flames. This is the case of modern aero-engines where the flow is partially premixed, and therefore both premixed and diffusion (non-premixed) flames may be present. The idea behind this model is to artificially increase the flame thickness by multiplying the thermal diffusivity (D) by a factor F and dividing the pre-exponential constant (A) by the same factor. As the flame thickness scales as $\delta \sim \sqrt{D/A}$ and the laminar flame speed as $s_l \sim \sqrt{DA}$, the new flame would be F times thicker (in order to be resolved by the mesh) while conserving the original laminar flame speed. The main drawback of this formulation is that the Damköhler number ($D_a \sim \tau_t/\tau_c$, where τ_t and τ_c are the turbulent and chemical characteristic times respectively) is also divided by a factor F, which means that vortices cannot wrinkle the thickened flame in the same way as they do with the real thin flame. The wrinkling of the flame by turbulent scales has a big influence on both mean quantities (turbulent flames have larger flame speeds) and on fluctuating quantities (RMS and heat release fluctuations), and therefore noise generation. For this reason the wrinkling of the flame must be appropriately modelled. This is done through an efficiency function (Colin et al., 2000) obtained from canonic DNS simulations. The advantage of using a thickened flame formulation,

however, is first that a multi-species combustion with different non-unity Lewis numbers can be considered as the flame front is resolved in the mesh and not only as a discontinuity of the flow, and at the same time the level of modelling tends towards zero when the mesh size is reduced. This last point is of great importance as, when performing resolved LES, the numerical solution should tend towards the real one when the mesh size tends to zero.

The chemical schemes are just as important as the flame or the LES models. The combustion of kerosene is a very complex process involving hundreds of species and thousands of reactions, which cannot be taken into account in a realistic application. The chemical kinetic schemes are usually simplified eliminating a large part of the reactions to obtain reduced combustion models. This process is described for example by Luche (2003) and Luche et al. (2004). The reduction of the kinetic scheme which can be used for LES, leads in general to a one or two-step chemistry, involving less than 10 species in total. It should be noted that for each species in the reaction, an extra transport equation must be solved in the LES for the species considered, and thus the interest in reducing the complexity of chemical schemes. Unfortunately, the neglected reactions are of great importance for the flame structure, the propagating speed and the adiabatic temperature, mostly at large equivalence ratios. This occurs because rich flames generate larger amounts of NO_x, CO_2 and unburnt hydrocarbons, which are in general not modelled by the simplified chemistry. To correct the adiabatic temperature and the propagating speed, the BFER two-step reaction model of Franzelli et al. (2010) and Franzelli (2011) is used here. It includes a reversible reaction and a correction of the Arrhenius law as a function of the local equivalence ratio, in order to fit detailed chemistry. This is of great importance as the adiabatic temperature of the flame is responsible for the entropy spots and therefore for indirect noise.

In general, fuel is injected into the combustion chamber in liquid form, evaporating and burning inside the combustion chamber. The effect of droplet evaporation and combustion has been studied in depth, and several combustion regimes have been identified (Chiu et al., 1982), depending on whether drops burn individually or as a group. From a numerical point of view, the bi-phasic flow can be modelled through an Eulerian description (Zhang and Prosperetti, 1994a,b) where a statistical approach is used, or through a Lagrangian method (Sirignano, 1999) where droplets are tracked as they are entrained and evaporated through the flow. The two-phase na-

ture of the flow can be of great importance when modelling the combustion process as it can change the dynamics of the flow, generating for example regions of unburnt fuel downstream of the flame, which burn isolated and produce large-amplitude hot spots and acoustic waves. The effects of the two-phase flow can be neglected if the evaporation time is much larger than the convective time (from the injector to the flame). In this case, the fuel arrives to the flame region fully evaporated. In this work the effects of a two-phase flow are not taken into account and a single phase LES is considered.

7.2 The CHORUS post-processing

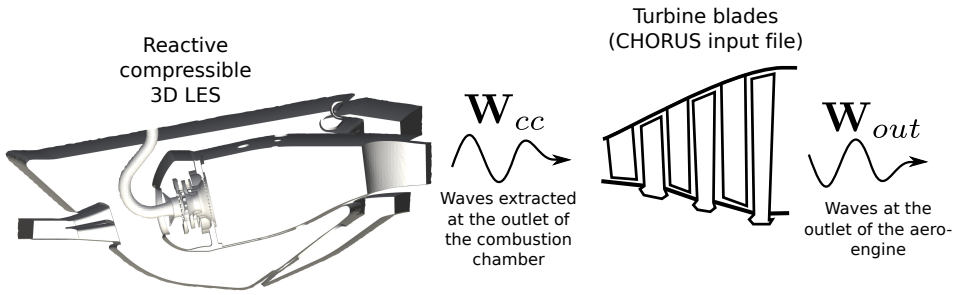

Figure 7.1 – *Sketck of CHORUS methodology for computing combustion noise.*

The starting point of the CHORUS methodology is the converged LES of the combustion chamber which will be post-processed to obtain the vector of waves at the outlet of the combustion chamber ($\mathbf{W}_{cc}$). These waves are then propagated through the turbine stages using analytical methods, as shown in figure 7.1, to obtain the acoustic waves at the outlet of the turbine ($\mathbf{W}_{out}$). The LES should first be run using a fixed time-step to gather data for post-processing. As the objective is to obtain the acoustic waves emitted by the aero-engine as a function of frequency (the power spectrum), some simulation parameters should be respected. In particular, the lowest frequency resolved is given by the inverse of the total simulated time, $f_{min} = \Delta f \sim 1/T$, and therefore the longer this time is, the better the frequency resolution. At the same time, the maximum value of the frequency is given by the inverse of the time step between saved solutions, $f_{max} \sim 1/\Delta t_{save}$, and therefore the interest of saving the solutions frequently. For these reasons, and to reduce memory consumption, the full 3D solution of the combustion chamber is

interpolated into a reduced 2D mesh plane placed at the outlet of the combustion chamber as seen in figure 7.2, where the waves $\mathbf{W}_{cc}$ are measured.

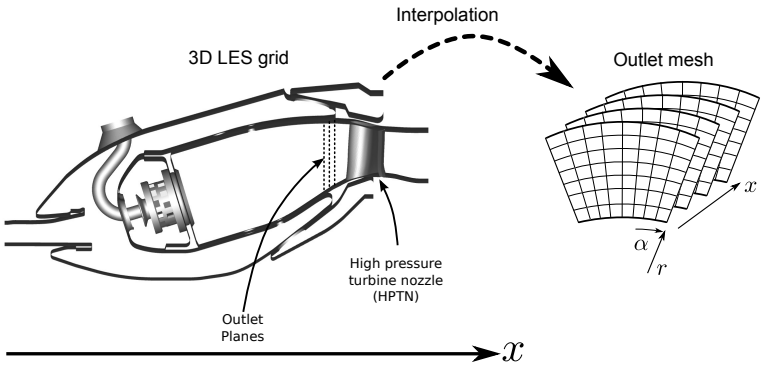

Figure 7.2 – *Interpolation of LES results at several outlet planes of the engine.*

The 2D outlet plane is perpendicular to the axis of the aero-engine. Several of these planes are used at different x locations in order to average axially the solution and to distinguish the hydrodynamic and acoustic pressure fluctuations. This method will be explained in Section 7.2.2. The planes are located at different axial locations at approximately one chord distance downstream from the first stator blade to avoid the potential effect, as seen in figure 7.2. The solutions stored in this reduced mesh will be then used by CHORUS to compute the waves generated by the combustion chamber ($\mathbf{W}_{cc}$), propagate these waves through the turbine blades and finally compute the generated noise at the outlet of the aero-engine. The method is divided into 4 parts: computation of the primitive variables, computation of the waves in the combustion chamber ($\mathbf{W}_{cc}$), transmission through turbine stages and computation of the acoustic waves ($\mathbf{W}_{out}$), and is illustrated in figure 7.3.

7.2.1 Primitive variables

The post-processing performed by CHORUS is done at each plane at the outlet of the computational domain shown in figure 7.2. The velocity vector is first projected into the polar coordinates system of the engine, $(u_x, u_y, u_z) \rightarrow (u_x, u_\alpha, u_r)$. The primitive variables considered will be those used in the analytical method of Part II: the entropy, pressure and velocity magnitude and angle. As the analytical model for the propagation of waves is 2D, the primitive variables in the outlet plane are first averaged radially.

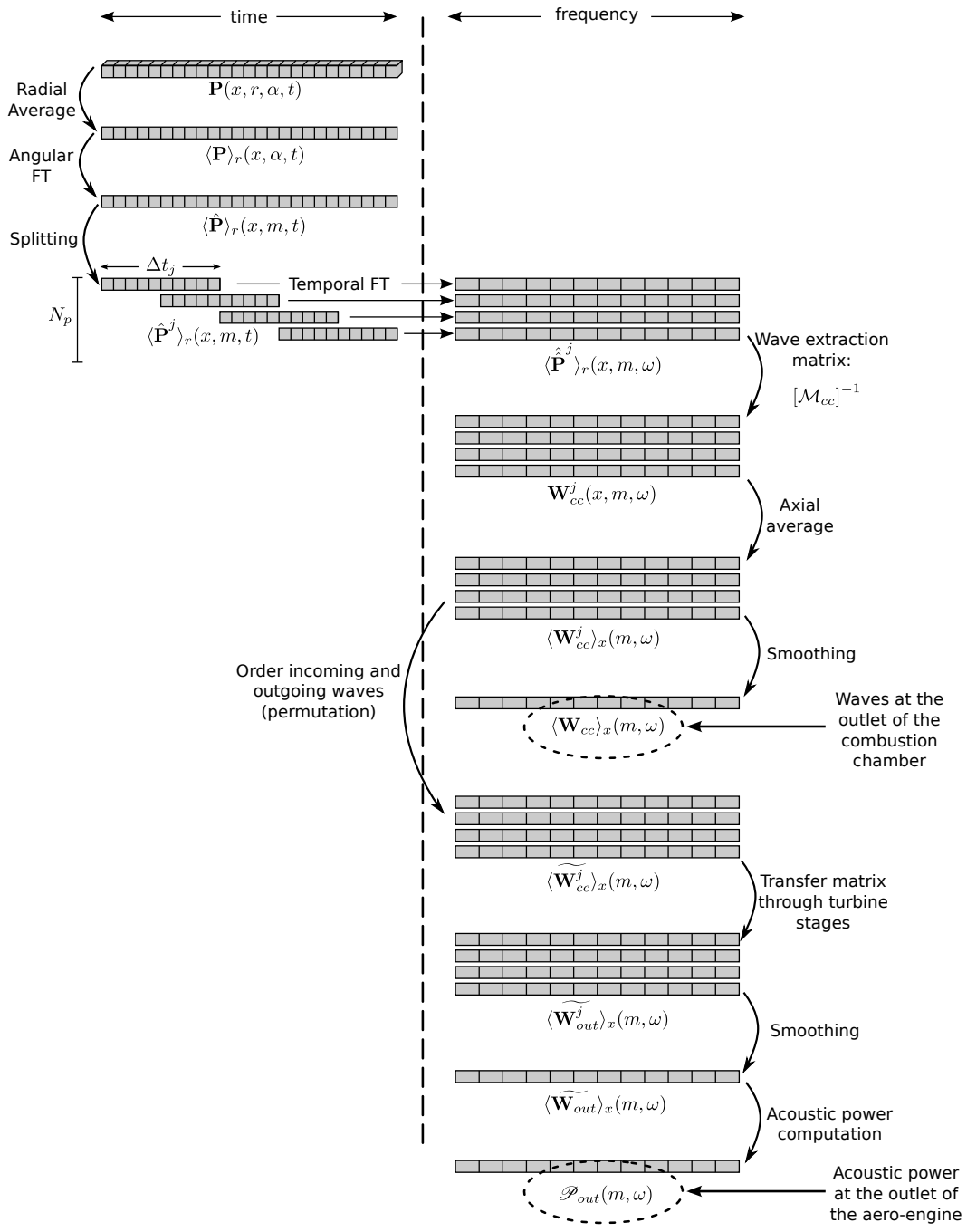

Figure 7.3 – *CHORUS procedure for computing the waves at the outlet of the combustion chamber and the noise generated at the outlet of the aero-engine (adapted from Leyko 2010).*

The fluctuation (over time) is then calculated at each point to obtain the time-dependent fluctuations, which are finally normalised to give the vector of primitive variables, $\langle \mathbf{P} \rangle_r (x, \alpha, t) = [s'/c_p, p'/(\gamma p), w'/c, \theta']$, where the symbol $\langle\ \rangle_r$ stands for the radial average. This vector of primitive variables depends on the azimuthal coordinate (α), time (t) and on the axial coordinate (x), as the vector is calculated at several outlet planes at different axial locations.

7.2.2 Waves at the outlet of the combustion chamber

The waves propagating through the combustion chamber outlet ($\mathbf{W}_{cc}$) must be obtained by mode and in the frequency domain to be then propagated using the analytical models. The spatial Fourier transform is first performed,

$$\langle \hat{\mathbf{P}} \rangle_r (x, m, t) = \frac{1}{\alpha_2 - \alpha_1} \int_{\alpha_1}^{\alpha_2} \langle \mathbf{P} \rangle_r (x, \alpha, t) e^{\mathrm{i}m\alpha} d\alpha, \tag{7.1}$$

where α_1 and α_2 are the maximum and minimum azimuthal angles, as seen in figure 7.2, and m is the index indicating the mode number. Symbol ($\hat{}$) stands for the spatial Fourier transform.

The temporal Fourier transform is performed using the Welch method (Childers, 1978): the temporal signal is split into N_p segments with an overlapping region. This allows a smoothing of the signal in the frequency domain. The Fourier transform of each segment gives,

$$\langle \hat{\hat{\mathbf{P}}}^j \rangle_r (x, m, \omega) = \frac{1}{\Delta t_j} \int_{\Delta t_j} \langle \hat{\mathbf{P}} \rangle_r (x, m, t) e^{-\mathrm{i}\omega t} dt, \quad \text{for} \quad j = 1, ..., N_p, \tag{7.2}$$

where subscript j represents the considered segment of time, as shown in figure 7.3, and ($\hat{\hat{}}$) represents the double Fourier transform in space and in time. The splitting of the data and the overlapping distance is chosen automatically by the Welch method.

Once the primitive variables have been computed as a function of m and ω, the waves are calculated. Using matrix notation equation (5.26) of Chapter 5 gives

$$\mathbf{W}_{cc}^j (x, m, \omega) = [\mathcal{M}_{cc}]^{-1} \langle \hat{\hat{\mathbf{P}}}^j \rangle_r (x, m, \omega), \tag{7.3}$$

where matrix $\mathcal{M}_{cc}$ is given in equation (5.27) and is computed at the outlet plane of the combustion chamber, and $\mathbf{W}_{cc} = [w^s, w^v, w^+, w^-]_{cc}$ is the vector

of waves at the combustion chamber (cc) outlet plane as seen in figure 7.2. The operation is performed for each segment of the Welch method as shown in figure 7.3. Note that the matrix $\mathcal{M}$ depends on m and ω, as seen in Chapter 5, but also on x as it is calculated for each outlet plane of figure 7.2.

This last operation is, however, unable to distinguish hydrodynamic pressure fluctuations (travelling at the convective speed) and acoustic fluctuations (travelling at the speed of sound with respect to the mean flow). This difference should be made as the vorticity levels at the outlet of the combustion chamber are expected to be large and can have a significant impact on the acoustic field computed. To eliminate the hydrodynamic pressure fluctuations from the acoustic ones, the correlation between the several outlet planes (at different x locations) is computed, taking into account the different propagation velocities in order to keep only the fluctuations traveling at the considered speed. For the acoustic wave this is written as,

$$\langle w_{cc}^{+j} \rangle_x(m,\omega) = \frac{1}{N_x} \sum_{i=1}^{N_x} \left[w_{cc}^{+j}(x_i,m,\omega) \exp\left(ik_x^+ x_i\right) \right], \tag{7.4}$$

where N_x is the number of planes at the outlet, where the axial location is x_i, and k_x^+ is the axial component of the downstream propagating acoustic wave. In matrix notation this is written as,

$$\langle \mathbf{W}_{cc}^{j} \rangle_x(m,\omega) = \frac{1}{N_x} \sum_{j=1}^{N_x} \left[\mathcal{T}(x,m,\omega) \right] \mathbf{W}_{cc}^{j}(m,\omega), \tag{7.5}$$

where matrix $\mathcal{T}$ is given in equation. (5.45) in which the diagonal terms are the phase-shift of the waves.

Finally, the waves at the outlet plane of the combustion chamber are obtained by averaging the different portions considered in the Welch method,

$$\langle \mathbf{W}_{cc} \rangle_x(m,\omega) = \sqrt{\sum_{j=1}^{N_p} \left[\langle \mathbf{W}_{cc}^{j} \rangle_x(m,\omega) \right]^2}. \tag{7.6}$$

Note that the phase information is lost in this operation. The smoothed spectra, however, are only used to obtain the waves at the outlet of the combustion chamber. To compute the propagation of waves through the turbine stages, the different portions of the Welch method are considered and are only smoothed at the outlet of the complete turbine as seen in figure 7.3.

7.2.3 Transmission through the turbine stages

Using the analytical method of Chapter 5, the waves obtained at the outlet plane of the combustion chamber can be propagated through the turbine stages. This propagation is performed individually for each of the outgoing waves of the combustion chamber (acoustic, entropy and vorticity), in order to separate direct, indirect and vorticity noise.

Using equation (5.48) the waves at the outlet of the aero-engine are given by,

$$\langle \widetilde{\mathbf{W}}^j_{out} \rangle_x(m,\omega) = [\mathcal{A}_{out}]^{-1} [\mathcal{A}_{in}] \cdot \langle \widetilde{\mathbf{W}}^j_{cc} \rangle(m,\omega), \tag{7.7}$$

where matrix $[\mathcal{A}_{out}]$ and $[\mathcal{A}_{in}]$ are calculated using the method described in Chapter 5. The $\widetilde{\ }$ sign indicates that the upstream-propagating acoustic waves have been permuted between the inlet and the outlet of the turbine in order to correctly impose the boundary conditions: vector $\langle \widetilde{\mathbf{W}}^j_{cc} \rangle(m,\omega) = [w^s_{cc}, w^v_{cc}, w^+_{cc}, w^-_{out}]$ is therefore the vector of incoming waves as explained in chapter 5, and the upstream-propagating acoustic wave at the outlet (unknown) is replaced with the upstream-propagating acoustic wave at the outlet of the aero-engine (incoming). Vector $\langle \widetilde{\mathbf{W}}^j_{out} \rangle_x(m,\omega) = [w^s_{out}, w^v_{out}, w^+_{out}, w^-_{cc}]$ therefore contains only the outgoing waves (including the upstream-propagating acoustic wave at the combustion chamber). Chapter 5 explains the methodology for obtaining $[\mathcal{A}]$,in which the compact assumption is made for each blade row: first, the jump relation matrix $[\mathcal{E}]$ is computed for each stage (5.33), and then matrix $[\mathcal{M}]$, relating the primitive variables with the wave vector. Equation (5.47) is then used and finally the matrix components permuted to correctly impose the boundary conditions. Matrix $[\mathcal{A}_{out}]$ and $[\mathcal{A}_{in}]$ depend therefore on the velocity triangles of each stator and rotor blade. The data from the turbine needed to solve the propagation is explained in Chapter 5: the velocity triangle (Mach number M and flow angle θ) and the specific heat ratio, γ, and sound speed, c, are needed at the inlet (left) and outlet (right) of each turbine row, as the value of the load factor ($\psi = -\Delta h_t/U^2$) and the compression ratio ($\Pi = p_{t2}/p_{t1}$) of the row and the rotating speed (U) of the row (for the rotor). Some geometrical parameters are also required: the hub and shroud radius of the row and the distance between rows. Table 7.1 presents an example of the input data needed for the turbine stages of Chapter 6.

For the transmission of waves the upstream propagating acoustic wave

```
2             ! Number of rows.

ROW 1
-----------------------------------------------------------------
0.1622        ! Left Mach
-0.00566      ! Left theta (in degrees)
1.3           ! Left gamma
799           ! Left sound speed (m/s)
0.6614        ! Right Mach
-71.83        ! Right theta
1.3           ! Right gamma
772.54        ! Right sound speed
0.0           ! Psi -- load factor (-\Delta h_t / U^2 )
1.0           ! Pi  -- compression ratio (Pt2/Pt1)
0.0           ! Rotating speed (m/s)
220.d-3       ! Outlet hub radius
280.d-3       ! Outlet shroud radius
0.06          ! Lx  --> Distance with the next row (in meters)

ROW 2
-----------------------------------------------------------------
0.6614        ! Left Mach
-71.83        ! Left theta
1.32          ! Left gamma
772.54        ! Left sound speed
0.3124        ! Right Mach
-40.67        ! Right theta
1.3           ! Right gamma
762.85        ! Right sound speed
0.6903        ! Psi
0.7021        ! Pi
-500.0        ! Rotating speed
220.d-3       ! Outlet hub radius
280.d-3       ! Outlet shroud radius
0.05          ! Lx  --> Distance with the next row
```

Table 7.1 – *Example of an input_turbine.dat file.*

at the outlet of the turbine has to be imposed. For this application a non-reflecting boundary is considered and the wave is simply set to zero. For a better approximation of this reflection coefficient, the one-dimensional non-compact method explained in Chapter 3 could be applied to the outlet nozzle of the aero-engine.

The different segments of the Welch method are finally averaged to obtain the outgoing waves at the outlet of the aero-engine:

$$\langle \widetilde{\mathbf{W}_{out}} \rangle_x(m,\omega) = \sqrt{\sum_{j=1}^{N_p} \left[\langle \widetilde{\mathbf{W}^j_{out}} \rangle_x(m,\omega) \right]^2}. \tag{7.8}$$

7.2.4 Acoustic power computation

Once the acoustic waves at the outlet $\mathbf{W}_{out}$ (due to acoustic, entropy and vorticity waves in the combustion chamber) are obtained at the outlet of the turbine stages, the acoustic power at the outlet ($\mathscr{P}$) is finally computed using the Bretherton and Garrett (1968) formula, which takes into account the convective terms,

$$\mathscr{P}(m,\omega)_{out} = \left[(M\cos\theta + \cos\nu)\left(1 + M\cos\left(\theta - \nu\right)\right) \right]_{out} \left(w^+_{out}\right)^2 \left(\gamma p c A\right)_{out}, \tag{7.9}$$

which measures the outgoing acoustic power per propagating mode and was used by Cumpsty and Marble (1977). In this equation w^+_{out} is the downstream-propagating acoustic wave at the outlet of the turbine (obtained in equation (7.8)), M is the Mach number, θ the flow angle (both evaluated at the outlet of the aero-engine), ν is the angle of the wave vector (see figure 5.1), p and c are the mean pressure and sound-speed of the flow, γ is the ratio of specific heat capacity and A is the section of the turbine outlet.

Chapter 8

Application to an aero-engine

In this chapter the CHORUS methodology presented in Chapter 7 is applied to a real state-of-the-art aero-engine. The procedure described in Chapter 7 is used, performing a LES simulation of the combustion chamber only and applying the analytical methods of Chapter 5 for the propagation of the waves through the turbine. Since no experimental data exists on the considered engine, no comparison is possible, and the objectives of this chapter will be limited to illustrating an example of an application of the CHORUS methodology to a real industrial case.

8.1 LES of the combustion chamber

The combustion chamber considered, computed first by Jauré (2012), is shown in figure 8.1. The engine is separately fed with hot pressurised air from the compressor stages through the air inlet, and with kerosene through the fuel duct. The high pressure stator blade at the outlet of the combustion chamber is choked and is replaced by an equivalent section nozzle in order to simplify the simulation and respect the outlet impedance: using the nozzle the geometry and the mesh are considerably simplified. Since the nozzle is choked (just as the high pressure stator blade would be in the real application), the combustion chamber is highly pressurised and the outlet boundary condition is correctly mimicked.

The combustion chamber is composed of 18 sectors, but only one of these

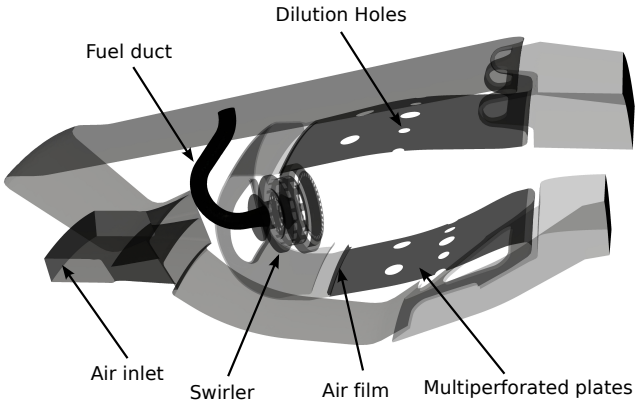

Figure 8.1 – *Combustion chamber studied.*

is computed here to reduce the computational cost. This is a common procedure when performing LES of reactive combustion chambers, and only a few recent studies have been carried out with a full 360° configuration (Staffelbach et al., 2009; Wolf et al., 2009). From a combustion noise computation point of view, however, the acoustic, entropy and vorticity waves have to be obtained for all the modes in the combustion chamber, and this can only be done when performing a 360° computation. For this reason, the modes calculated in this application will be the plane mode ($m = 0$) and all multiples of the periodicity (18). As seen in Chapter 5, acoustic waves propagating with these oblique modes are evanescent at low frequencies, and therefore only a few modes are necessary. It should be noted, however, that the first circumferential mode of the full annular combustion chamber ($m = \pm 1$) as well as all modes between $m = 1$ and $m < 18$ cannot be computed using a mono-sector configuration and are therefore neglected in this study.

In the real engine the fuel is injected as a liquid through the fuel duct. The LES simulation, however, is mono-phasic and the gas fuel is therefore injected directly into the swirler, where the liquid film is supposed to atomise and evaporate. This simplification can have a significant impact on the numerical results, as explained in Section 7.1, but reduces the complexity of the numerical set-up significantly.

The numerical parameters of the LES simulation are summarised in ta-

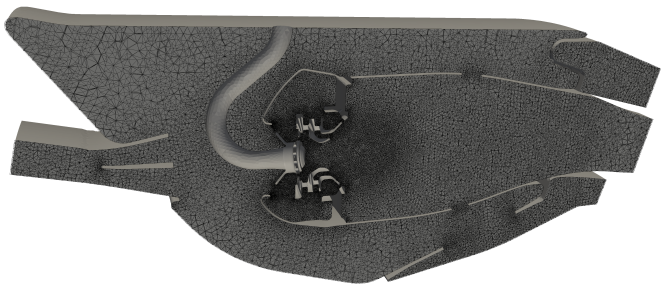

Figure 8.2 – *Mesh used for the LES of the combustion chamber.*

Parameter	value
Number of cells	8.749.998
Number of nodes	1.557.473
Smallest cell volume	$3.08 \cdot 10^{-13}\ m^3$
Fixed time step (CFL <0.7)	$9 \cdot 10^{-8}\ s$
Numerical Scheme	TTGC
Sub-grid scale model	Smagorinsky model
Artificial viscosity model	Colin Sensor (ϵ_2 = 0.2 & ϵ_4 = 0.01)
Flame model	Thickened flame model
Chemistry	Two-step BFER
Number of species	6
Number of reactions	2

Table 8.1 – *Parameters for the LES of the combustion chamber.*

ble 8.1. The two-step chemistry of Franzelli et al. (2010), known as the BFER model, is used here for the kerosene injected into the engine. The two reactions are

$$F + 10O_2 \longrightarrow 10CO + 10H_2O, \tag{8.1a}$$

$$CO + \frac{1}{2}O_2 \longleftrightarrow CO_2, \tag{8.1b}$$

where only the second one is reversible. The forward reaction rates are given by the Arrhenius law with a correction term, as explained in Section 7.1, to account for the complex chemistry neglected. This chemistry is applied in

the LES using a flame thickening model as explained in Section 7.1, where the flame is thickened dynamically (Légier et al., 2000). The time step is fixed with a CFL number less than 0.7, and a TTGC numerical scheme (Donéa et al., 1987, 2000; Lamarque, 2007) is used, which is third-order in space and fourth-order in time and has been shown to have very little dissipation and dispersion. These centered schemes present non-physical oscillations which should be eliminated. The use of filters is a common procedure but unfeasible due to the large computational cost on unstructured meshes. For this reason low levels of artificial viscosity based on the Jameson et al. (1981) sensor are used to avoid these numerical issues (Colin, 2000).

8.1.1 Flow description

Though the flow description of this combustion chamber can be found in previous work (Jauré, 2012), a basic description will be given here focusing on the unsteadiness of the flow and on the generation of direct and indirect noise.

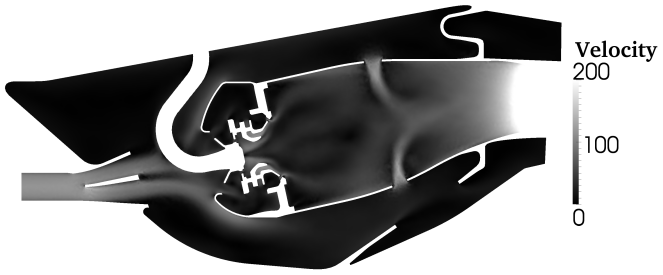

Figure 8.3 – *Mean velocity* $[m/s]$ *of a cross-section of the combustion chamber.*

Figure 8.3 shows the mean velocity magnitude and figure 8.4(a) shows the mean temperature in the combustion chamber with the central recirculation zone (CRZ). The flow enters the flame tube through the swirler, where it is mixed with kerosene. The objective of the swirler is to generate a large tangential velocity (with respect to the swirler's axis) which is the cause of the CRZ shown in figure 8.4(a). The objective of this recirculation zone is to make the hot burnt gases recirculate close to the unburnt region in order to ignite the fresh mixture. Figure 8.5 shows an instantaneous field

of heat release of the flame due to the combination of the two reactions of equation 8.1.

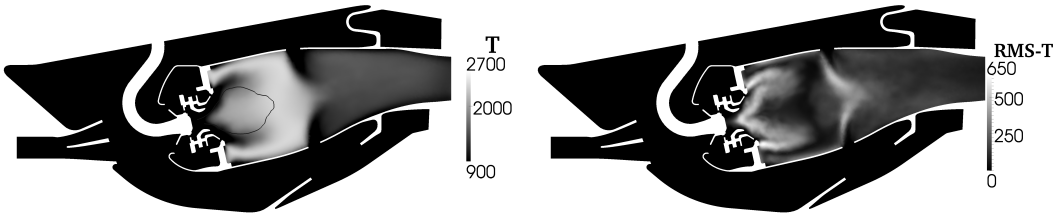

(a) Mean temperature $[K]$. (b) RMS temperature $[K]$.

Figure 8.4 – *Temperature fields of a cross-section of the combustion chamber* $[K]$*. A solid black line on (a) shows the central recirculation zone.*

The swirling of the flow generates large turbulence levels at the same time, which enhance mixing and combustion. These turbulent eddies interact with the flame generating an unsteady heat release and originating in this way acoustic and entropy waves, which are finally responsible for combustion noise. Figure 8.4(b) shows the RMS values of the temperature field. It can be seen that large fluctuations exist in the flame region, which are linked to the generation of entropy waves. The contribution of the dilution holes and flow mixing is also of great importance, as illustrated in figure 8.4(b). It can be seen that the fresh air injected into the main flame tube through the dilution holes generates large RMS temperature values, due to the large temperature fluctuations between fresh air from the compressor and hot air from the flame.

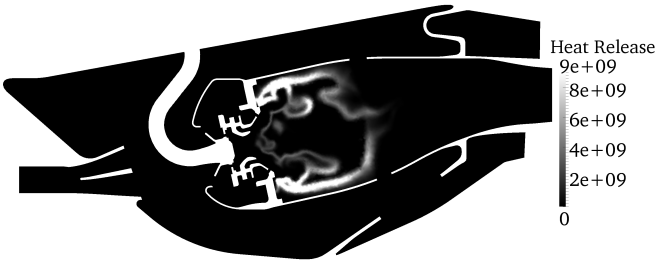

Figure 8.5 – *Instantaneous field of heat release.*

Figure 8.6 shows an instantaneous field of the temperature fluctuation in the combustion chamber. This figure illustrates the generation of entropy spots by two mechanisms: the unsteadiness of the flame and the turbulent mixing downstream of the flame in the region of the dilution holes. The acceleration of these entropy spots through turbine stages is responsible for indirect combustion noise.

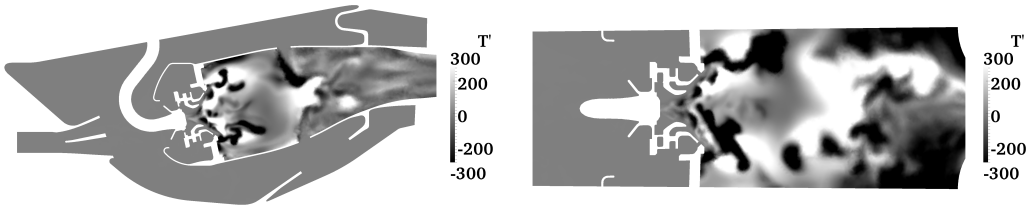

(a) Side view (b) Top view

Figure 8.6 – *Instantaneous field of the temperature fluctuation* $[K]$.

To avoid perturbations from the downstream boundary condition, the outlet planes where the acoustic, entropy and vorticity waves are extracted are located one chord upstream from the high-pressure turbine stator blade, as shown in figure 7.2.

Total samples	Total time	Number of segments (N_p)	Samples in a segment	Overlap between segments
5160	232.2 ms	968	322	5

Table 8.2 – *Parameters used in the CHORUS post-processing.*

8.2 Waves in the combustion chamber

The spectra of the waves at the outlet of the combustion chamber are obtained using the CHORUS post-processing tool and are plotted in figure 8.7. The parameters used in CHORUS are summarised in table 8.2. As only one sector has been computed, only the plane wave ($m = 0$) is relevant. However,

to illustrate the capability of CHORUS to compute circumferential modes, the first circumferential mode (m = 18) has also been plotted.

The acoustic waves (figures 8.7(a) and 8.7(b)) are mainly longitudinal, as the circumferential mode does not propagate under the cut-off frequency, which is calculated as explained in Section 5.2 and in this case gives $f_{cut} \approx 8600$ Hz for m = 18, which coincides with the peak value of the circumferential mode shown in figures 8.7(a) and 8.7(b). The main source of noise in this mono-sector configuration will therefore be the plane mode. It should be noted that the first circumferential mode of the complete 360° configuration (which is not computed here as explained above) has a cut-off frequency of $f_{cut} \approx 480$ Hz.

Figure 8.7 shows that the waves generated in the combustion chamber are broadband. Indeed, as the combustion chamber is stable, no thermoacoustic frequency peak appears (except the one related to the cut-off frequency), showing that no thermoacoustic instability occurs. The unsteady heat release generating the waves (acoustic, entropy and vorticity) at the outlet is therefore due to the interaction of the flame with turbulence, and not to a flame-acoustics coupling.

Using a simple 1D cold flame, Leyko et al. (2009) showed, as explained in Section 4.5, that the ratio between entropy and acoustic waves generated by the flame can be estimated to be of the order of $(1+M)/M$, which for small Mach numbers is approximately $1/M$. This is the case for a very simple compact analytical flames. For the real application considered here, the dimensionless entropy wave (w^s) can be seen to be an order of magnitude larger than the dimensionless acoustic wave (w^+).

8.3 Direct and indirect combustion noise

The CHORUS post-processing tool propagates the acoustic, entropy and vorticity waves computed in the previous section through the turbine stages. Results are shown in figure 8.8, where the three sources of combustion noise (direct, indirect and vorticity noise) are considered independently. Figure 8.8 gives the total acoustic power radiated at the engine outlet. The value of the reduced frequency Ω = 0.1 is also plotted, based on the chord of the first stator blade of the turbine.

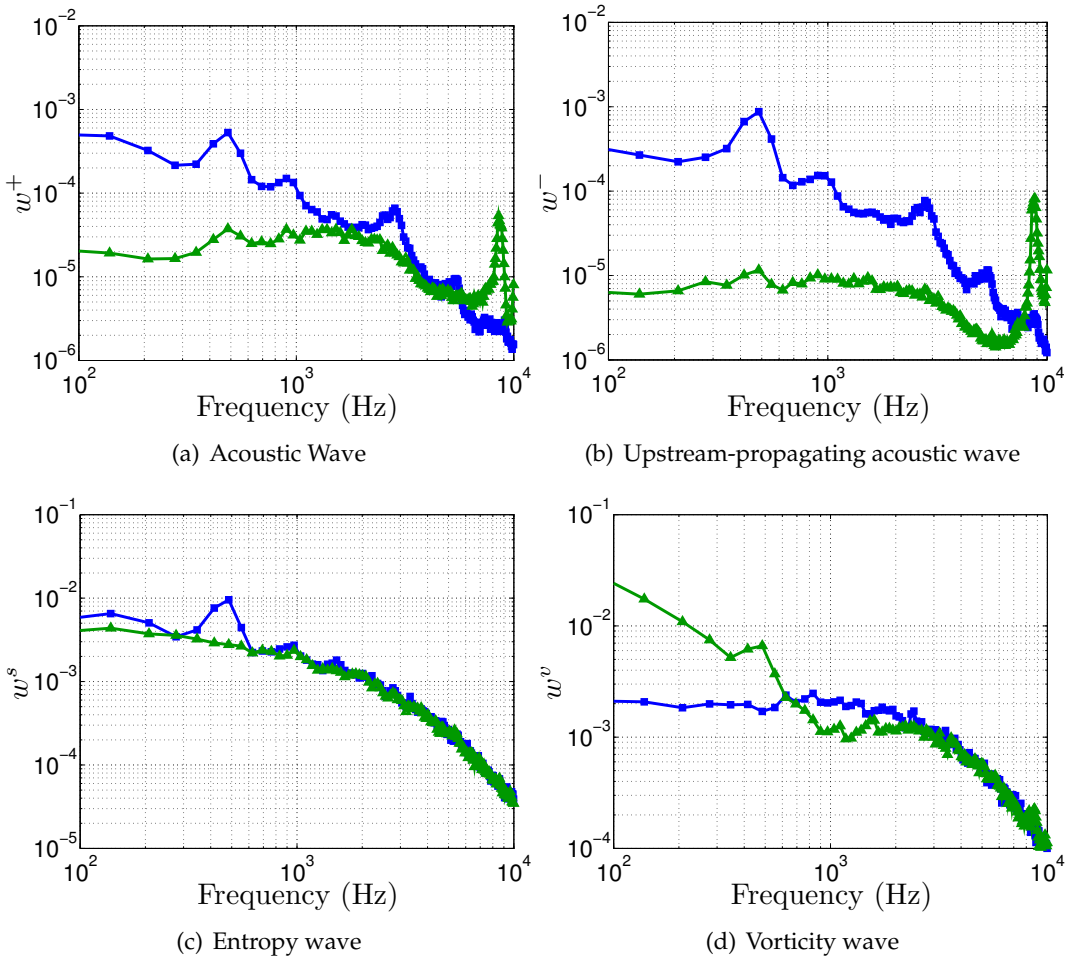

(a) Acoustic Wave (b) Upstream-propagating acoustic wave

(c) Entropy wave (d) Vorticity wave

Figure 8.7 – *Spectra of the waves at the outlet of the combustion chamber for the plane mode (■) and for the first circumferential mode of the sector, m = 18 (▲).*

CHORUS can also be used to compute the transfer functions of the acoustic and entropy waves through the considered turbine stages. These transfer functions represent the acoustic wave at the outlet of the engine generated for a unitary acoustic wave at the inlet of the turbine (for T_{aa}) and per unitary entropy wave at the inlet (T_{sa}). Figure 8.9 shows the module of these functions, computed using the analytical method of Chapter 5 and considering only plane modes. It should be noted that the transfer functions are computed using the compact assumption for each blade, and the frequency dependence is due only to the spacing between blades.

In this case, just as in the one discussed by Leyko (2010), indirect noise is

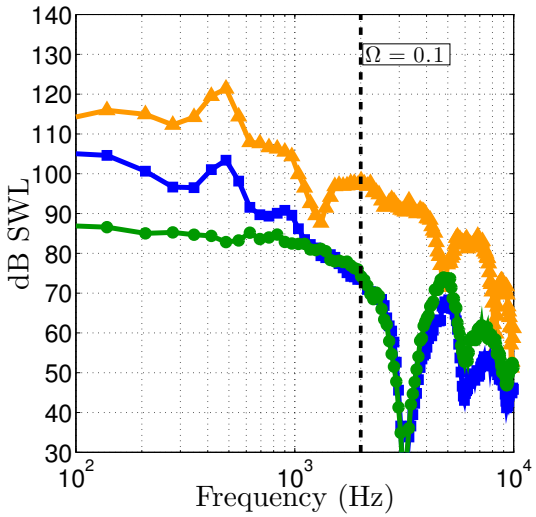

Figure 8.8 – *Combustion noise at the outlet of the turbine stages. Indirect noise (▲), direct noise (■) and vorticity noise (•). No attenuation considered.*

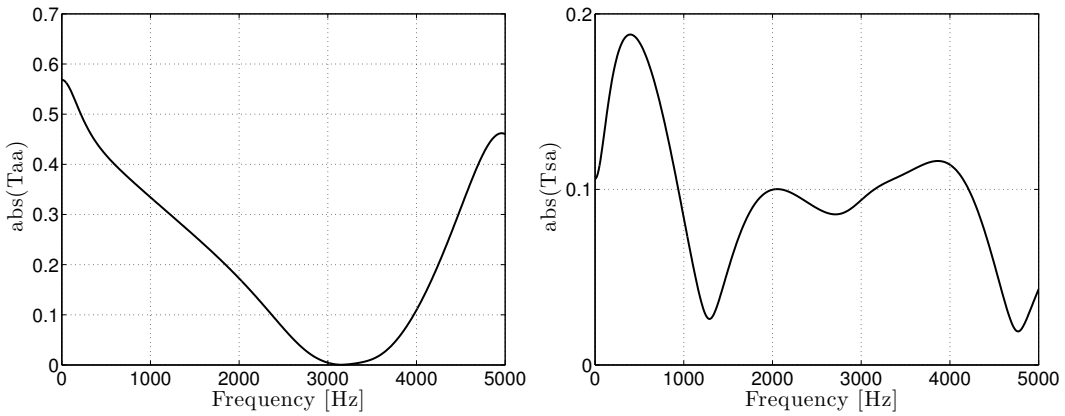

(a) Acoustic transfer function (b) Entropy transfer function

Figure 8.9 – *Transfer function of the complete turbine considered for the plane mode.*

larger than direct noise and vorticity noise is almost negligible. However, the attenuation of the plane entropy wave while propagating through the turbine stages (due to the deformation of the wave by the mean flow, as seen in Chapter 6) is likely to have an impact on the entropy noise levels. Figure 8.10 shows the same results but takes into consideration the attenuation functions of Chapter 6 applied to each turbine row. It should be noted that the attenuation model takes into account only the deformation of the entropy wave and does not consider turbulence, mixing or heat diffusion.

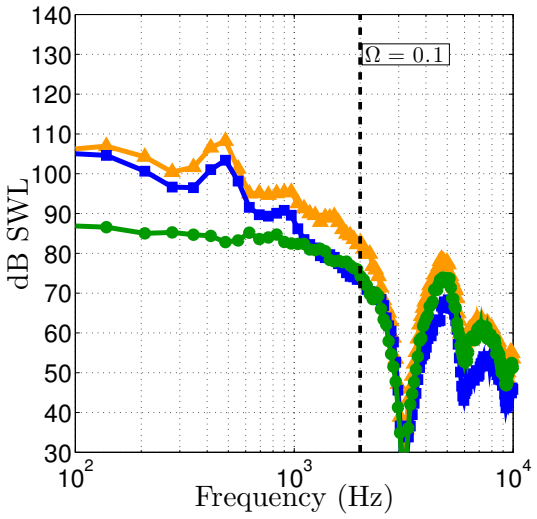

Figure 8.10 – *Combustion noise at the outlet of the turbine stages. Indirect noise (▲), direct noise (■) and vorticity noise (•) considering the attenuation functions for the entropy wave.*

Figure 8.11 shows the evolution of the total acoustic power (in dB) generated by each mechanism as more turbine rows are considered. Direct noise is found to decrease around 1.5dB for each row added (3.0dB for each stage). This is due to the shielding effect: the acoustic transmission coefficients are lower than unity and therefore prevent noise from propagating to the outlet. When considering no attenuation of the entropy wave (figure 8.11(a)), indirect noise is found to increase as more rows are added in the configuration (as they each generate more and more indirect noise) up to a point where it starts to decrease, due to the shielding effect of the last added turbine row for the noise generated upstream. However, when considering the attenuation model (figure 8.11(b)), the indirect noise decreases at almost the same rate as the direct noise, as turbine rows added downstream generate less indirect noise (due to the entropy wave attenuation) but contribute to the shielding effect of the indirect noise generated upstream.

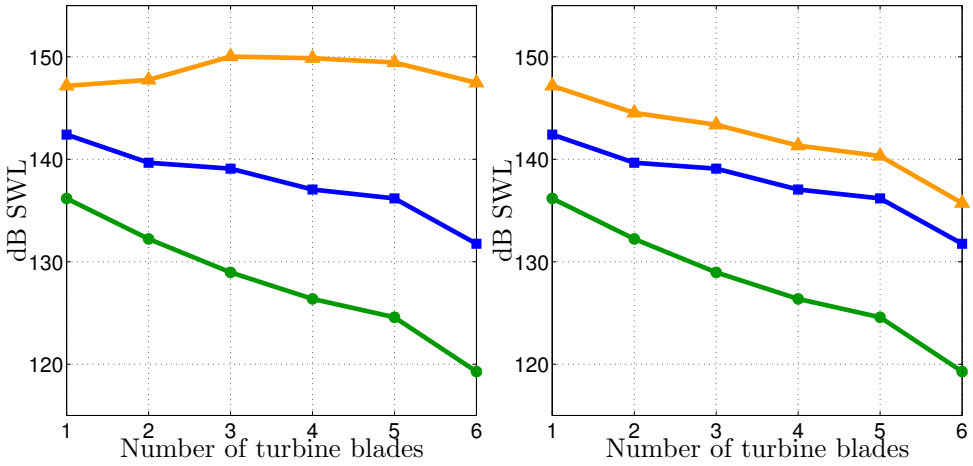

(a) No attenuation model (b) With attenuation model

Figure 8.11 – *Noise integrated over all frequencies at each turbine stage. Indirect noise (▲), direct noise (■) and vorticity noise (●).*

Conclusions

To compute the combustion noise generated by an aero-engine, the LES of the combustion chamber has been combined with the analytical methods of Part II to propagate the acoustic and entropy waves. The post-processing of the LES fields gives both the waves at the outlet of the combustion chamber and the noise generated at the outlet of the turbine for each mechanism.

The main advantage of this method is that it avoids a complete computation of the combustion chamber with the turbine stages. Indeed, the method accounts for the generation of indirect noise and for the reflection and attenuation of acoustic waves when propagating through turbine stages, using the analytical propagation methods for the turbine blades. This method has other advantages: while a complete numerical result will give the total noise at the outlet, the analytical method decouples direct and indirect combustion noise and therefore provides more insight on which noise mechanism is stronger.

The method has been successfully applied to several combustion chambers, one of which is explained in Chapter 8. Results show the importance of indirect noise on the global noise computed and at the same time the influence of the deformation of the entropy wave when passing through the stator and rotor blades on the indirect noise levels.

General conclusions and perspectives

The increase of air traffic and the increasingly restrictive international regulations on aircraft noise has led industry and research groups to study the generation of noise by the combustion chamber. The prediction of combustion noise is a challeging task, as it requires on the one hand accurately solving (numerically for example) the noise sources in the combustion domain, and on the other hand, accurately propagating these sources through the outlet of the combustion chamber: the turbine stages. This work focuses mainly on this last point in order to build up a low-order model for the propagation of waves through the turbine stages.

Part I presents a study of the propagation of waves through quasi-1D nozzles, extending previous solutions based on low-frequency assumptions, to non-compact frequencies. This analysis shows the importance of the frequency dependence on the propagation of waves. The non-compact method was validated with numerical simulations of the linearised Euler equations and with experimental data, showing that the method is able to accurately predict both the reflection and the transmission coefficients of quasi-1D nozzles. In Part II, the 2D compact method of Cumpsty and Marble (1977) is studied and validated using numerical simulations of a complete turbine stage. The deformation of the entropy wave is also studied and the attenuation induced modelled as it is found to have a large effect when combining several turbine stages. These analytical methods used to compute the propagation of waves allow a simpler and faster prediction of the propagation of waves through non-homogeneous flows, in order to reduce the computational costs of the combustion noise simulation.

Part III presents the complete methodology for the prediction of com-

bustion generated noise. The method is based on a LES of the combustion chamber which accurately computes the noise sources. The acoustic, entropy and vorticity waves are extracted from the simulation and post-processed, propagating them through the turbine stages using the low-order models previously explained.

Combustion noise has only recently attracted the attention of the research community, and for this reason there is large room for improvement of methods and the development of new techniques for noise reduction. The quasi-1D non-compact method presented in Chapter 3 can be extended to a 2D configuration, extending the compact model of Cumpsty and Marble (1977) explained in Chapter 5 to non-compact frequencies. From a numerical point of view, though the LES methodology and the combustion models used have been validated in multiple applications, their use for combustion noise prediction should be analysed. The combustion chamber computed in this work consists of a single sector, neglecting therefore azimuthal modes. This should also be studied as, even if higher order modes do not propagate at low frequencies, it is expected that at least the first azimuthal mode may propagate and would generate noise in the frequency range of combustion noise.

A validation of the developed methods using experimental measurements is still required. In this context, two projects (RECORD and TEENI, under the 7th EU Framework Programme) are expected to generate a large database of experimental measurements to validate the numerical tools and the low-order models.

Bibliography

M. Abramowitz and I. Stegun. *Handbook of mathematical functions with formulas, graphs, and mathematical tables*, volume 55. Dover publications, 1964. 32

ACARE. http://www.acare4europe.com/. 2013. 2

C. Bailly, C. Bogey, and S. Candel. Modelling of sound generation by turbulent reacting flows. *International Journal of Aeroacoustics*, 9(4):461–490, 2010. 9

F. Bake, C. Richter, B. Muhlbauer, N. Kings, I.Rohle, F.Thiele, and B.Noll. The entropy wave generator (ewg): a reference case on entropy noise. *J. Sound Vib.*, pages 574–598, 2009. 7, 17, 71

G. K. Batchelor. *An introduction to fluid dynamics*. Cambridge University Press, Cambridge, 1988. 22

W. Bell and B. Zinn. The prediction of three-dimensional liquid-propellant rocket nozzles admittances. Technical Report CR-121129, NASA, 1973. 89

W. Bell, B. Daniel, and B. Zinn. Experimental and theoretical determination of the admittances of a family of nozzles subjected to axial instabilities. *J. Sound Vib.*, 30(2):179–190, 1973. vii, 55, 69, 70

S. Blanes, F. Casas, J. A. Otero, and J. Ros. The magnus expansion and some of its applications. *Physics Reports*, 470(5-6):151–238, January 2009. 37, 41, 43

A. W. Bloy. The pressure waves produced by the convection of temperature disturbances in high subsonic nozzle flows. *Journal of Fluid Mechanics*, 94(03):465–475, Oct. 1979. doi: 10.1017/S0022112079001130. 37

F. P. Bretherton and C. J. R. Garrett. Wavetrains in inhomogeneous moving media. *Proceedings of the Royal Society of London*, 302(1471):529–554, 1968. 157

S. Buis, A. Piacentini, and D. Déclat. Palm: A computational framework for assembling high performance computing applications. *Concurrency and Computation: Practice and Experience*, 18(2):231–245, February 2006. 113

T. D. Butler and P. J. O'Rourke. A numerical method for two-dimensional unsteady reacting flows. *Proc. Combust. Inst.* , 16(1):1503 – 1515, 1977. 148

L. Campos. On longitudinal acoustic propagation in convergent and divergent nozzle flows. *Journal of Sound and Vibration*, 117(1):131–151, 1987. ISSN 0022-460X. 18

S. Candel. Acoustic transmission and reflection by a shear discontinuity separating hot and cold regions. *J. Sound Vib.*, 24:87–91, 1972a. 8

S. Candel. *Analytical studies of some acoustic problems of jet engines*. PhD thesis, California Institute of Technology, 1972b. 17

S. Candel and T. Poinsot. Interactions between acoustics and combustion. In *Proceedings of the institute of acoustics*, volume 10, pages 103–153, 1988. 18

F. Casas. Sufficient conditions for the convergence of the Magnus expansion. *Journal of Physics A: Mathematical and Theoretical*, 40(50):15001–15017, Dec. 2007. ISSN 1751-8113. doi: 10.1088/1751-8113/40/50/006. 43

D. G. Childers. *Modern Spectrum Analysis*. IEEE Press, 1978. 153

H. . H. Chiu and M. Summerfield. Theory of combustion noise. *Acta Astronautica*, 1:967–984, 1974. 4, 7

H. H. Chiu, H. Y. Kim, and E. J. Croke. Internal group combustion of liquid droplets. In *19th Symp. (Int.) on Combustion*, pages 971–980. The Combustion Institute, Pittsburgh, 1982. 149

O. Colin. *Simulations aux grandes échelles de la combustion turbulente prémélangée dans les statoréacteurs*. Phd thesis, INP Toulouse, 2000. 162

O. Colin, F. Ducros, D. Veynante, and T. Poinsot. A thickened flame model for large eddy simulations of turbulent premixed combustion. *Phys. Fluids* , 12(7):1843–1863, 2000. 148

E. Collado. *Impact of the unsteady aerothermal environment on the turbine blades temperature*. PhD thesis, Université de Toulouse - Institut National Polytechnique de Toulouse - Energétique et Transferts, 2012. PhD. 9

L. Crocco and W. A. Sirignano. Behavioir of Supercritical Nozzles under Three-Dimensional Oscillatory Conditions. *AGARD*, (117), 1967. 70

F. E. C. Culick. Combustion instabilities in liquid-fueled propulsion systems-an overview. In *AGARD 72B PEP meeting*, 1988. 18

N. A. Cumpsty and F. E. Marble. The interaction of entropy fluctuations with turbine blade rows; a mechanism of turbojet engine noise. *Proc. R. Soc. Lond. A* , 357:323–344, 1977. 4, 11, 47, 90, 93, 95, 101, 102, 139, 140, 145, 147, 157, 173, 174

J. Donéa, L. Quartapelle, and V. Selmin. An analysis of time discretization in the finite element solution of hyperbolic problems. *J. Comput. Phys.* , 70:463–499, 1987. 162

J. Donéa, B. Roig, and A. Huerta. High-order accurate time-stepping schemes for convection-diffusion problems. *Comput. Methods Appl. Mech. Eng.* , 182:249–275, 2000. 162

A. Dowling and S. Stow. Acoustic analysis of gas turbine combustors. *Journal of Propulsion and Power*, 19(5):751–764, 2003. ISSN 0748-4658. 17

A. Dowling, G. J. Bloxsidge, N. Hooper, and P. J. Langhorne. Active control of reheat buzz. *AIAA Journal*, 26(7):783–790, July 1988. ISSN 0001-1452. doi: 10.2514/3.9970. 6

A. P. Dowling. The calculation of thermoacoustic oscillations. *J. Sound Vib.*, 180(4):557–581, 1995. 18

A. P. Dowling. Nonlinear self-excited oscillations of a ducted flame. *J. Fluid Mech.* , 346:271–290, 1997. 17

I. Duran and S. Moreau. Analytical and numerical study of the entropy wave generator experiment on indirect combustion noise. In *17th AIAA/CEAS Aeroacoustics Conference - AIAA-2011-2829*, Portland, Oregon, 2011. 188

I. Duran and S. Moreau. Study of the attenuation of waves propagating through fixed and rotating turbine blades. In *18th AIAA/CEAS Aeroacoustics Conference (33rd AIAA Aeroacoustics Conference)*, number AIAA2012-2133 paper, Colorado Springs, USA, June 4-6 2012. 105, 188

I. Duran and S. Moreau. Numerical simulation of acoustic and entropy waves propagating through turbine blades. In *19th AIAA/CEAS Aeroacoustics Conference (34th AIAA Aeroacoustics Conference)*, number AIAA2013-2102 paper, Berlin, Germany, May 27-29 2013a. 188

I. Duran and S. Moreau. Solution of the quasi one-dimensional linearized Euler equations using flow invariants and the Magnus expansion. *Journal of Fluid Mechanics*, 723:190–231, May 2013b. 187

I. Duran, M. Leyko, S. Moreau, F. Nicoud, and T. Poinsot. Computing combustion noise by combining Large Eddy Simulations with analytical models for the propagation of waves through turbine blades. In *3rd Colloquium INCA*, Toulouse (France), November 17-18 2011. 188

I. Duran, M. Leyko, S. Moreau, F. Nicoud, and T. Poinsot. Computing combustion noise by combining Large Eddy Simulations with analytical models for the propagation of waves through turbine blades. *Comptes Rendus de l'Académie des Sciences - Mécanique*, 341(1-2):131–140, January 2013a. 187

I. Duran, S. Moreau, F. Nicoud, T. Livebardon, E. Bouty, and T. Poinsot. Combustion noise in modern aero-engines. *AerospaceLab*, submitted, 2013b. 187

I. Duran, S. Moreau, and T. Poinsot. Analytical and numerical study of combustion noise through a subsonic nozzle. *AIAA Journal*, 51(1):42–52, 2013c. 18, 37, 187

I. Duran, S. Moreau, and T. Poinsot. A new analytical method to compute nozzle impedances at all frequencies. In *EUROMECH Colloquium 546 – Combustion Dynamics and Combustion Noise*, Villa Vigoni, Menaggio, Italy, May 13-16 2013d. 188

EIA. http://www.eia.gov. 2013. v, 1, 2

B. Franzelli. *Impact of the chemical description on direct numerical simulations and Large Eddy Simulations of turbulent combustion in industrial*

aero-engines - TH/CFD/11/101. PhD thesis, Université de Toulouse, France - MeGeP Dynamique des Fluides, 2011. phd. 149

B. Franzelli, E. Riber, M. Sanjosé, and T. Poinsot. A two-step chemical scheme for Large-Eddy Simulation of kerosene-air flames. *Combust. Flame* , 157(7):1364–1373, 2010. 149, 161

A. Giauque, M. Huet, and F. Clero. Analytical analysis of indirect combustion noise in subcritical nozzles. *J. Eng. Gas Turbines Power*, 134(11): 111202, 2012. 33, 61

L. Gicquel, G. Staffelbach, and T. Poinsot. Large Eddy Simulations of gaseous flames in gas turbine combustion chambers. *Progress in Energy and Combustion Science*, 38(6):782–817, 2012. ISSN 03601285. doi: 10.1016/j.pecs.2012.04.004. 20

C. S. Goh and A. S. Morgans. Phase prediction of the response of choked nozzles to entropy and acoustic disturbances. *Journal of Sound and Vibration*, pages 1–15, June 2011a. ISSN 0022460X. doi: 10.1016/j.jsv.2011.05.016. vii, 18, 35, 40, 49, 55, 63, 64, 65, 81

C. S. Goh and A. S. Morgans. The effect of entropy wave dissipation and dispersion on thermoacoustic instability in a model combustor. In *17th AIAA/CEAS Aeroacoustics Conference - AIAA-2011-2914*, Portland, 2011b. 57

V. Granet, O. Vermorel, T. Leonard, L. Gicquel, , and T. Poinsot. Comparison of nonreflecting outlet boundary conditions for compressible solvers on unstructured grids. *AIAA Journal*, 48(10):2348–2364, 2010. 112, 115

E. Gullaud, S. Mendez, C. Sensiau, F. Nicoud, and T. Poinsot. Effect of multiperforated plates on the acoustic modes in combustors. *C. R. Acad. Sci. Mécanique*, 337(6-7):406–414, 2009. 17

H. Hassan. Scaling of combustion generated noise. *J. Fluid Mech.* , 66: 445–453, 1974. 4

C. W. Hirt, A. Amsden, and J. L. Cook. An arbitrary lagrangian-eulerian computing method for all flow speeds. *J. Comput. Phys.* , 131(4):371–385, 1974. 111

M. S. Howe. The generation of sound by aerodynamic sources in an homogeneous steady flow. *J. Fluid Mech.* , 67(3):597–610, 1975. 7

M. S. Howe. *Acoustics of Fluid-Structure Interaction*. Cambridge University Press, 1998. 22

M. S. Howe. Indirect combustion noise. *J. Fluid Mech.* , 659:267–288, 2010. 7, 17

ICAO. http://www.icao.int. 2013. v, 2, 3

M. Ihme and H. Pitsch. On the generation of direct combustion noise in turbulent non-premixed flames. *International Journal of Aeroacoustics*, 11(1):25–78, 2012. 8, 148

M. Ihme, D. Bodony, and H. Pitsch. Towards the prediction of combustion-generated noise in non-premixed turbulent flames using large-eddy simulation. *CTR Annual Research Briefs*, pages 311–323, 2005. 8

A. Jameson, W. Schmidt, and E. Turkel. Numerical solution of the euler equations by finite volume methods using runge-kutta time stepping schemes. In A. p. 81-1259, editor, *14th Fluid and Plasma Dynamic Conference*, Palo Alto, 1981. 162

S. Jauré. *Méthodologies pour le couplage Simulation aux Grandes Echelles/Thermique en environnement massivement parallèle - TH/CFD/12/114*. PhD thesis, Université de Toulouse - Ecole doctorale : Mécanique, Energétique, Génie civil, Procédés - Dynamique des Fluides - December, 13, 2012. phd. 159, 162

S. Kaji and T. Okazaki. Propagation of sound waves through a blade row: I. analysis based on the semi-actuator disk theory. *J. Sound Vib.*, 11(3): 339–353, 1970a. 89

S. Kaji and T. Okazaki. Propagation of sound waves through a blade row: II. analysis based on acceleration potential method. *J. Sound Vib.*, 11 (3):355–375, 1970b. 89

A. R. Kerstein. A linear eddy model of turbulent scalar transport and mixing. *Combust. Sci. Tech.* , 60:391, 1988. 148

M. Kostka and H. Pitsch. Direct approach to the prediction of indirect combustion noise. *Annual Research Briefs 2010*, pages 289–294, 2010. 7

S. Kotake. On combustion noise related to chemical reactions. *J. Sound Vib.*, 42:399–410, 1975. 7

C.-Y. Kuo and A. P. Dowling. Oscillations of a moderately underexpanded choked jet impinging upon a flat plate. *Journal of Fluid Mechanics*, 315: 267–291, 1996. ISSN 00221120. doi: 10.1017/S002211209600242X. 49

N. Lamarque. *Schémas numériques et conditions limites pour la simulation aux grandes échelles de la combustion diphasique dans les foyers d'hélicoptère*. Phd thesis, INP Toulouse, 2007. 162

J.-P. Légier, T. Poinsot, and D. Veynante. Dynamically thickened flame LES model for premixed and non-premixed turbulent combustion. In *Proc. of the Summer Program* , pages 157–168. Center for Turbulence Research, NASA Ames/Stanford Univ., 2000. 162

M. Leyko. *Mise en oeuvre et analyse de calculs aéroacoustiques de type SGE pour la prévision du bruit de chambres de combustion aéronautiques*. Phd thesis, INP Toulouse, 2010. viii, 9, 12, 89, 90, 125, 126, 145, 166

M. Leyko, F. Nicoud, S. Moreau, and T. Poinsot. Numerical and analytical investigation of the indirect noise in a nozzle. In *Proc. of the Summer Program* , pages 343–354, Center for Turbulence Research, NASA AMES, Stanford University, USA, 2008. 7, 8, 17

M. Leyko, F. Nicoud, and T. Poinsot. Comparison of direct and indirect combustion noise mechanisms in a model combustor. *AIAA Journal*, 47 (11):2709–2716, 2009. viii, 7, 17, 28, 37, 55, 75, 76, 77, 82, 165

M. Leyko, S. Moreau, F. Nicoud, and T. Poinsot. Waves transmission and generation in turbine stages in a combustion-noise framework. In *16th AIAA/CEAS AeroAcoustics Conference*, 2010. 109, 110, 119, 120

M. Leyko, S. Moreau, F. Nicoud, and T. Poinsot. Numerical and analytical modelling of entropy noise in a supersonic nozzle with a shock. *J. Sound Vib.*, 330(16, 1):3944–3958, 2011. 7, 49

M. Leyko, I. Duran, S. Moreau, F. Nicoud, and T. Poinsot. Simulation and modelling of the waves transmission and generation in a stator blade row in a combustion-noise framework. *JSV*, submitted, 2013. 109, 116, 134, 140, 187

T. Lieuwen and V. Yang. Combustion instabilities in gas turbine engines. operational experience, fundamental mechanisms and modeling. In *AIAA Prog. in Astronautics and Aeronautics* , volume 210, 2005. 5

M. J. Lighthill. On sound generated aerodynamically. i. general theory. *Proc. R. Soc. Lond. A , Mathematical and Physical Sciences*, 211(1107): 564–587, 1952. 4, 8

A. Liñán. *Mecánica de fluidos.* Escuela Técnica Superior de Ingenieros Aeronáuticos de Madrid, 2005. 22

J. Luche. *Elaboration of reduced kinetic models of combustion. Application to a kerosene mechanism.* PhD thesis, LCSR Orleans, 2003. 149

J. Luche, M. Reuillon, J.-C. Boettner, and M. Cathonnet. Reduction of large detailed kinetic mechanisms: application to kerosene / air combustion. *Combust. Sci. Tech.* , 176:1935–1963, 2004. 149

P. Madhu and N. Kurur. Fer expansion for effective propagators and Hamiltonians in NMR. *Chemical Physics Letters*, 418(1-3):235–238, Jan. 2006. ISSN 00092614. doi: 10.1016/j.cplett.2005.10.134. 42

W. Magnus. On the exponential solution of differential equations for a linear operator. *Communications on pure and applied mathematics*, 7(4):649–673, November 1954. 41

F. E. Marble and S. Candel. Acoustic disturbances from gas nonuniformities convected through a nozzle. *J. Sound Vib.*, 55:225–243, 1977. 4, 5, 6, 10, 12, 17, 18, 19, 27, 28, 29, 30, 31, 33, 47, 48, 49, 55, 56, 64, 81, 90, 93, 96

M. Matalon and B. J. Matkowsky. Flames as gasdynamic discontinuities. *J. Fluid Mech.* , 124:239, 1982. 148

A. Mishra and D. J. Bodony. Evaluation of actuator disk theory for predicting indirect combustion noise. */JSV*, 332(4):821–838, February 2013. 109, 120

P. C. Moan and J. Niesen. Convergence of the Magnus series. Technical Report 0316, La Trobe University, 2006. 43

W. Moase, M. Brear, and C. Manzie. The forced response of choked nozzles and supersonic diffusers. *Journal of Fluid Mechanics*, 585:281–304, 2007. ISSN 0022-1120. doi: 10.1017/S0022112007006647. 18, 19, 28, 32, 33, 48, 49, 81

C. Moler. Nineteen Dubious Ways to Compute the Exponential of a Matrix, Twenty-Five Years Later. *SIAM Review*, 46(1):366, 2003. doi: 10.1137/S00361445024180. 42

C. L. Morfey. Amplification of aerodynamic noise by convected flow inhomogeneities. *J. Sound Vib.*, 31:391–397, 1973. 9

A. S. Morgans, C. S. Goh, and J. A. Dahan. The dissipation and shear dispersion of entropy waves in combustor thermoacoustics. *Journal of Fluid Mechanics*, 733 R2:1–11, 2013. 127

E. Motheau, L. Selle, T. Poinsot, and F. Nicoud. A mixed acoustic-entropy combustion instability in a realistic gas turbine. In *Proceedings of the 2012 Summer Program*, Center for Turbulence Research, NASA AMES, Stanford University, USA, June 24 to July 20 2012. 20, 57

V. R. Moureau, O. V. Vasilyev, C. Angelberger, and T. J. Poinsot. Commutation errors in Large Eddy Simulations on moving grids: Application to piston engine flows. In *Proc. of the Summer Program* , pages 157–168, Center for Turbulence Research, NASA AMES/Stanford University, USA, 2004. 111

R. S. Muir. The application of a semi-actuator disk model to sound transmission calculations in turbomachinery, part i: The single blade row. *Journal of Sound and Vibration*, 54(3):393–408, October 1977a. 89

R. S. Muir. The application of a semi-actuator disk model to sound transmission calculations in turbomachinery, part ii: Multiple blade rows. *Journal of Sound and Vibration*, 55(3):335–349, Decembre 1977b. 89

M. Muthukrishnan, W. Strahle, and D. Neale. Separation of hydrodynamic, entropy, and combustion noise in a gas turbine combustor. *AIAA Journal*, 16(4):320–327, 1978. 8, 17

W. Noh. A time dependent two space dimensional coupled eulerian lagrangian code. *Meth. Comput. Phys.*, 3, 1964. 111

O. M. Phillips. On the generation of sound by supersonic turbulent shear layers. *J. Fluid Mech.* , 9:1–28, 1960. 7

G. F. Pickett. Core engine noise due to temperature fluctuations convecting through turbine blade rows. In *2nd AIAA Aeroacoustics Conference - AIAA 1975-528*, 1975. 8, 17

A. D. Pierce. *Acoustics: an introduction to its physical principles and applications.* McGraw Hill, New York, 1981. 22

T. Poinsot and S. Lele. Boundary conditions for direct simulations of compressible viscous flows. *J. Comput. Phys.* , 101(1):104–129, 1992. doi: 10.1016/0021-9991(92)90046-2. 115

T. Poinsot and D. Veynante. *Theoretical and Numerical Combustion*. Third Edition (www.cerfacs.fr/elearning), 2011. 5, 17, 147

S. B. Pope. *Turbulent flows*. Cambridge University Press, 2000. 147

H. Posson, M. Roger, and S. Moreau. On a uniformly valid analytical rectilinear cascade response function. *Journal of Fluid Mechanics*, 663:22–52, Sept. 2010. ISSN 0022-1120. doi: 10.1017/S0022112010003368. 89

R. Rajaram and T. Lieuwen. Acoustic radiation from turbulent premixed flames. *Journal of Fluid Mechanics*, 637:357–385, 2009. ISSN 0022-1120. 8

L. Rayleigh. The explanation of certain acoustic phenomena. *Nature*, July 18:319–321, 1878. 17

H. S. Ribner. Convection of a pattern of vorticity through a shock wave. *NACA TN*, 2864, 1953. 20

H. S. Ribner. Shock-turbulence interaction and the generation of noise. *NACA TN*, 3255, 1954. 20

H. S. Ribner. Spectra of noise and amplified turbulence emanating from shock turbulence interaction. *AIAA Journal*, 25(3):436–442, 1987. 20

J. Sakurai and S. F. Tuan. *Modern quantum mechanics*, volume 1. Addison-Wesley California, 1985. 42

T. Schønfeld and M. Rudgyard. Steady and unsteady flows simulations using the hybrid flow solver avbp. *AIAA Journal*, 37(11):1378–1385, 1999. 109, 110, 147

L. Selle, F. Nicoud, and T. Poinsot. The actual impedance of non-reflecting boundary conditions: implications for the computation of resonators. *AIAA Journal*, 42(5):958–964, 2004. 115

C. Silva. *Numerical study of combustion noise in gas turbines*. PhD thesis, 2010. 61

C. Silva, I. Duran, S. Moreau, and F. Nicoud. Boundary conditions for low mach number acoustic codes. *AIAA Journal*, submitted, 2013. 187

Y. Sinai. The generation of combustion noise by chemical inhomogeneities in steady, low-Mach-number duct flows. *Journal of Fluid Mechanics*, 99, 1980. 7

W. A. Sirignano. *Fluid dynamics and transport of droplets and sprays*. Cambridge University Press, 1999. 149

J. Smagorinsky. General circulation experiments with the primitive equations: 1. the basic experiment. *Mon. Weather Rev.* , 91:99–164, 1963. 148

G. Staffelbach, L. Gicquel, G. Boudier, and T. Poinsot. Large eddy simulation of self-excited azimuthal modes in annular combustors. *Proc. Combust. Inst.* , 32:2909–2916, 2009. 160

S. Stow, A. Dowling, and T. Hynes. Reflection of circumferential modes in a choked nozzle. *Journal of Fluid Mechanics*, 467:215–239, 2002. ISSN 0022-1120. doi: 10.1017/S0022112002001428. vi, 18, 19, 28, 34, 35, 40, 41, 47, 48, 49, 50, 55, 63, 81

W. C. Strahle. On combustion generated noise. *J. Fluid Mech.* , 49:399–414, 1971. 8

W. C. Strahle. Some results in combustion generated noise. *J. Sound Vib.*, 23(1):113–125, 1972. 4, 8

N. Swaminathan, G. Xu, a. P. Dowling, and R. Balachandran. Heat release rate correlation and combustion noise in premixed flames. *Journal of Fluid Mechanics*, 681:80–115, 2011. ISSN 0022-1120. doi: 10.1017/jfm.2011.232. 8

M. Talei, M. J. Brear, and E. R. Hawkes. Sound generation by laminar premixed flame annihilation. *Journal of Fluid Mechanics*, 679:194–218, Apr. 2011. ISSN 0022-1120. doi: 10.1017/jfm.2011.131. 8

C. K. Tam, S. a. Parrish, J. Xu, and B. Schuster. Indirect combustion noise of auxiliary power units. *Journal of Sound and Vibration*, 332(17): 4004–4020, Aug. 2013. ISSN 0022460X. doi: 10.1016/j.jsv.2012.11.013. 7

C. K. W. Tam, S. A. Parrish, J. Xu, and B. Schuster. Indirect Combustion Noise of Auxiliary Power Units. In *AIAA Conference*, number June, Colorado Springs, 2012. 7

K. W. Thompson. Time dependent boundary conditions for hyperbolic systems. *J. Comput. Phys.* , 68:1–24, 1987. 26

H. S. Tsien. The transfer functions of rocket nozzles. *J. American Rocket Society* , 22(3):139–143, 1952. 5, 18

G. Wang, D. Papadogiannis, F. Duchaine, N. Gourdain, and L. Gicquel. Towards massively parallel large eddy simulations of turbine stages. San Antonio, USA, June 3-7 2013. Proceedings of the ASME TURBO EXPO 2013 Gas Turbine Technical Congress and Exposition. 113, 123

R. M. Wilcox. Exponential Operators and Parameter Differentiation in Quantum Physics. *Journal of Mathematical Physics*, 8(4):962, 1967. ISSN 00222488. doi: 10.1063/1.1705306. 42

F. A. Williams. *Combustion Theory*. Benjamin Cummings, Menlo Park, CA, 1985. 18

J. E. F. Williams and M. Howe. The generation of sound by density inhomogeneities in low Mach number nozzle flows. *Journal of Fluid Mechanics*, 70(3):605–622, 1975. 7

P. Wolf, G. Staffelbach, A. Roux, L. Gicquel, T. Poinsot, and V. Moureau. Massively parallel LES of azimuthal thermo-acoustic instabilities in annular gas turbines. *C. R. Acad. Sci. Mécanique*, 337(6-7):385–394, 2009. 160

C. Yoo, Y. Wang, A. Trouvé, and H. Im. Characteristic boundary conditions for direct simulations of turbulent counterflow flames. *Combust. Theory and Modelling* , 9:617–646, 2005. 115

D. Zhang and A. Prosperetti. Ensemble phase-averaged equations for bubbly flows. *Phys. Fluids* , 6(9):2956–2970, 1994a. 149

D. Z. Zhang and A. Prosperetti. Averaged equations for inviscid disperse two-phase flow. *J. Fluid Mech.* , 267(1-4):185–219, 1994b. 149

L. Zhao, W. Qiao, and L. Ji. Computational fluid dynamics simulation of sound propagation through a blade row. *The Journal of the Acoustical Society of America*, 132(4):2210–7, Oct. 2012. ISSN 1520-8524. doi: 10.1121/1.4740499. 109

B. T. Zinn, W. A. Bell, B. R. Daniel, and A. J. Smith. Experimental Determination of Three-Dimensional Liquid Rocket Nozzle Admittances. *AIAA Journal*, 11(3):267–272, 1973. 69

Articles

Journals

- I. Duran and S. Moreau. Solution of the quasi one-dimensional linearized Euler equations using flow invariants and the Magnus expansion. *Journal of Fluid Mechanics*, 723:190–231, May 2013b.
- I. Duran, S. Moreau, and T. Poinsot. Analytical and numerical study of combustion noise through a subsonic nozzle. *AIAA Journal*, 51(1): 42–52, 2013c.
- I. Duran, M. Leyko, S. Moreau, F. Nicoud, and T. Poinsot. Computing combustion noise by combining Large Eddy Simulations with analytical models for the propagation of waves through turbine blades. *Comptes Rendus de l'Académie des Sciences - Mécanique*, 341(1-2): 131–140, January 2013a.
- I. Duran, S. Moreau, F. Nicoud, T. Livebardon, E. Bouty, and T. Poinsot. Combustion noise in modern aero-engines. *AerospaceLab*, submitted, 2013b.
- M. Leyko, I. Duran, S. Moreau, F. Nicoud, and T. Poinsot. Simulation and modelling of the waves transmission and generation in a stator blade row in a combustion-noise framework. *JSV*, submitted, 2013.
- C. Silva, I. Duran, S. Moreau, and F. Nicoud. Boundary conditions for low mach number acoustic codes. *AIAA Journal*, submitted, 2013.

Conferences

- I. Duran and S. Moreau. Analytical and numerical study of the entropy wave generator experiment on indirect combustion noise. In *17th AIAA/CEAS Aeroacoustics Conference - AIAA-2011-2829*, Portland, Oregon, 2011.

- I. Duran, M. Leyko, S. Moreau, F. Nicoud, and T. Poinsot. Computing combustion noise by combining Large Eddy Simulations with analytical models for the propagation of waves through turbine blades. In *3rd Colloquium INCA*, Toulouse (France), November 17-18 2011.

- I. Duran and S. Moreau. Study of the attenuation of waves propagating through fixed and rotating turbine blades. In *18th AIAA/CEAS Aeroacoustics Conference (33rd AIAA Aeroacoustics Conference)*, number AIAA2012-2133 paper, Colorado Springs, USA, June 4-6 2012.

- I. Duran and S. Moreau. Numerical simulation of acoustic and entropy waves propagating through turbine blades. In *19th AIAA/CEAS Aeroacoustics Conference (34th AIAA Aeroacoustics Conference)*, number AIAA2013-2102 paper, Berlin, Germany, May 27-29 2013a.

- I. Duran, S. Moreau, and T. Poinsot. A new analytical method to compute nozzle impedances at all frequencies. In *EUROMECH Colloquium 546 – Combustion Dynamics and Combustion Noise*, Villa Vigoni, Menaggio, Italy, May 13-16 2013d.